3-11-2011

Time Resolved Filtered Rayleigh Scattering Measurement of a Centrifugally Loaded Buoyant Jet

Firas Benhassen

TIME RESOLVED FILTERED RAYLEIGH SCATTERING MEASUREMENT OF A CENTRIFUGALLY LOADED BUOYANT JET

THESIS

Firas Benhassen, 1st Lt, TUNAF

AFIT/GAE/ENY/11-M01

DEPARTMENT OF THE AIR FORCE
AIR UNIVERSITY

AIR FORCE INSTITUTE OF TECHNOLOGY

Wright-Patterson Air Force Base, Ohio

AFIT/GAE/ENY/11-M01

TIME RESOLVED FILTERED RAYLEIGH SCATTERING MEASUREMENT OF A CENTRIFUGALLY LOADED BUOYANT JET

THESIS

Presented to the Faculty

Department of Aeronautics and Astronautics

Graduate School of Engineering and Management

Air Force Institute of Technology

Air University

Air Education and Training Command

In Partial Fulfillment of the Requirements for the

Degree of Master of Science in Aeronautical Engineering

Firas Benhassen, BS

1st Lt, TUNAF

March 2011

AFIT/GAE/ENY/11-M01

TIME RESOLVED FILTERED RAYLEIGH SCATTERING MEASUREMENT OF A CENTRIFUGALLY LOADED BUOYANT JET

Firas Benhassen, BS

1st Lt, TUNAF

Approved:

Dr. Marc D. Polanka (Chairman)	16 Mar 11 Date
Dr. Mark F. Reeder (Member)	16 Mar 11 Date
Lt Col. Carl R. Hartsfield (Member)	16 Mar 11 Date

Abstract

The combustion process within the Ultra-Compact Combustor (UCC) occurs in the circumferential direction. The presence of variable flow density within the circumferential cavity introduces significant buoyancy issues. On the other hand, G-loading caused by the presence of centrifugal forces, ensures the circulation of the flow in the circumferential cavity and enhances the completion of the combustion process before allowing the exit of the hot gases to the main flow. The coupling between buoyancy and high G-loading is what predominately influences the behavior of the flow within the UCC. In order to better understand the combustion process within the UCC, three different experiments were run. The overall objective of these experiments is to investigate the effects of both buoyancy and G-loading on the trajectory and the mixing of a jet in a co-flow. The first experiment involved setting up the Filtered Rayleigh scattering (FRS) technique to be used in this research. Then, using horizontal and curved sections, two types of experiments were run to characterize and measure both G-loading and buoyancy effects on the overall behavior of a jet in a co-flow of air. Measurements were made using a FRS set up which involved a continuous wave laser and a high speed camera showing adequate signal to noise ratio at 400 Hz. Collected time resolved images allowed for the investigation of the effects of G-loading and buoyancy on the mixing properties and trajectory of the jet.

To my mother and my father

Acknowledgments

I would like to express my gratitude and appreciation to the following individuals without whom this work would not have been made possible. First of all, special thanks go to my thesis advisor Dr. Marc Polanka for his support and patience throughout this entire program. I would also like to thank Dr. Mark Reeder for his insight and specific guidance. My sincere thanks as well, go to Captain Kenneth LeBay for his patience and willingness to give up countless hours of his research time to help me with my experiments in the COAL lab. I would also like to thank Mr. Jay Anderson and the technicians John Hixenbaugh, Chris Zickerfoose, and Brian Crabtree for their technical support. I would also take this opportunity to thank Mr. Jacob Wilson and Mr. Samuel Raudabaugh for helping me with SolidWorks. And last, but not least, I would like to the Mrs. Annette Robb, the director of the International Military Student Office (IMSO) and her technician Mr. Rorey Kanemoto for their time, efforts, and continuous support in all matters.

Firas Benhassen

1st Lt, Tunisian Air Force

Table of Contents

Page

List of Figures

Page

List of Tables

Page

TIME RESOLVED FILTERED RAYLEIGH SCATTERING MEASUREMENT OF A CENTRIFUGALLY LOADED BUOYANT JET

I. Introduction

I.1. Background

The human life on earth is affected in many aspects by fluids. It is, in fact, impossible to imagine life without air, water or blood which fuel most of the living organisms. The oil and all its derivatives are the driving motors of technology and many industrial activities that sustain our economy and daily lives. For hundreds of years, fluids have been the subject of continuous interest for physicians, biologists, environmentalists, physicists, chemists, and engineers. The ultimate objective of investigating the characteristics of a fluid flow (whether at gaseous or liquid state) is to predict and possibly control its behavior. When performing these investigations, scientists and engineers are interested in the mechanisms that trigger or prevent the occurrence of specific patterns or changes within the flow. In fluid dynamics, the behavior of the fluid is studied in relation with inertial, viscous, thermal, and buoyancy effects. This research will focus closely on the dynamics associated with buoyant effects and characterize their contribution in shaping the behavior of the fluid flow.

A jet is considered buoyant when it is discharged into a medium where a large density gradient is present. The jet effective density depends on whether it is hotter or cooler than its surrounding fluid. The density gradient can also be due simply to the presence of different species in the medium [1]. Examples of situations or problems involving buoyant jets include but are not limited to: the emission of pollutant into the atmosphere or oceanic waters, safety and fire hazards associated with leakage of gases such as hydrogen into air [2], and heating issues

associated with an uneven temperature distribution within combustion systems. Therefore, studying buoyancy effects proves to be of great importance when it comes to preventing environmental hazards, tracking pollutant plumes, or improving combustion efficiency.

However, acquiring accurate analysis from these investigations is often a challenging task due to the sensitivity of the flow properties (velocity, pressure, temperature, etc) to the introduction of any intrusive probing device within the medium in question. Examples of intrusive measuring devices include hot-wires, thermocouples, and pitot tubes. In addition to their body influence on the flow, these devices cannot operate properly in harsh media of high temperature and pressure such as within a combustion environment [3]. Laser techniques however, are non-intrusive and prove to be capable of both high temporal and spatial resolution [4]. The non-intrusive aspect of these diagnostic techniques allows for the investigation of the flow properties within boundary layers or combustion zones [4]. Particle Image Velocimetry (PIV) and Filtered Rayleigh Scattering (FRS) are two of the most important laser techniques considered by the researches when studying flow properties. PIV involves shining a laser sheet into a pre-seeded flow and taking a series of images using a camera at a known frame rate. 2D velocity is then calculated by comparing consecutive frames and dividing the traveled distance by the time difference between the frames [5]. On the other hand, FRS techniques do not require the presence of seeds within the flow. This technique involves the use of a narrow-line bandwidth laser along with a camera and a molecular filter used to block unwanted background or dust particles interference.

More specifically, for FRS when a flow is illuminated with a laser beam (or sheet), light is scattered due to the presence of particles within the flow. The intensity of the scattered light is proportional to the cross section of the scattering particle or molecule and thus to the density of

the species [6]. Using a high speed camera, time resolved information can be obtained by capturing scattered light images and constructing density fields [7]. The molecular filter is used to absorb the scattered light resulting from the stationary particles and background noise while allowing the scattered signal shifted and broadened by thermal and Doppler effects to be transmitted [8]. In addition to density profiles, more flow properties can be obtained by relating the frequency shift and the broadening of the signal to respectively the velocity and the temperature of the scattering species [7] as it will be discussed in the literature review section. The FRS technique along with the use of a high speed camera constitutes the basis of this research and will be thoroughly described in the second chapter as part of the literature review. Now that the overall background of the research is laid out, let us delve into the essence of this study and start with its relevance from an aerospace engineering stand point.

I.2. Problem Statement

This research is initiated and sponsored by the Propulsion Directorate of the Air Force Institute of Technology (AFRL) located at Wright Patterson Air Force Base. The global scope within which falls this study is ultimately integrating the Ultra Compact Combustor (UCC) concept with a Highly Efficient Embedded Turbine Engine (HEETE) program [9].

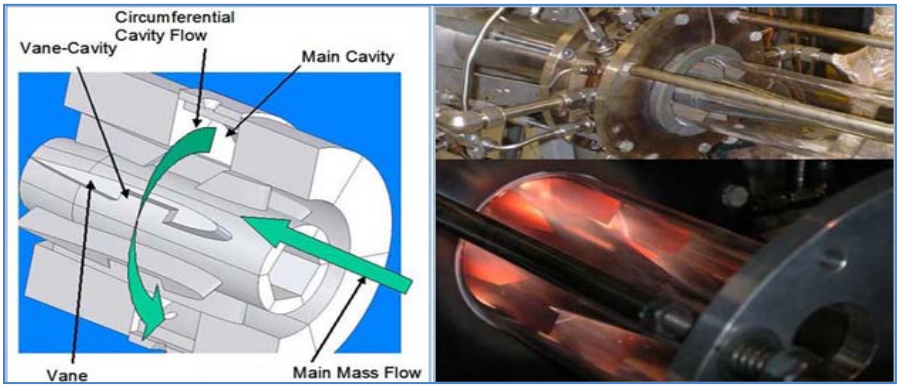

Figure 1. Conceptual (Left) and Actual AFRL UCC Model (Right)

The concept of the UCC (shown in Figure 1) stems from the need to develop a more compact combustion unit that increases the engine's thrust to weight ratio while maintaining a comparable fuel efficiency and structural robustness. The thrust to weight ratio is increased by the reduction of the overall weight of the engine as a direct result of the more compact design. The basic idea is to inject fuel and air into a circumferential cavity where combustion occurs in the presence of high G-loading caused by the spinning of the unit. The centrifugal effect forces the unburned (cold/heavy) mixture to remain circulating within the cavity until combustion is completed. The hot (light) combustion products are then driven by buoyancy effects out of the circumferential cavity, through the radial vane cavity (RVC), and back to the main flow [10]. Combustion occurs within the circumferential cavity which creates a large density gradient due to the presence of lighter than air hot products and heavier than air unburned reactants. This density difference brings up buoyancy effects which are the driving forces of pushing the hot gas out of the circumferential cavity. Buoyancy and G-loading effects are both important in the combustion process. Hence, their unique interaction needs to be characterized as they both influence the direction of the flow within the circumferential cavity. As it exits the circumferential cavity, the hot gas encounters the main flow. Initially, this creates a jet in cross flow situation that quickly transforms to a hot jet in a relatively cold co-flow as the mixture is carried downstream by the main flow. In order to create an even temperature profile across the turbine vanes and hence avoid burning the turbine blades, we need to understand the mechanism that ensures the migration of the hot gas from the exit of the circumferential cavity and radically down the turbine airfoils. This migration ensures the mixture of the hot gas with the colder main flow and allows for cooling to occur [9]. As a result, it is apparent that buoyancy affects the flow direction, mixture, and cooling process within the UCC.

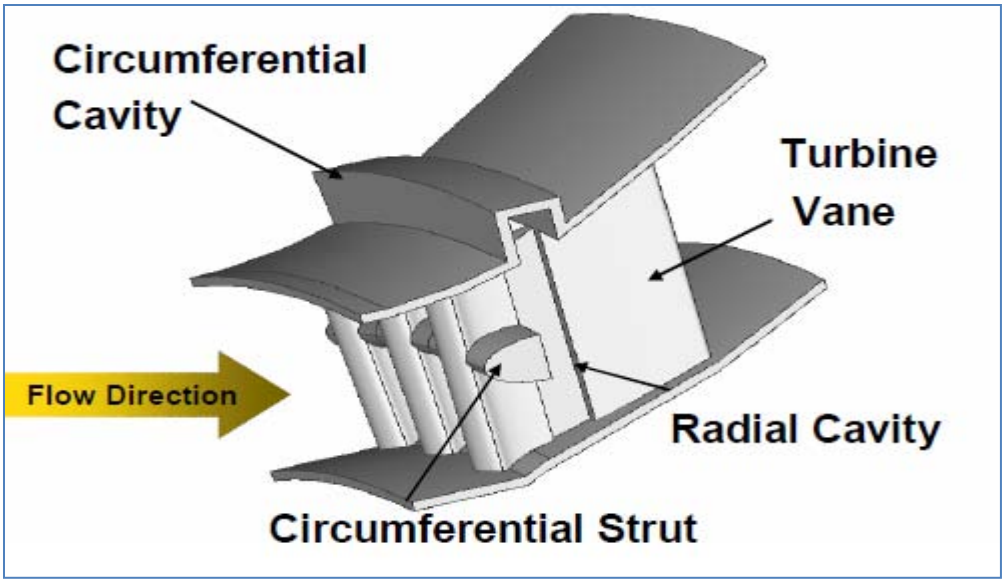

Figure 2. UCC Integration with Turbine Vanes (modified)

Figure 2 shows a schematic of the UCC integration with turbine vanes. Whether the UCC concept is integrated with a missile size engine, a fighter size engine, as an inter-stage turbine burner (ITB), or as a main combustion unit between the compressor and turbine, there are fundamental questions to be answered to ensure a successful integration [9]. These questions underline the objectives of this research.

I.3. Objectives

The objectives of this study can best be described by finding the answer to the following questions:

1. How does buoyancy affect the direction of the flow within the circumferential cavity?
2. Does G-loading work against or with buoyancy with respect to the mixing of the hot and cold flow in the main cavity?
3. What is the trajectory of the exiting hot gas once it is co-flowing with the relatively colder main flow?

The answers to these questions will be sought simultaneously from two collaborating perspectives. The first one, ties the relevance of these objectives to the UCC integration and the engineering aspect of the posed problems. The second set of objectives works towards strengthening of fundamental concepts involving buoyant jets and highlights the academic values of the investigation along with the use of time resolved FRS technique.

I.4. Implications

Knowing the direction of the flow at any sub-stage of the combustion will help optimize the integration of the UCC with a fighter size turbo jet engine while ensuring structural robustness of the turbine blades. The study of centrifugally loaded buoyant jet in the presence of a co-flowing gas has not been thoroughly investigated by previous researchers which makes this work original. The findings of this research will ensure a better understanding of the dynamics governing a buoyant jet's behavior. In addition, the use of the FRS techniques in conjunction with a high speed camera will allow for the acquisition of time resolved concentration profiles. In this manner, intermediate fluctuations and turbulence effects can be recorded, captured, and analyzed. The contribution added by the time resolved aspect of the data acquisition in this research will help understand the interaction between the jet and the co-flow. The time resolution difference in data acquisition has drastic implications in the way we interpret physical phenomena associated with the centrifugally loaded buoyant jet.

II. Literature Review

The relevance of any research stems from the understanding of the problem in hands and the reported efforts put in to solve it. It is therefore critical to present selected previous studies that put this work into context and strengthen its relevance. Specifically, this literature review will be divided into three major parts. First, a theoretical background of the Rayleigh scattering phenomenon and the Filtered Rayleigh scattering technique employed in this study is described. Second, results from major studies characterizing the behavior of buoyant jets are briefly presented. Lastly, the relevance of this work to the UCC and the effects of G-loading on the buoyant jet behavior are introduced while referencing previous investigations.

II.1. Rayleigh-Scattering

The Rayleigh scattering phenomenon was first documented by the English physicist Lord Rayleigh in the 19th century. His studies aimed to understand the origin of the intensity and color of the atmosphere [6]. Rayleigh scattering pertains to the elastic scattering from molecules as opposed to Mie scattering which is attributed to the scattering from particles [11]. The analytical theory and model for Mie scattering was developed by Gustav Mie who distinguished between the scattering of light by small particles (with diameters less than the wavelength of light) and bigger particles and molecules [3]. Mie's mathematical model indicated that the intensity of the scattered light (I) caused by a single particle is proportional to the particle's diameter (d) and the inverse of the wavelength raised to the fourth as shown in Equation (1) [3]. Equation (1) offers an explanation to the origin of the blue color of the sky. Blue light has the shortest wavelength of all the visible light wavelengths and hence scatters more than the other lights such as red, green or yellow.

$$I \propto d.\lambda^{-4} \quad (1)$$

Rayleigh scattering builds on these principles by realizing that when light goes through a gas, it is scattered by the molecules and particles present in the gas [11]. In order to formulate a full developed theory that includes scattering from molecules, the diameter (d) is replaced by a parameter called the total cross section and given the Greek symbol σ_{ss}. Equation (1) is then modified resulting in Equation (2) which relates the power of scattered (P_s) light to the incident light intensity (I_o) [6]:

$$P_s = \sigma_{ss} I_o \tag{2}$$

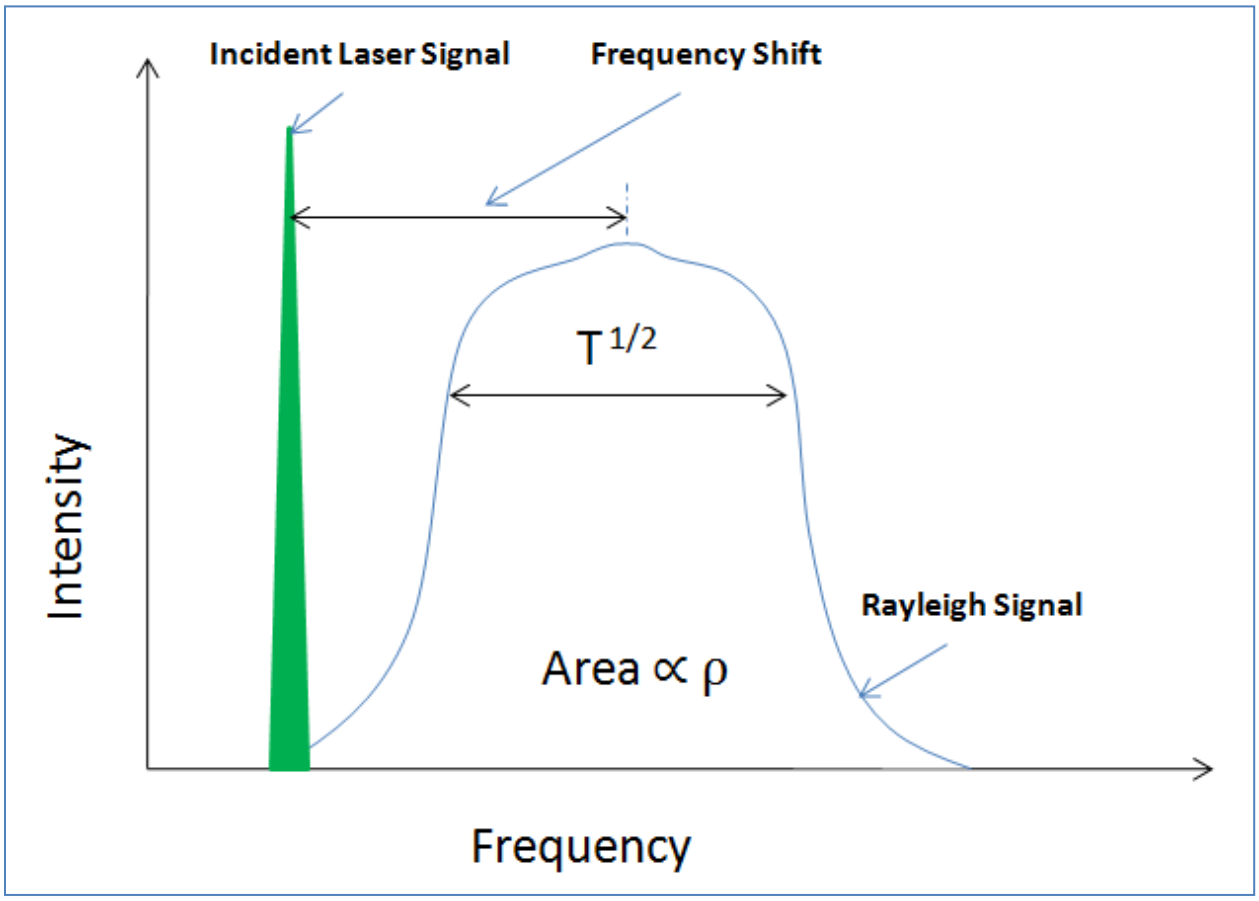

Figure 3. Rayleigh Scattering Spectrum (as inspired by Mielke *et al.*'s figure)

The amount of scattered signal (area under the curve in Figure 3), is proportional to the cross section and hence to the density of the molecules. Furthermore, when light is scattered,

two things occur. First, the scattered light is shifted in frequency due to Doppler Effect. Second, the scattered light line-width is broadened as shown in Figure 3 due to the increase of the kinetic energy driven by the particles' motion. Since the frequency shift is mainly due to the translational motion of the molecules [11], the flow velocity can be measured by processing the scattered light images at different locations. Velocity can be calculated using the Yeh and Cummins equation (given by Equation (3)) which relates the velocity V, the scattering angle θ, the frequency shift $\nu_{D,}$ and the incident light wavelength λ [7].

$$\nu_D = \frac{2V\sin(\theta/2)}{\lambda} \tag{3}$$

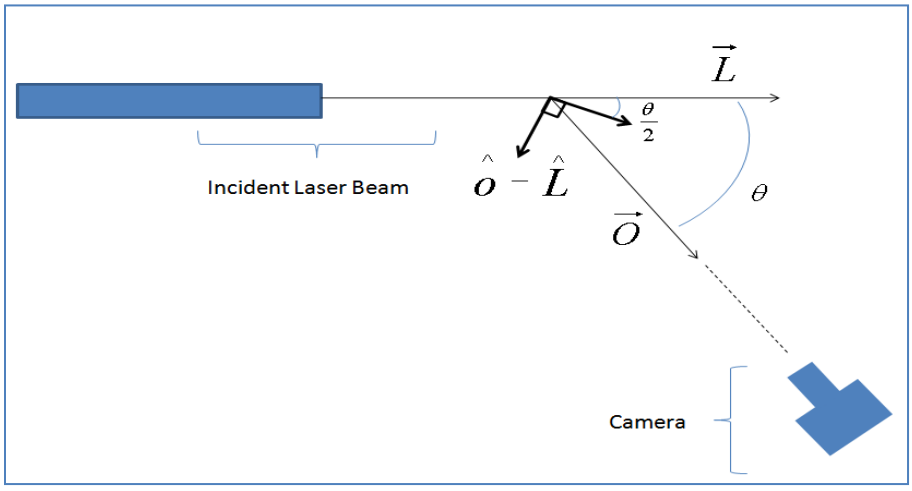

Figure 4. Diagram of a Typical Filtered Rayleigh Scattering Set Up (as inspired by Miles *et al.*'s figure)

The velocity V is the scalar component of the vector velocity in the direction to which the FRS is sensitive as shown in Figure 4 [7]. Further discussion of the frequency shift and the Doppler Effect will be presented in fourth chapter of this report.

In addition, the line width of the scattered signal turns out to be proportional to the flow temperature (as shown in Figure 3). Quantitative values of temperature can be determined using Equation (4) below [12]:

$$\Delta f = \frac{2\sin(\theta/2)}{\lambda}\left[\frac{8kT\ln 2}{m}\right]^{0.5} \quad (4)$$

Equation (4) allows for the calculation of the temperature T, given the angle between the illumination and detection (θ), the incident light wavelength (λ), the mass of the gas molecule (m), the linewidth (Δf), and the Boltzman constant (k).

Different species have different molecular cross sections and hence different Rayleigh scattering spectra. This outlines the utility of this concept as it allows for possible observation of the individual behavior of the species within the flow. In fact, even the reverse task proves to be feasible. In 2004, Sneep and Ubachs were able to back out the Rayleigh scattering cross sections of several species such as CO_2, CO, CH_4, and others by measuring the loss rate of the scattered light. As shown in Table 1, the measured values were within 15% difference of the theoretical values. The theoretical values were calculated using curve fit approximation and medium refractive index correction equations [13].

Table 1. Measured vs Tabulated Cross Section Values (as given by Sneep *et al*.)

Gas	Measured σ ($10^{-27}cm^2$)	Tabulated σ ($10^{-27}cm^2$)	Error (%)
Ar	4.45	4.56	0.11
N2	5.10	5.30	3.8%
CO	6.19	6.82	9.2
CO_2	12.4	13.39	7.5
CH_4	12.47	14.69	15
N_2O	15.9	18.19	12.6
SF_6	32.3	34.1	5.2

However, the presence of dust particles or any background noise in the medium in question distorts the scattered signal and gives false readings and analysis regarding the properties of the flow. This drawback of the Rayleigh scattering application inspired the development of more robust techniques such as the Filtered Rayleigh Scattering (FRS).

In the FRS technique, a molecular filter is used to block scattered signal from walls, windows, and particles and transmit only scattered light from molecules of interest as shown in Figure 5 below. A filter should have steep cut off edges and allow for an overlap of frequencies with the tunable laser in use [8].

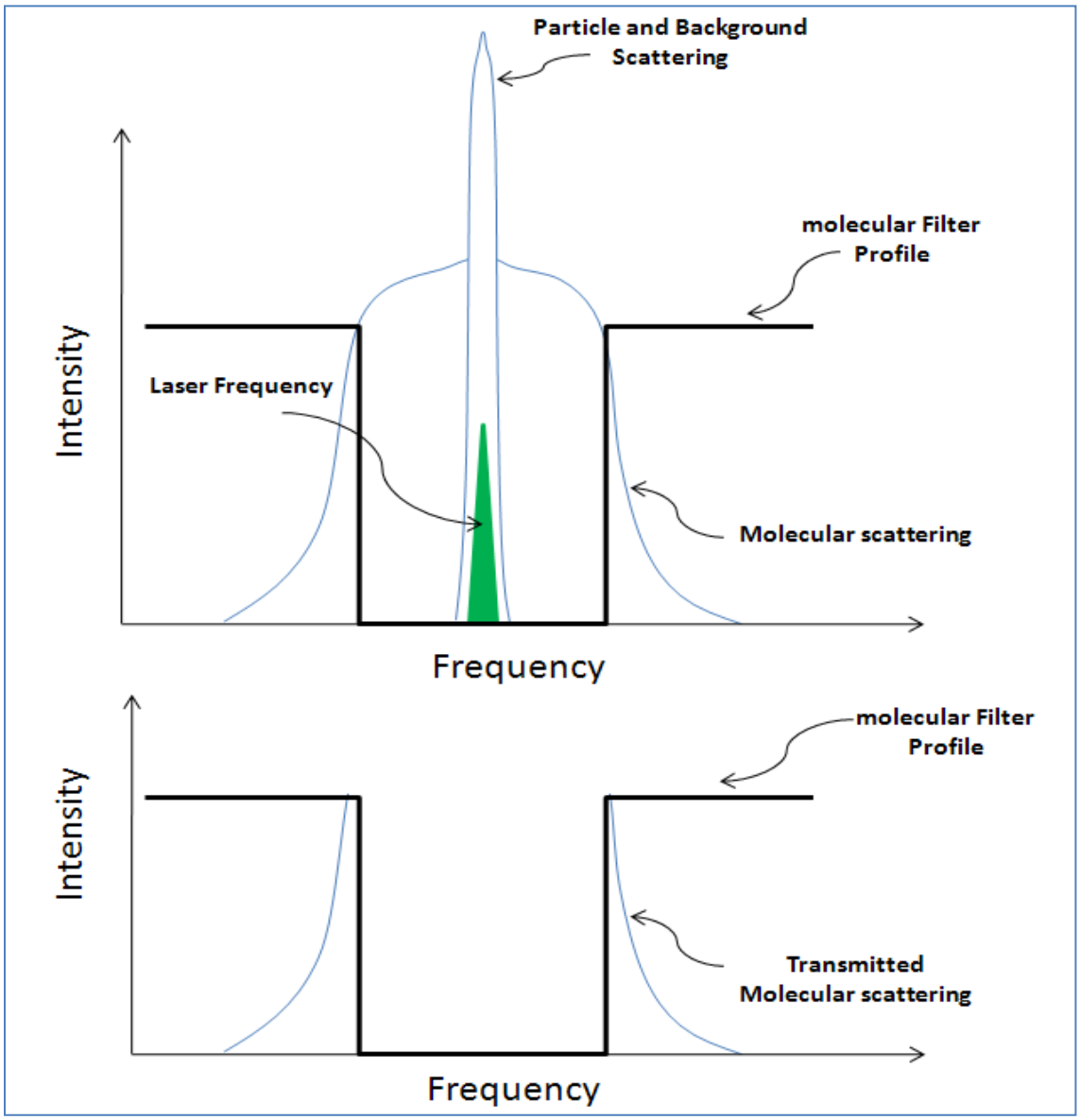

Figure 5. Illustration of the FRS Concept (as inspired by Miles *et al.*'s figure)

The top graph of Figure 5 shows the background/particle scattering signal and the molecular Rayleigh scattering signal. The bottom graph shows the absorption spectrum of the molecular filter along with the transmitted Rayleigh scattering signal [8].

In their study on atomic and molecular notch filters, Miles *et al.* present three main criteria for the selection of the filter [8].

a. Sharp cut off edges for high spectral resolution.
b. Deep absorption well that translates into almost 0% transmittance in the blocking region and transmission close to 100% outside the absorption walls.
c. Overlap with tunable laser in use.

The molecular filter profile should be determined to optimize the collection of the scattered light by tuning the laser to an adequate frequency. The goal is to make sure that most of the scattered light (broadened and shifted) fall outside the absorption well of the filter while ensuring near total absorbance of the incident signal itself, the background noise, and Mie scattering (scattering due to particles). An iodine filter will be used for this research along with the Coherent Verdi V12 continuous wave (CW) laser at 532 nm. The iodine filter is recognized for having many transitions throughout the visible portion of the frequency spectrum. Figure 6 below illustrates the transmission curve of an iodine filter using a 7W continuous wave Coherent Innova Sabre R Argon ion laser at 514 nm [14]. It is important to note that the higher the temperature of the cell, the deeper the absorption well gets. In fact at 90^{o} there is approximately 100% blocking (0% transmission) for a small range of wavenumber.

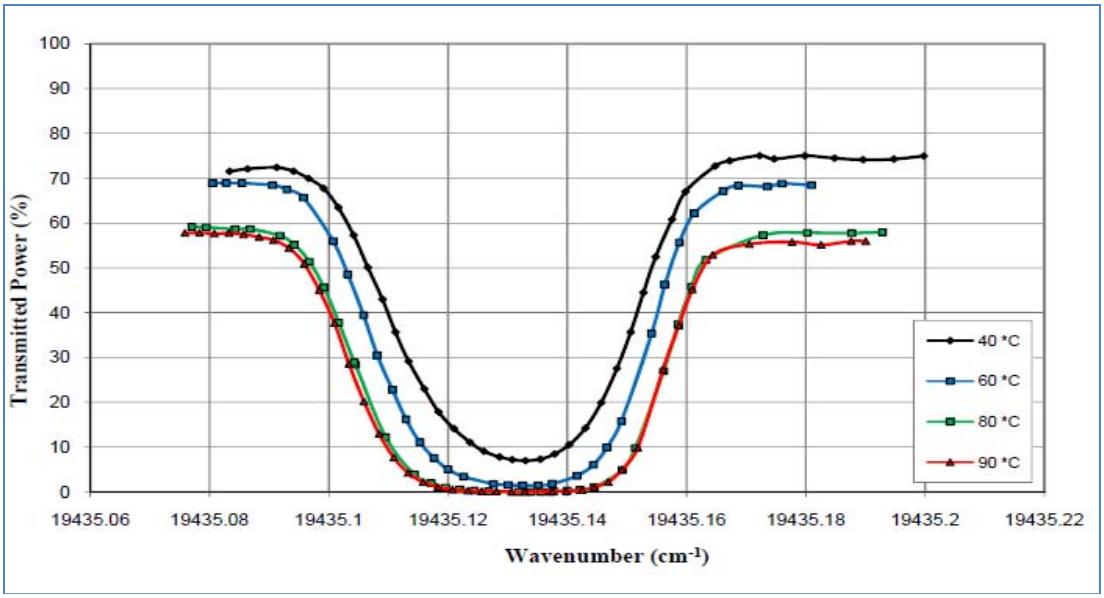

Figure 6. Iodine Filter Absorption Well Characterization

The equation for the intensity of light transmitted through a filter is given by Equation (5) :

$$I = I_o e^{-\alpha l V(w)} \tag{5}$$

Where I is the transmitted intensity, I_o the incident intensity, α is an absorption constant, l the length of the filter, and V(*w*) a line width function that depends on the incident wavelength and molecular collisions (i.e the temperature of the cell) [8]. The take away of this equation is that the filter's absorption well depends on the temperature of the filter and the wavelength of the incident light. It is necessary therefore to characterize the filter's absorption well at 532 nm before using it to ensure optimal Rayleigh scattering signal collection. The goal is to determine the center line frequency of the absorption well as well as its width. As mentioned in the methodology section of the first chapter, the characterization of the iodine filter at 532 nm is the heart of the first experiment which will be fully discussed in Chapter Three of this report.

The relevance of the present work stems from the need to characterize the effects of buoyancy and its governing parameters on the trajectory of a jet in a co-flow and its mixing

properties. The present work is based on a Filtered Rayleigh scattering (FRS) set up that allows the capture of the intensity of the scattered light off of the molecules present in the testing area. The fundamentals of the FRS are discussed throughout this work. This non intrusive technique involves the use of a laser source, an iodine filter to block unwanted signal, and a camera to capture the scattered light signal. In previous work, the use of a laser light along with a molecular filter proved to be convenient when seeking either quantitative or qualitative mixing measurements of gaseous flows. Jenkins and Desabrais used Planar Doppler Velocimetry (PDV) to resolve velocity measurements within a low speed flow field [15]. The set up involved the use of a tunable laser (Coherent Verdi V-18) in conjunction with three camera/iodine filter systems. The iodine filters were used to discriminate the Doppler shifted scattered light (due to the motion of the particles) from the un-shifted one. PDV is similar to FRS in the way that data is extracted out of filtered scattered light using molecular cells such as the iodine cell used in this study.

In addition, one of the most recent studies in the literature pertaining to the acquisition of time resolved concentration measurements in a gaseous flow is the work of Cheung and Hanson in 2009. Using a tracer-based laser-induced fluorescence (LIF) diagnostic applied on a N2 jet with 4% toluene (by mole fraction) issuing into air, the authors were successfully able to obtain fluorescence signal time histories at a frame rate of 18.5 kHz using a continuous wave laser [16].

II.2. Effects of Buoyancy and G-loading on a Jet's Behavior

This section will highlight the dynamics and mechanisms associated with a centrifugally loaded buoyant jet as described in a collection of the most relevant reported efforts in this area.

II.2.1. Buoyant Jets

As mentioned in the introduction, the leading motive behind this research is to understand the dynamics of a buoyant jet subjected to a G-loading in a combustion environment such as in

the case of the UCC. An important step toward understanding these dynamics deals with the study of the fundamental concept of buoyancy and the researches associated with the behavior of buoyant jets in different configurations (horizontal, vertical, G-loaded, etc) and various environments such as combustive or cold medium.

In fluid dynamics, buoyancy is considered when a fluid with an initial momentum is discharged into a medium where a density gradient is present. This gradient can be due to the presence of various species or a difference in the temperature of the present entities (thermal gradient) which alters their effective densities [17]. If we simply consider the behavior of an impinging horizontal low density jet into a higher density medium, we anticipate the trajectory of the jet to be influenced at least by inertial forces, body forces, density gradient, thermal gradient, molecular diffusion, viscosity, and turbulence. Due to the coupling between all these physics, buoyancy is usually described in the literature in terms of different parameters such as Reynolds number, Froude number, Grashof number, and Richardson number. These parameters are defined respectively as follows:

$$Reynolds\ Number\ \ (Re) = \frac{Inertial\ \text{Forces}}{Viscous\ Forces}$$

$$Re = \frac{4\rho Q}{\pi D \nu} \tag{6}$$

$$Q = VD \tag{7}$$

$$Froude\ Number\ (Fr) = \frac{\text{Inertial Forces}}{Gravitational\ Forces (Buoyancy)}$$

$$Fr = \frac{4Q}{\pi D^2 [gD\left|\frac{\rho_a - \rho}{\rho}\right|]^{0.5}} \tag{8}$$

$$Grashof\ Number\ \ (Gr) = \frac{Gravitational\ \text{Forces(Buoyancy)}}{Viscous\ Forces}$$

$$Gr = \frac{g\beta D^3\ (T - T_a)}{\nu^2} \tag{9}$$

$$Richardson\ Number\ \ (Ri) = \frac{Buoyancy\ Forces\ (Natural\ Convection)}{Inertial\ Forces\ (Forced\ Convection\ )}$$

$$Ri = \frac{\text{Gr}}{Re^2} \tag{10}$$

Where ρ is the jet density, D is the jet diameter, ν is the jet kinematic viscosity, V is the velocity of the jet, Q is the volumetric flow rate, g is the gravitational acceleration, T is the jet's temperature, T_a is the ambient temperature, and β is the coefficient of thermal expansion of the jet.

One effort in the literature that was fundamental to this research was the study performed by Reeder *et al.* at AFIT in 2008 [18]. Its relevance stems from the use of FRS to collect concentration measurements that allowed the investigation of the trajectory and the cross sectional shape of a buoyant jet in ambient air. Both positive and negative buoyancy were investigated using respectively horizontal jets of helium and carbon dioxide. In order to capture images of the jet's cross section, the authors used a continuous wave laser operating at a nominal frequency of 514.5 nm wavelength, an iodine filter, and a PCO.4000 camera. The Froude number was varied between 0.71 and 46 while the Reynolds number ranged from 50 to 1200. The study acquired data at five different stream-wise locations to track the trajectory of the jet. Figure 7 illustrates a sample raw picture of the helium jet cross section captured at x/D = 1.5 location. The helium jet is darker than the surrounding air spectrum since helium has a much

smaller cross section (only 1.4 % of that of air) than air [18] and hence scatters much less laser light. Figure 8 and Figure 9, however, depict samples of the processed FRS images for both the helium and CO_2 jets.

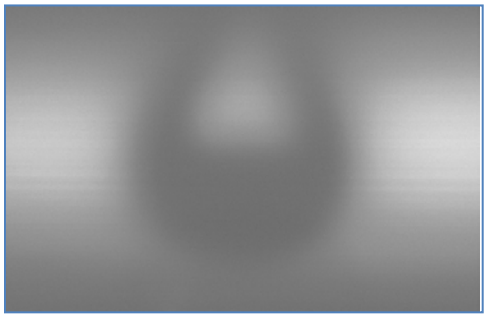

Figure 7. Helium Jet Cross Section for Fr = 0.71 and Re = 100

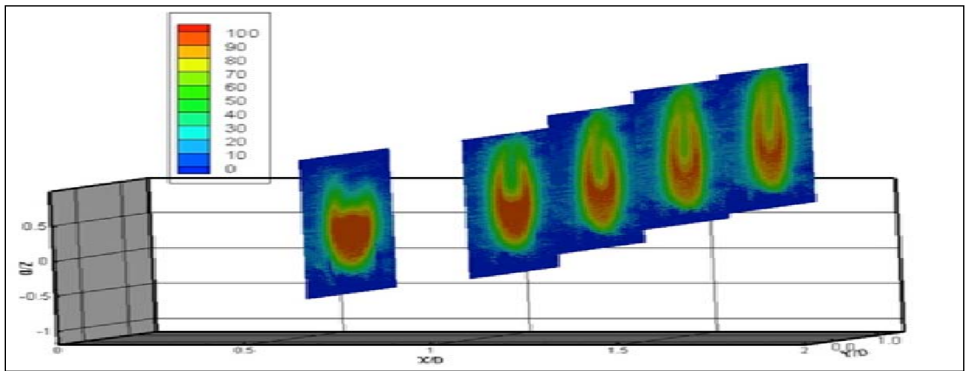

Figure 8. Filtered Rayleigh Scattering Data of a Buoyant Jet Flowing at 7.5 SLPM of He

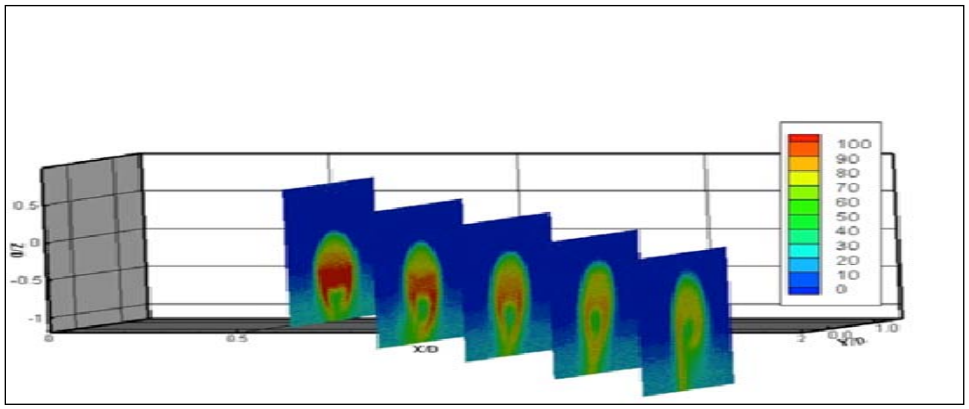

Figure 9. Filtered Rayleigh Scattering data of a Buoyant Jet Flowing at 1 SLPM of CO_2

As expected, the lighter than air jet (helium) exhibited positive buoyancy while the heavier than air jet (CO_2) had negative buoyancy. In addition, it was noted that for values of Froude number between 1.5 and 3 the jet's cross section exhibits the formation of a plume (a tear drop shape) ejecting from the core of the jet and directed upward for positive buoyancy (helium) and downward for negative buoyancy (CO_2). Raw images of these plumes are shown in Figure 7 and Figure 10 for respectively the helium and CO_2 jets.

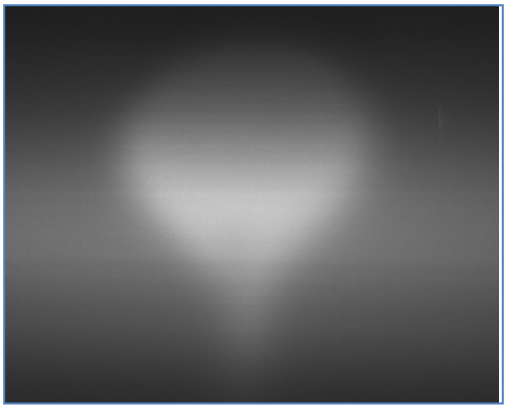

Figure 10. CO_2 Jet Cross Section for Fr = 0.71 and Re = 100

The formation of these plumes for specific ranges of Froude number was also documented by Arakeri *et al.* [19] in their study on buoyant horizontal laminar jet. Their set up was based on "the injection of pure water jet in a brine solution." The study showed that horizontal jets were subjected to a bifurcation (formation of plumes) at low Froude number conditions between values of 1 and 4.

In addition, it was noted that at sufficiently low Froude number (less than unity), the cross section of the jet exhibited the formation of side lobes. For Froude number values less than unity the tear drop shape was suppressed and two plumes (side lobes) emanated from the sides. This behavior, which could clearly be seen in Figure 8 and Figure 9 above, was noted for both positive and negative buoyancy. The formation of these lobes was more apparent at low values

of Froude number where buoyancy dominates inertia forces which underlines the effect buoyancy has in shaping the cross section of the jet. In Reeder *et al.*'s study, the effect of inertia on the shape of the jet's cross section was also investigated through the variation of Reynolds number. The study showed that the change in the shape of the plumes was minimal as Reynolds number was changed. This suggests that the shape of the jet's cross section is driven by buoyancy rather than inertia [18]. Therefore, turbulence was not accounted for during these tests. In fact, the sampling rate (1 Hz) was relatively low and would not have allowed for time resolved images where turbulent effects could be observed.

Turbulence, however, was investigated by Subbarao in 1989 when he studied the behavior of a buoyant jet as a function of Richardson and Reynolds numbers. The study involved taking Schlieren photographs of a vertical helium jet as it was injected in a co-flowing air stream [1]. Cone-like structures were repeatedly seen in the Schlieren photographs and were essentially vortex rings. These structures were the direct result of the interaction between buoyant forces and the jet's momentum. The vortex rings appeared to exhibit a constant periodicity for ranges of Richardson number values between 1 and 4 and Reynolds number values between 260 and 900. The vortex rings became aperiodic for values of Richardson number greater than 5. Furthermore, the study concluded that the higher the Richardson number (greater buoyancy), the more accelerated the core jet (the cap of the cone) got and hence the more stretched out the cells (cones) were. In addition, it was also noted that at higher Reynolds number the flow was more turbulent which was expected. However, the transition from laminar to turbulent flow occurred at a point closer to the jet exit as either Richardson number or Reynolds number increased which indicated that the transition point was not solely affected by the Reynolds number but also by buoyancy effects [1].

On a side note, it was noted that Subbarao used an absolute expression for the jet velocity in the calculation of Richardson and Reynolds numbers even in the presence of a co-flowing air. As it was mentioned earlier, this study will investigate the importance of the relative velocity of the jet with respect to the co-flow when calculating buoyancy parameters. This will attempt to understand how the Froude number should be defined in the presence of a co-flow since the traditional definition does not include any term associated with a co-flowing jet. Testing will compare the impact of changing both the absolute velocity range and the relative velocity difference between the jet and the co-flow to understand the ongoing physics.

As documented by the literature, numerical and experimental studies involving hot and cold impinging jets were carried out to characterize the effect of both aiding and opposing buoyancy on the flow behavior. One of these investigations was the numerical study performed by Kumar and Yuan in 1988 which involved simulating an impinging jet (both hot and cold) in a rectangular cavity with constant wall temperatures. The conclusion of this study is that an impinging cold jet encounters opposing buoyancy which prevents it from penetrating deeper down the cavity. On the other hand, a hot jet penetrates all the way to the bottom of the cavity due to the absence of opposing buoyancy (presence of aiding buoyancy). It was noted in this analysis that a vortex was created on the bottom left corner of the cavity due to the presence of two opposing flows (upward and downward) in the case of the cold jet while no vortex was observed in the case of the hot jet [20].

A similar investigation was performed by Sherif and Pletcher in 1988 on aqueous turbulent hot jet. The investigation confirmed the presence of a “kidney shaped” structure of the jet cross section. The behavior of the flow was analyzed using contours of mean and fluctuations of temperature across and along the jet. The contours were generated at velocity ratios of 1, 2, 4,

and 7. The authors discovered that the jet was more turbulent away from the centerline of the jet (where the jet lost some of its momentum). In addition, the increase in the velocity ratio resulted in a more pronounced and effective mixing of the jet and the streamline flow [21].

II.2.2. G-loaded jet

For the purpose of this research and its application on the UCC, the effect of G-loading on the jet's trajectory needs to be considered as well. In general, the G-load is given by Equation (11) which is a relationship between the mass flow rate, the radius of curvature (r), the jet's density (ρ_{jet}), and its cross sectional area (A). Within the UCC, the values of G-loading range between 500 and 2000. The G-loading is controlled by varying the velocity of the jet or essentially the mass flow rate. Equation (11) provides an expression for G-loading that will be used in this study.

$$G - load = \left(\frac{\dot{m}}{\rho_{jet} A}\right)^2 \left(\frac{1}{rg}\right) \tag{11}$$

The U.S. Air Force Research Laboratory (AFRL) has been, since 2001, the leading party in the conduction of studies and investigations geared toward gaining a better understanding of the combustion process within the UCC. In 2004, Armstrong used the concept of chemiluminescence to underline the effects of the centrifugal force on the combustion process using the UCC test rig located in the AFRL's Atmospheric Combustion Research Laboratory [22]. The study involved running the UCC using the JP8+100 fuel and measuring the intensity of light emitted by the three excited radicals C_2* (excited C_2), OH* (excited OH), and CH*(excited CH) at eight different port locations in the inner and outer radius of the circumferential cavity. The study showed that the intensities ratios CH*/OH* and C_2*/OH* were at their highest values at the ports in the outer radius of the circumferential cavity. This

indicated that the largest amount of fuel air mixture was reacting in the area of high G-loading (the outer radius). Furthermore, it was noted that the intensity of C_2* decreased as the G-loading increased (going from inner to outer radius of the cavity). This trend indicated that the "higher G-loadings reduced the residence time" which "could quench the C_2* production" [22].

In an additional effort to characterize the effects of G-loading on the combustion process, the Air Force Institute of Technology's Combustion Optimization and Analysis Laser (COAL) Laboratory conducted a series of studies involving both a straight and a curved section of the radial cavity as shown in Figure 11. Using hydrogen as fuel, the G-loading was varied from 0 to 15000 g's by controlling the mass flow rate and equivalence ratio. In order to capture the effects of G-loading on the completeness of the combustion process, turbulent intensity, and temperature profile, Particle Image Velocimetry (PIV) along with single-line and two-line Planar Laser-Induced Fluorescence (PLIF) were used. The investigation revealed an increase in the turbulent intensity with respect to G-loading. This led to the conclusion that the increase in centrifugal force results in a better mixing, a reduction in chemistry time, and hence an advancement of the combustion process. This conclusion was also underlined via the reduction of the amount of OH in the main flow [23].

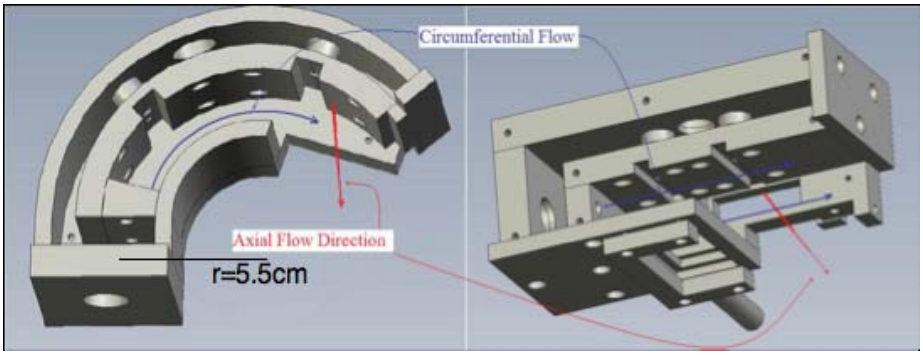

Figure 11. UCC Sections: Curved (Left) and Straight (Right)

In 2009, Lapsa and Dahm investigated the effects of positive and negative high centripetal accelerations (up to 10,000 g's) on both flame propagation and blowout limits using premixed propane –air flames stabilized by backward step. The results of their study could simply be summarized by Figure 12 which illustrates the chemiluminescence and shadow graph images they acquired [24].

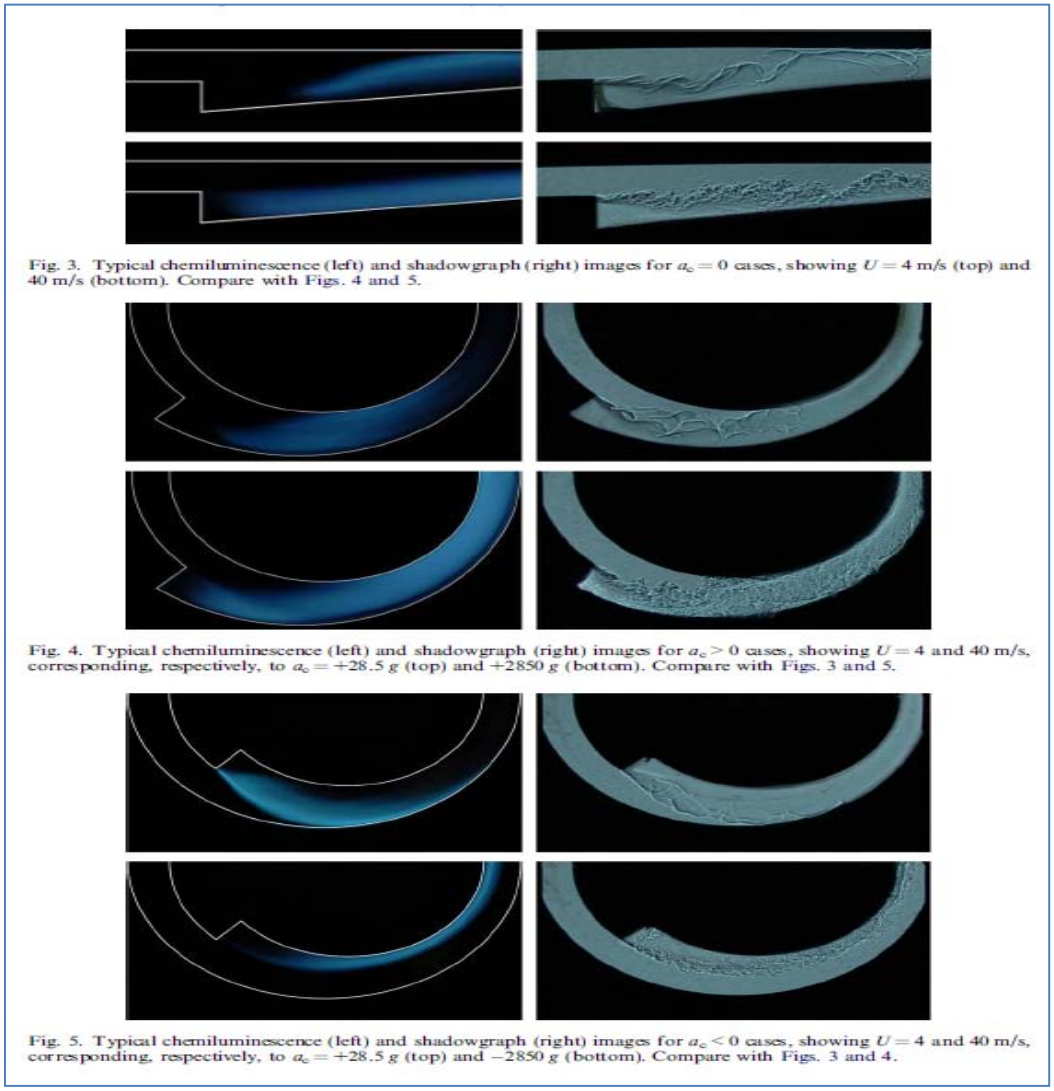

Fig. 3. Typical chemiluminescence (left) and shadowgraph (right) images for $a_c = 0$ cases, showing $U = 4$ m/s (top) and 40 m/s (bottom). Compare with Figs. 4 and 5.

Fig. 4. Typical chemiluminescence (left) and shadowgraph (right) images for $a_c > 0$ cases, showing $U = 4$ and 40 m/s, corresponding, respectively, to $a_c = +28.5\,g$ (top) and $+2850\,g$ (bottom). Compare with Figs. 3 and 5.

Fig. 5. Typical chemiluminescence (left) and shadowgraph (right) images for $a_c < 0$ cases, showing $U = 4$ and 40 m/s, corresponding, respectively, to $a_c = +28.5\,g$ (top) and $-2850\,g$ (bottom). Compare with Figs. 3 and 4.

Figure 12. Chemiluminescence and Shadowgraph Images for ac=0, ac>0, and ac<0

The authors noted that in the case of positive acceleration, the buoyancy forces drove the hot products (with lighter density) to the center of the turn and that the higher the centrifugal

force the better the mixing between hot and cold species was. However, in the case of negative acceleration, the opposite scenario occurred. At higher (in absolute value) centripetal acceleration, the separation between cold and hot gases was more pronounced which resulted in less mixing. For both positive and negative acceleration, the study concluded an overall increase in the flame propagation across the channel. Lastly, the authors discovered that the centripetal force prevented the formation of large scale distortion and turbulence (as can be seen clearly in Figure 12) which resulted in the stabilization of the flame and hence the increase of the blowout speeds [24].

II.3. Literature Review Findings and Unanswered Questions

We deduce from the literature review that a horizontal buoyant jet (whether for positive or negative buoyancy) is subjected to a bifurcation for a Froude number values between 1 and 4. On the other hand, the center plume is suppressed from the core jet and replaced by two side lobes for Froude number less than unity (Reeder *et al.*) [18]. These effects are less pronounced for high values of Froude number (Fr>7) where the jet is momentum driven. Will these observations still hold when a co-flowing air is introduced to the flow field? How will the buoyant jet trajectory change when a co-flowing air stream is introduced? These are some of the relevant and unanswered questions that the current research will attempt to answer.

Based on Subbarao's study [1], the jet's trajectory is characterized by the formation of periodic and aperiodic vortex rings in the presence of a co-flowing air. The periodicity of these structures is more apparent for 260 <Re<900 and 1 <Ri<4. Subbarao, however, was investigating the classical case of a vertical jet. This study will investigate similar parameters, however with initially a horizontal jet and later with a G-loaded jet. Will the horizontal jet in a

co-flow of air show the same structures? If so, is it possible to pick up the frequency of some of these periodic structures in the presence of a co-flow?

Furthermore, we claim that in the circumferential cavity of the UCC, the cold unburned fuel keeps circulating and being pushed outward until it is completely burned. This fact was partially validated by Dahm's study [24] which revealed that positive acceleration (positive g's) forced the heavier gas to move outward. Dahm's research though was performed in a combusting environment and did not consider the presence of a sustained flow. Then, how would changing these conditions affect the direction in which the cold gas goes?

Investigating the behavior of the buoyant jet in the presence of a co-flow is one of the fundamental objectives of this study. Particularly, this situation figures during the fuel injection into the circumferential cavity. Based on Kumar and Yuan's study [20], a hot flow injected in a cold medium penetrates deeper than when a cold flow is injected into a hot environment due to the absence (and respectively presence) of opposing buoyancy. In addition, at the same Reynolds number (as a cold jet), the hot jet exhibits higher velocity since it has lower density. This study however does not provide any details on the progression of the injected jet with respect to time. Will it stay deeper in the cavity or eventually move upward? Sherif *et al.*'s study [21] on the other hand, concluded that the increase in the jet to air velocity ratio resulted in a more pronounced mixing between the jet and the cross-flowing air. Will this observation, however, hold true in a more complex configuration where G-loading and co-flowing air effects are introduced simultaneously?

The relevance of this research stems directly from the need to answer all these questions which go in parallel with the list of objectives previously set in chapter one of this report.

III. Methodology

The methodology developed and executed for this research is outlined in this chapter. Simply put, it entails setting up and performing three separate experiments that ensure the collection of adequate data to answer the questions outlined in the research objectives. The first experiment will be associated with properly setting up the FRS technique which requires the characterization of the absorption well of the molecular filter to be used in the study. The second and third experiments involve the use of FRS technique to collect jet concentration data using two different configurations. The first configuration is based on a horizontal buoyant jet (helium and CO_2) in a co-flow of air. The second configuration (third experiment) involves the use of a UCC like curved section with a circumferential cavity where air is flowing around a jet (CO_2) introduced in the cavity using a curved tube. The idea is to create an environment and a flow structure that mimics the flow field within the UCC circumferential cavity. It is important to note that all these configurations will have optical access from different views to allow the capture of FRS images. These experiments along with the equipment are described in the following sections.

III.1. Equipment

The following sections will describe the equipment used in this research program. With the exception of the mass flow controllers used in the third experiment for high flow measurements, the same equipment is used for both the second and third experiment.

III.1.1. Laser

The laser used in this experiment is the Coherent VERDI Laser DPSS High Power CW V12 manufactured by Coherent Inc. The laser outputs a maximum power of 12 W at a wavelength of 532 nm. The lowest power it outputs is about 0.01 W. The laser system consists

of the laser head, a power supply and a water cooling unit as shown in Figure 13 below. The laser's wavelength can be tuned by changing the laser's etalon temperature. Using the menu display located on the power supply, the user can navigate through the different options. The power can be regulated directly using a knob located next to the menu display. The laser can be turned on using first an *on/off* switch on the back of the power supply, an *enable/standby* key , and a shutter switch located below the menu display.

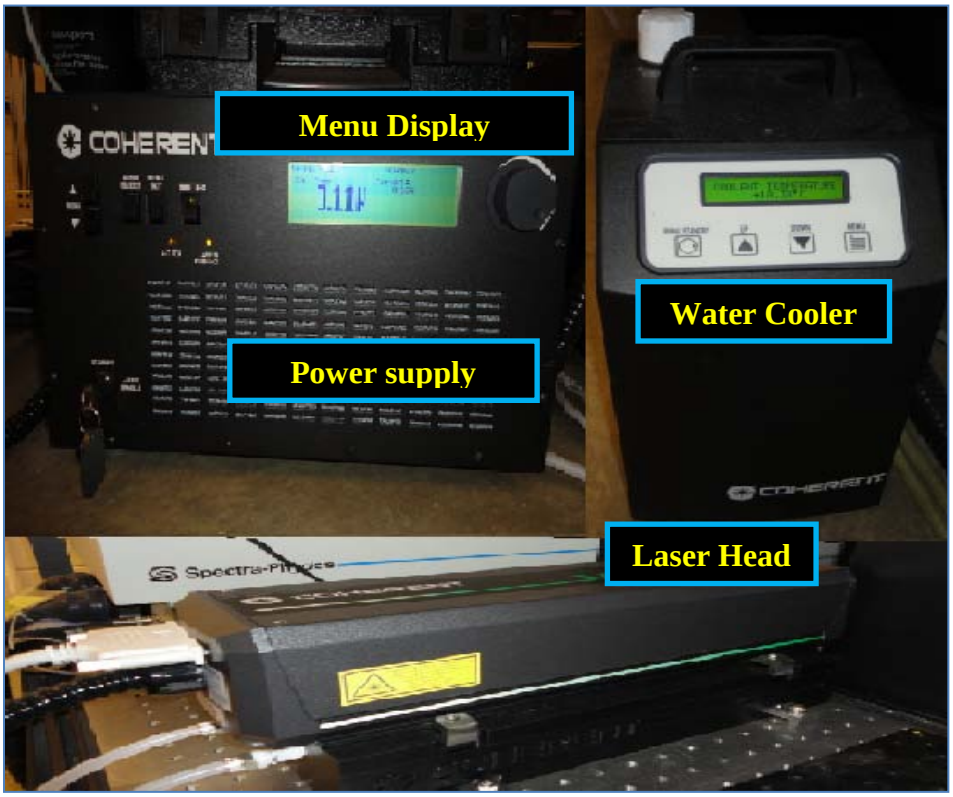

Figure 13. Coherent Verdi V12 Laser System

III.1.2. Iodine Filter

As shown in Figure 14, the molecular filter used in this experience consists of a 3.5 inch glass tube filled with iodine and a protective aluminum cylindrical case. It is manufactured by Innovative Scientific Solutions Inc. (ISSI) of Dayton, Ohio.

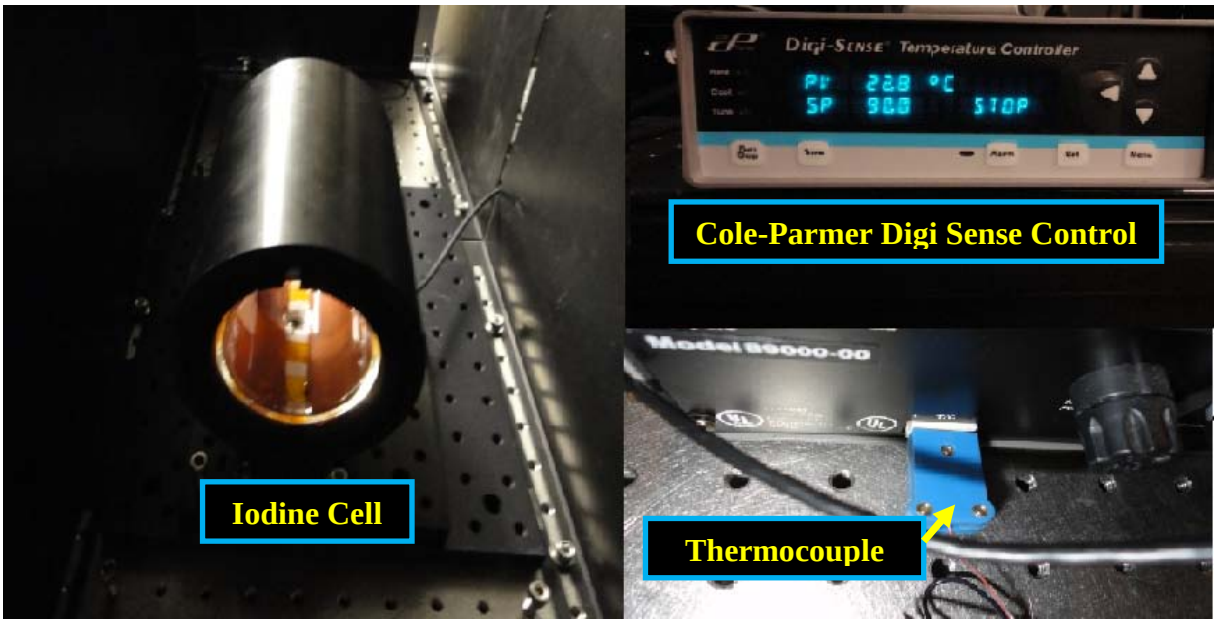

Figure 14. Iodine Filter and Accessories

The filter is attached to a power supply cord and a thermocouple of type K. The thermocouple is used to set the temperature inside the filter and is connected to a Cole-Parmer Digi Sense control box.

III.1.3. Power meters

Figure 15. Orion, Vega, and Coherent Fieldmaster Power Meters

Three power meters were used during the iodine filter characterization experiment (Figure 15). Two of them (the Orion TH and the Coherent Fieldmaster) were used to acquire the reference power and the transmitted power values. The third power meter was used to check the consistency of the measurements during the experiment. Each power meter is attached to a sensor and a power supply. A power meter sensor is shown in Figure 16 below. The Orion and Vega meters are manufactured by the OHIR Laser Measurement Group. According to their respective manuals, the Orion TH meter operating range is between 0.1 μW and 20 kW. The Vega however measures values in range of nW and up to kW. Because the meters were of different types, calibrating them was a necessary task. The meters were initially zeroed out with the laser turned off. The Coherent Fieldmaster power meter has an accuracy of ±2%.

Figure 16. Power Meter Sensor

III.1.4. Mass Flow Controllers

For relatively low jet velocity measurements, the Brooks Instrument 5850i mass flow controller shown in Figure 17 was used to control the jet mass flow rate to ±0.1SLPM. This flow controller was calibrated for air at maximum flow rate value of 30 SLPM. For high flow measurements, the Brooks Instrument 5853i mass flow controller, shown in Figure 18, was used instead to control the jet's mass flow rate to ±0.5 SLPM. This mass flow controller, however, was calibrated for propane at a maximum flow rate value of 200 SLPM. The same user interface (shown in Figure 17) was used to display and control the jet's mass flow rate value.

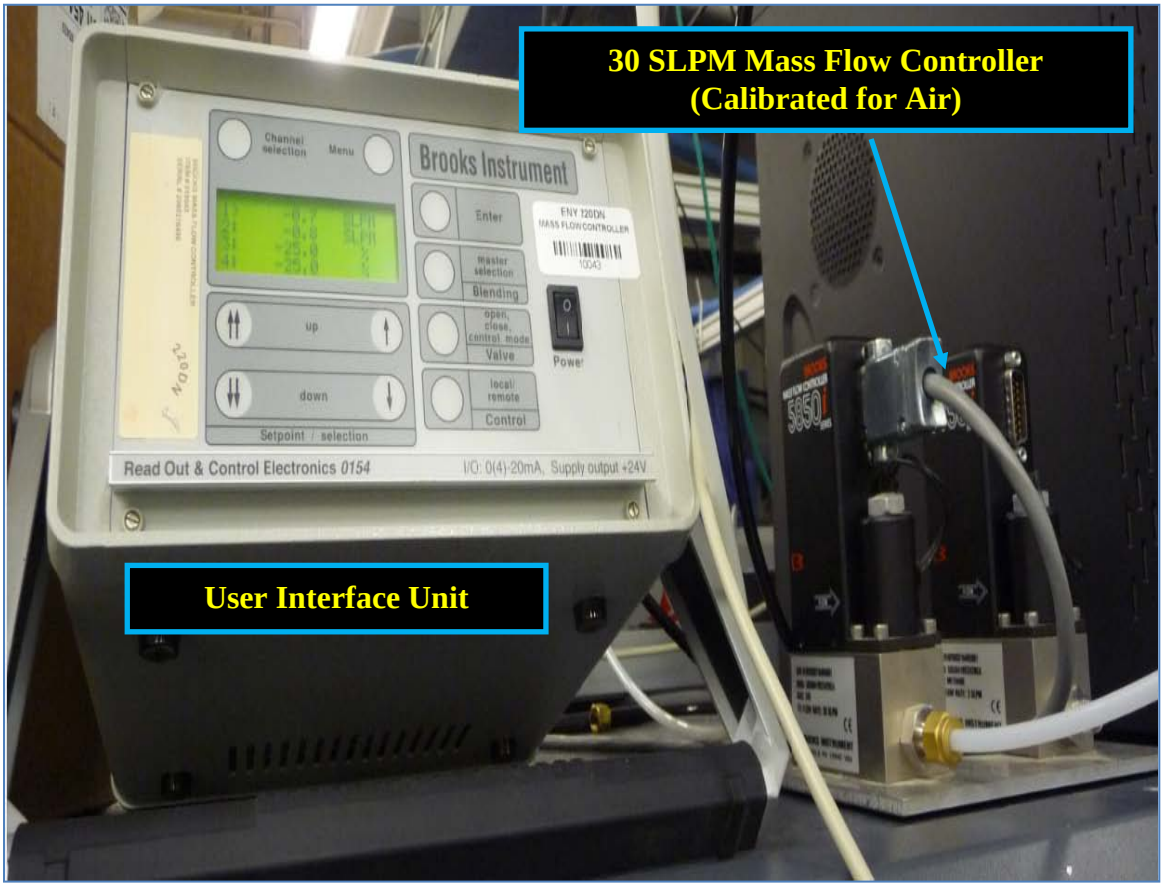

Figure 17. The Brooks Instrument 5850i Mass Flow Controller

Figure 18. The Brooks Instrument 5853i Mass Flow Controller

For this research however, both mass flow controllers were intended to be used for Carbon Dioxide (CO_2) gas and helium. Equation (12) which is provided by the manufacturer is used to relate the output reading and the actual value of the mass flow rates of the CO_2 or helium jet.

$$Actual\ Gas\ Flow\ Rate\ (CO_2\ or\ \text{helium}) = Output\ reading \times \frac{factor\ of\ the\ new\ gas\ (CO_2 \text{or helium})}{factor\ of\ the\ calibrated\ gas\ (air\ or\ propane)} \quad (12)$$

As an example, when plugging the corresponding values for the conversion factors for the cases when the Brooks 5850i were used for a CO_2 jet, the relationship of Equation (12) becomes Equation (13):

$$Output\ reading = 1.291 \times Actual\ Gas\ Flow\ Rate\ (CO_2) \quad (13)$$

III.1.5. Camera

Images used in this study were collected using a monochrome Phantom V12.1 (shown in Figure 19) manufactured by Vision Research. This high speed camera enables image capture at up to 1,000,000 Hz. For this research, data was captured at 400 Hz for the CO_2 (and 80 Hz for helium) jet allowing the capture of images at an adequate signal to noise ratio as will be explained later on in this thesis report. In addition, this camera was also equipped with a Nikon 85mm lens with an f stop of 1.8. The camera has a maximum resolution of 1280x800 and an exposure time down to 1μsec. All images have a pixel depth of 16 bit. Figure 20 illustrates a snap shot of the camera software used to input the camera settings and initiate the data collection.

Figure 19. Phantom V12.1 Camera

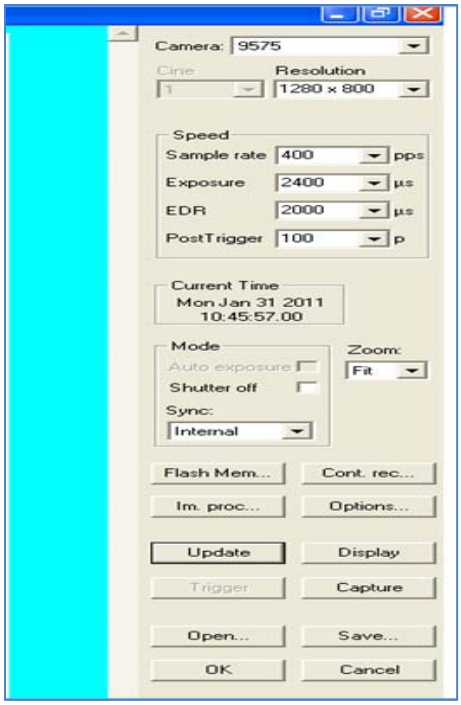

Figure 20. Camera User Interface Software Screen Shot

III.1.6. Optics

Various optical tools were needed in this research to direct the laser beams to the test section and control its power. The optics includes mirrors, beam splitters, density filters and others as it will be discussed in this section.

III.1.6.1. Mirrors

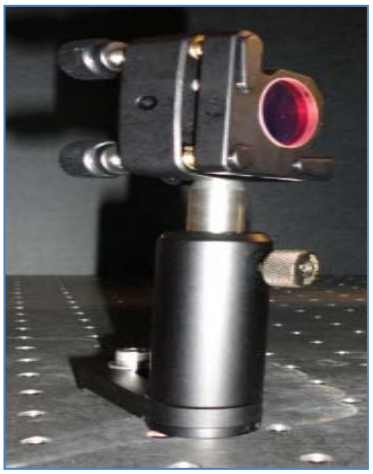

Figure 21. High Reflective (HR) Mirror

High reflective mirrors were used in all three experiments to turn the beam 90°. These mirrors (shown in Figure 21) reflect 99% of the beam while letting only 1% goes through. The mirrors are manufactured by Lattice Electro Optics (LEO), Inc.

III.1.6.2. Beam Splitters

The objective behind using a beam splitter (whether the 50-50 or the 90-10) is to reduce the power of the beam to a predefined percentage. The beam splitters (or often called beam samplers) used in the first experiment (the iodine filter characterization) are shown in Figure 22. Both beam samplers are made by LEO and are designed to be used with a laser of a wavelength value around 532 nm. The 50-50 beam splitter is a 2 inch diameter sampler. It divides the beam into two perpendicular beams transmitting 50% of the incident power each. The 90-10 power is a regular glass plate that allows 90% of the power to pass through while reflecting the remaining 10% at a 90° angle.

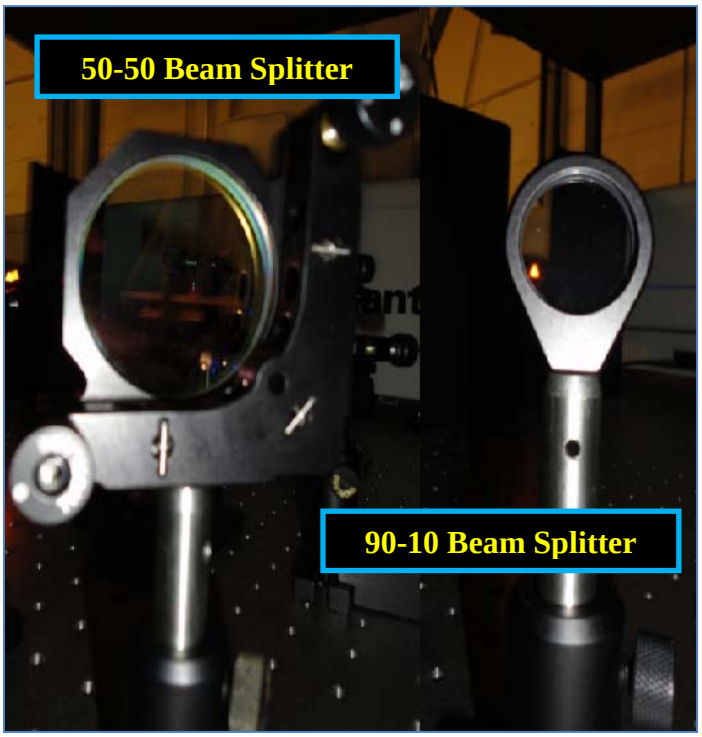

Figure 22. Beam Splitters (or Samplers)

III.1.6.3. Aperture

The aperture was used in all three experiments. The intent behind using it is to block the unwanted beam spray as shown in Figure 23. The laser power was set during the measurements at 12 W. It is important at this high power to intercept and block any stray beams to avoid any risks of burning any surface the laser may be in contact with. The aperture is manufactured by ThorLabs.

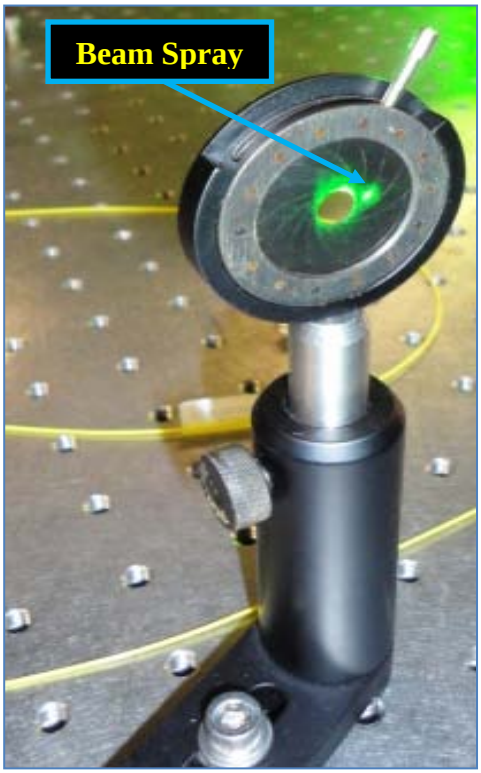

Figure 23. Aperture and Unwanted Beam Spray

III.1.6.4. Spherical lenses

Two spherical lenses (shown in Figure 24) were used in the iodine filter characterization experiment. Both lenses were manufactured by LEO. The first one (on the right) is a 1 inch diameter, +25 mm spherical lens used to create a sheet of laser in front of the iodine filter to allow for maximum passage through the inner volume of the filter. The 25mm is the focal length

and indicates that the beam will be focused to a point at 25 mm behind the lens. Beyond the 25 mm, the beam is turned into a sheet as shown in Figure 25. The second spherical lens is a 2 inch diameter, +200 mm lens and is used to focus the sheet of laser back to a point after passing through the filter before it is intercepted by the power meter sensor.

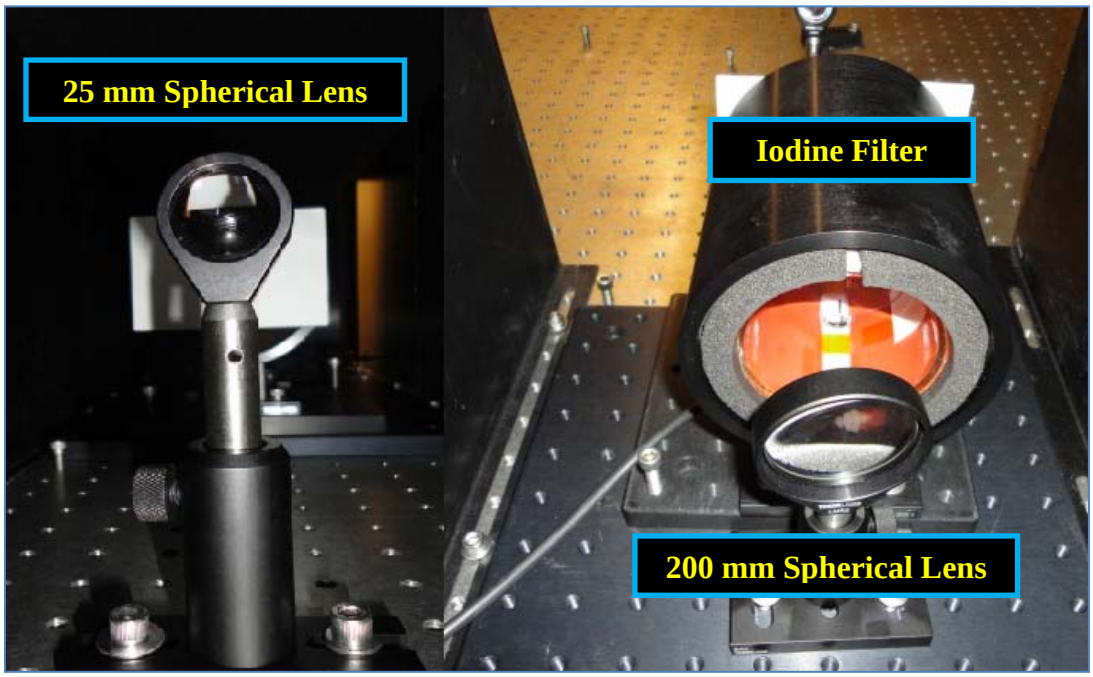

Figure 24. Spherical Lenses

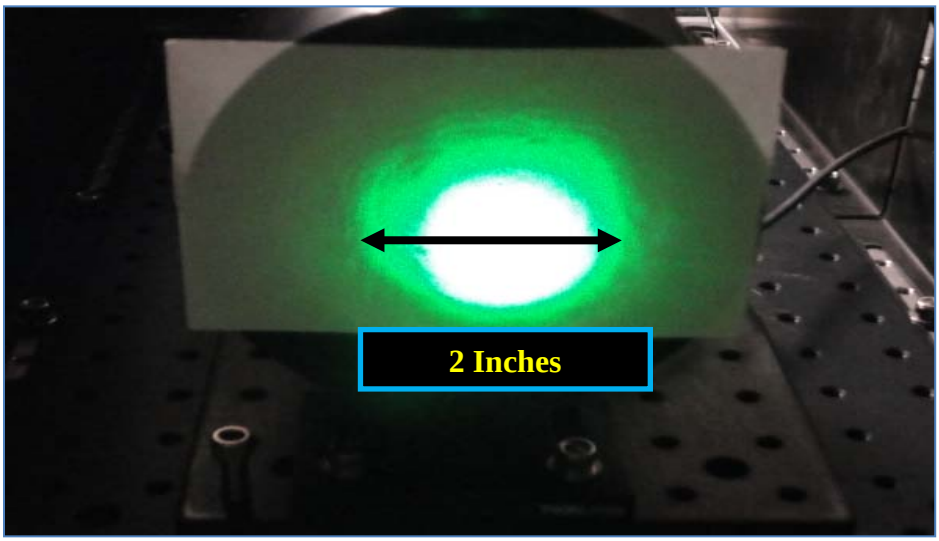

Figure 25. Sheet of Laser in front of the Iodine Filter

III.1.6.5. Density Filters

Two density filters were employed during the first experiment to further reduce the power of the incident beam. One density filter with an opacity of 2.0 (98% absorption) is placed in front of the wave meter sensor while the other one, with an opacity of 3.0 (99% absorption), was positioned in front of the aperture in the way of the main beam directed toward the filter. The two filters are manufactured by LEO. Figure 26 below shows one of the density filters used for this experiment. Similarly to the other optical tools, the density filter is mounted on a ThorLabs post.

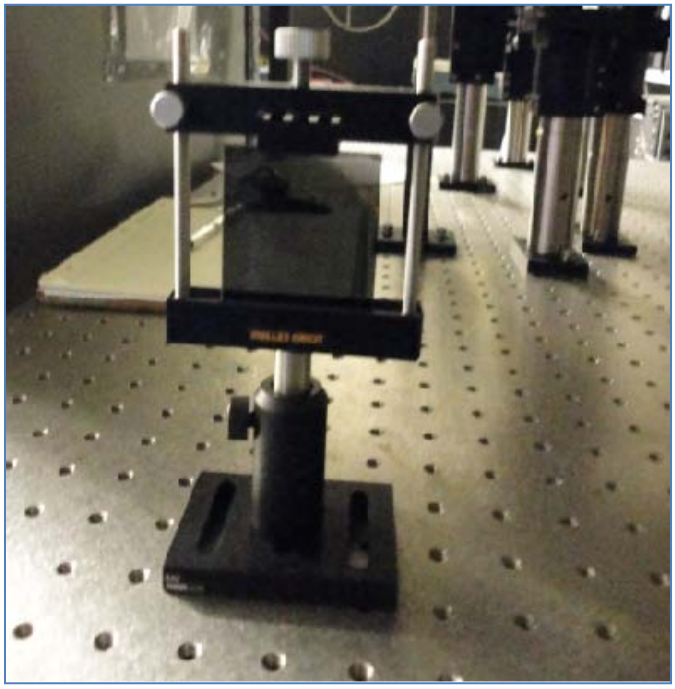

Figure 26. A LEO Density Filters

III.1.7. Wave meter and Accessories

In order to keep track of the laser's wavelength, two different wave meters were used throughout this research. The first wavemeter used for the iodine filter characterization is a HighFinesse WS-7 wave meter shown in Figure 27. The wave number (or wavelength) values

were acquired via the WS-7 software provided by the company TOPTICA. According to the WS-7 user's manual, the device is capable of measuring wavelength values in the range between 192 nm and 2250 nm. In addition, it can be used for both pulsed and continuous wave lasers. When operating between 370 nm and 1100 nm, the device has an accuracy of 60 MHz which corresponds to approximately 0.00005 nm.

Figure 27. WS-7 Wavemeter Unit

The second wave meter is the Brsitol Model 621 wavemeter. The Bristol wavemeter was used in the second and third experiments. This wavemeter has comparable characteristics as the WS-7 wavemeter mentioned earlier. Both wavemeters were connected to a computer using the corresponding device's USB interface. In addition, they were both used in conjunction with a fiber optic cable attached to a calorimeter as shown in Figure 29. A screenshot of the computer screen during the acquisition of the data when using the WS-7 wavementer (as an example) is shown in Figure 30.

Figure 28. Bristol (Model 621) Wavemeter

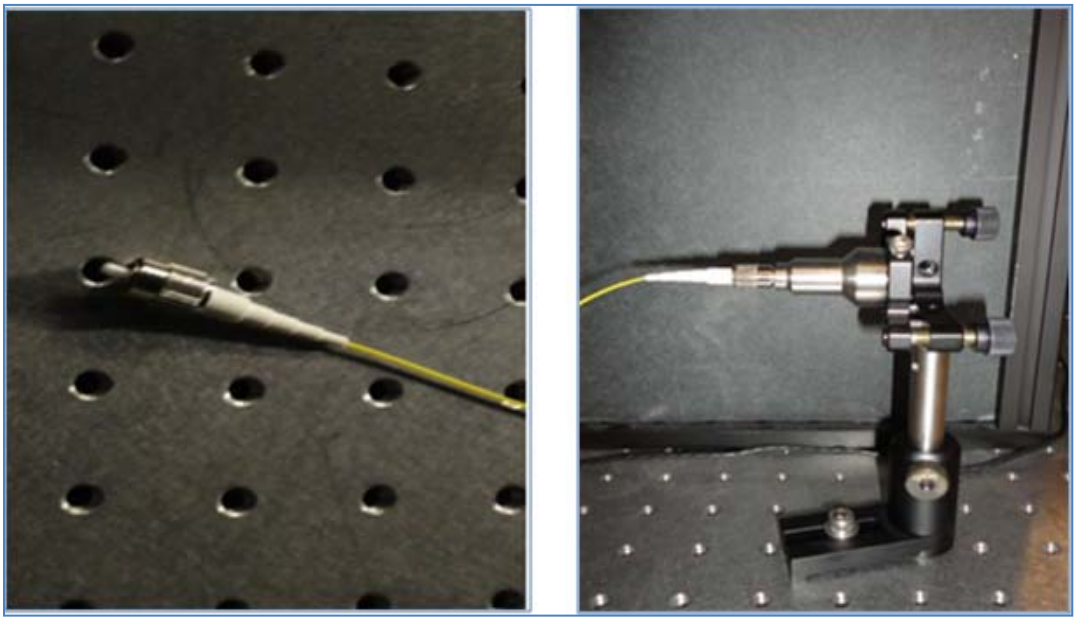

Figure 29. Laser Calorimeter (Right) and Fiber Optic Cable (Left)

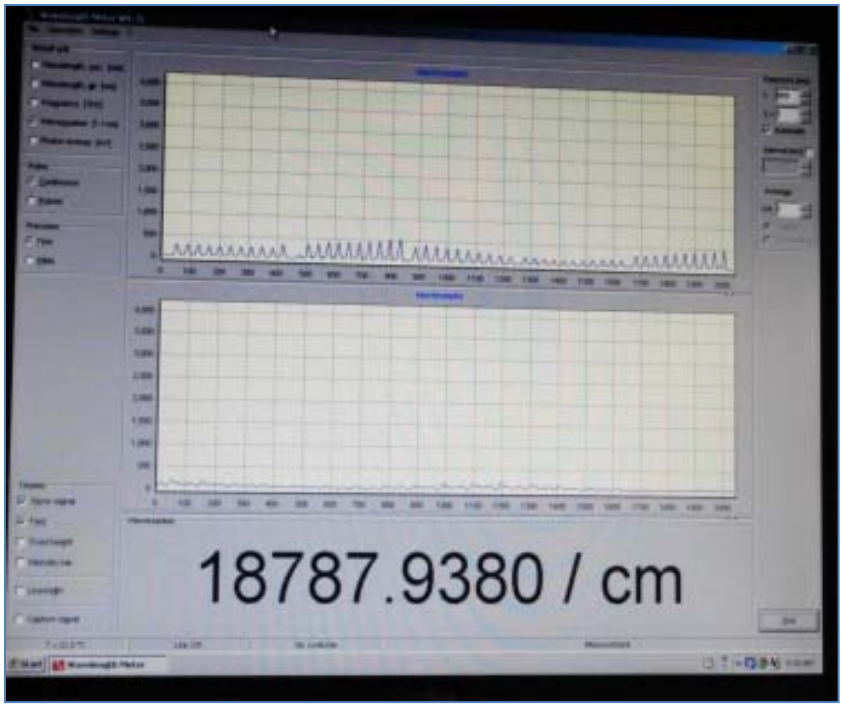

Figure 30. WS-7 Wavemeter Computer Interface and Data Display (currently the wavenumber is 18787.9380 cm^{-1})

III.2. Experiment # 1: Iodine Filter Characterization

As mentioned in the literature review section, the molecular filter characterization is essentially plotting the absorption well within which there will be blocking of the incident light. Based on the diagram of Figure 5, maximum absorption (about 0% transmission) occurred for a small range of frequency between a lower boundary value of wavenumber (or wavelength or frequency) ν_{min} and an upper boundary value ν_{max} . The well is usually centered at a reference frequency νo. The objective of the filter characterization experiment is therefore, determining values of ν_{min} and ν_{max} of the absorption well centered at about 532 nm which corresponds to the wavelength of the laser in use in this research. When testing, tuning the incident laser to a frequency between ν_{min} and ν_{max} ensures maximum blocking of undesired scattered light and background noise. The experimental set up used to characterize the iodine filter is illustrated in Figure 31 and Figure 32.

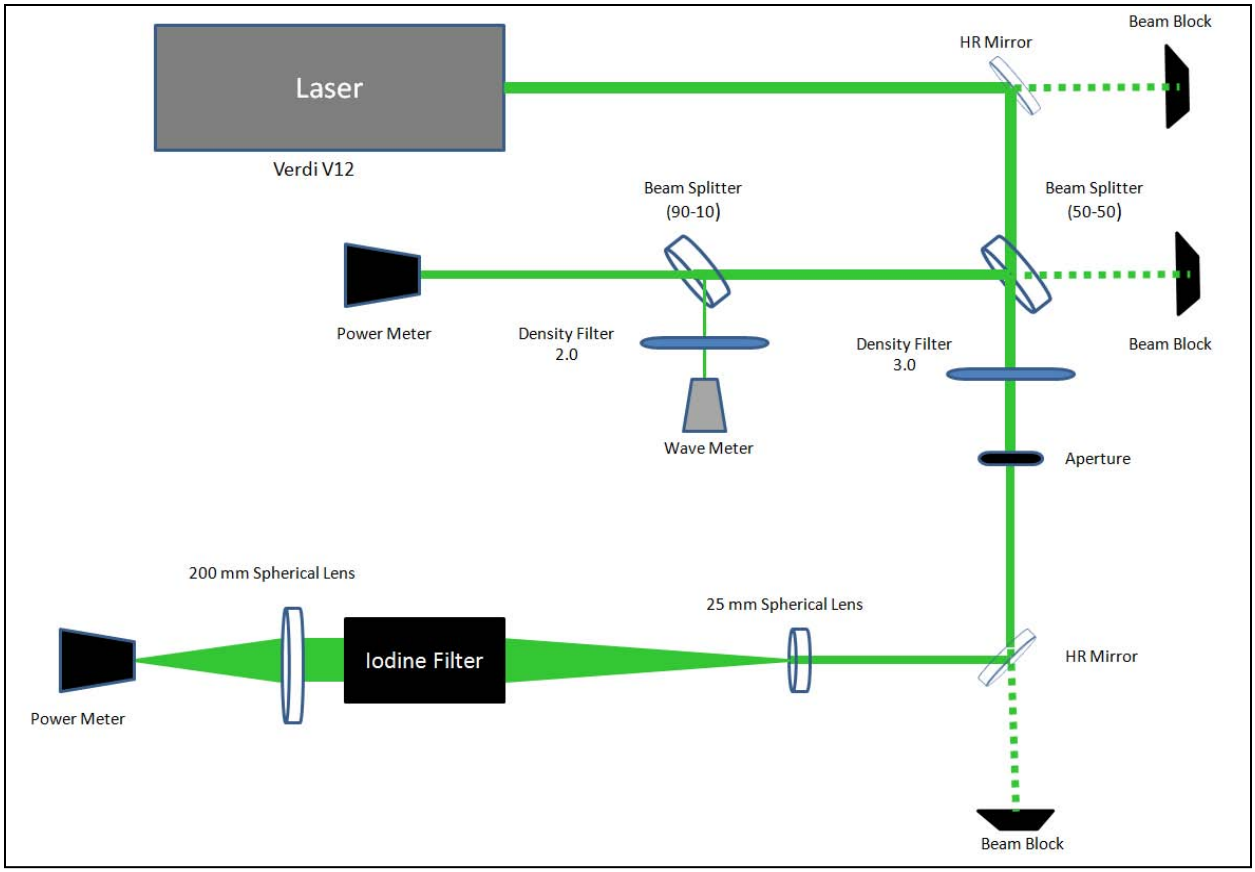

Figure 31. Iodine Filter Characterization Setup Diagram

The incident beam's trajectory is turned 90^{o} toward the iodine filter area using a high reflective mirror. It then goes through two beam splitters (a 50-50 and 90-10) to reduce its power down to a value that is within the range of operation of the wave meter. 45% of the beam's power is intercepted by the first power meter. The light then passes through a density filter to further reduce its power and an aperture to block the undesired stray beams. The beam then hits the surface of a mirror and turns 90^{o} facing the front of the iodine filter. A sheet of laser (as shown in Figure 25) is created in front of the filter using a 25 mm spherical lens. Finally, the light exiting the filter passes through a 200 mm spherical lens which focuses it back to a single point before it is intercepted by the second power meter.

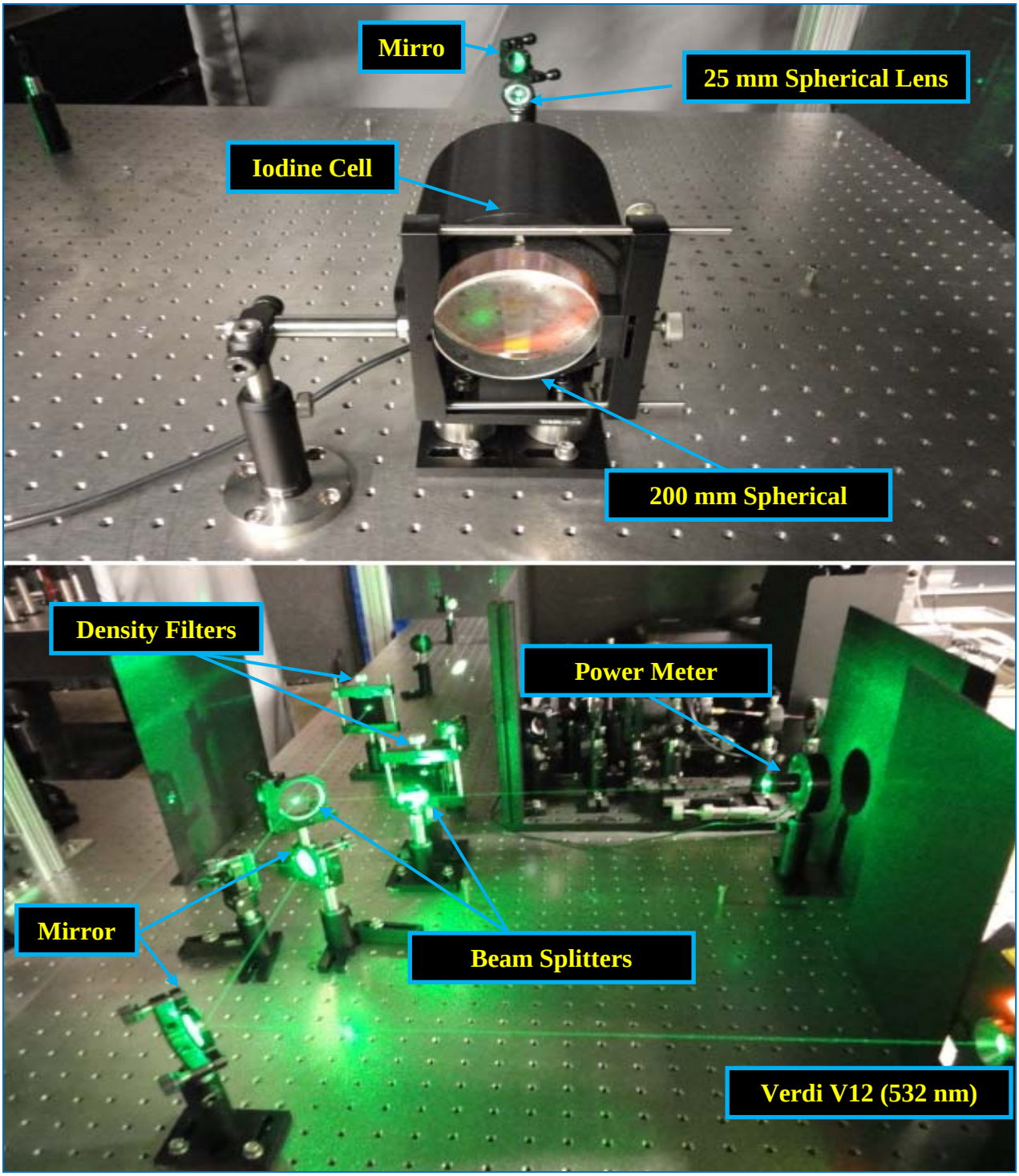

Figure 32. Photos Showing the Iodine Filter Characterization Experimental Set Up

The construction of the iodine filter absorption well is essentially plotting the percentage of the transmitted power as a function of the wave number (or the wavelength, or the frequency).

For that purpose, the power of the laser exiting the iodine filter was measured and the ratio of the output to input power was calculated as the wavelength was changing. The wavelength can be changed by varying the etalon temperature of the laser. This could be achieved using the software interface associated with the V12. According to the user's manual, the etalon temperature can be varied between 35 ^{o}C and 75^{o}C. For example, the command to set the etalon temperature to 40^{o} is given by:

> >et = 40

The command to check the currently set etalon temperature is:

>>?est

It is important to note though that the wavelength (or the wave number) values decrease spontaneously over time. Starting with a high value of wave number (way larger than the range where the well is) allows for a slow drift that could be taken advantage of to record the values of the corresponding transmitted power as the wave number decreases. This approach was used for the iodine filter characterization in order to avoid changing the etalon temperature and obtain more consistent results. For this experiment, the incident power was set at 1.04 W. According to the V12 user's manual, the power has to be greater than 5 % of the maximum output (12 W) to avoid driving the laser to enter an alignment mode (where the power could not be accurately measured). As mentioned in the Second Chapter, the well's shape and depth change with respect to the iodine cell temperature. Three different cell temperatures (40 ^{o} C, 60 ^{o} C, and 90^{o} C) were investigated during this experiment.

III.3. Experiment # 2: Horizontal Buoyant Jet in a Co-flow

The experimental set up to collect scattered light images off of a horizontal buoyant jet in a co-flow is shown in Figure 33. In order to investigate the effects of both positive and negative buoyancy on the jet's trajectory and behavior, both helium and Carbon Dioxide (CO_2) jets were respectively used. Because the two gases have significantly different densities, two different configurations of the plenum in which air flows, were used to create comparable test conditions. The plenum section (for both helium and CO_2 configurations) was designed by Mr. Samuel Raudabaugh. In order to create comparable test conditions for these two configurations, the exit area of the helium configuration plenum is about 60% smaller than that of CO_2 as it could clearly be noticed when comparing Figure 34 and Figure 35. The experimental set up however, is essentially the same for both configurations.

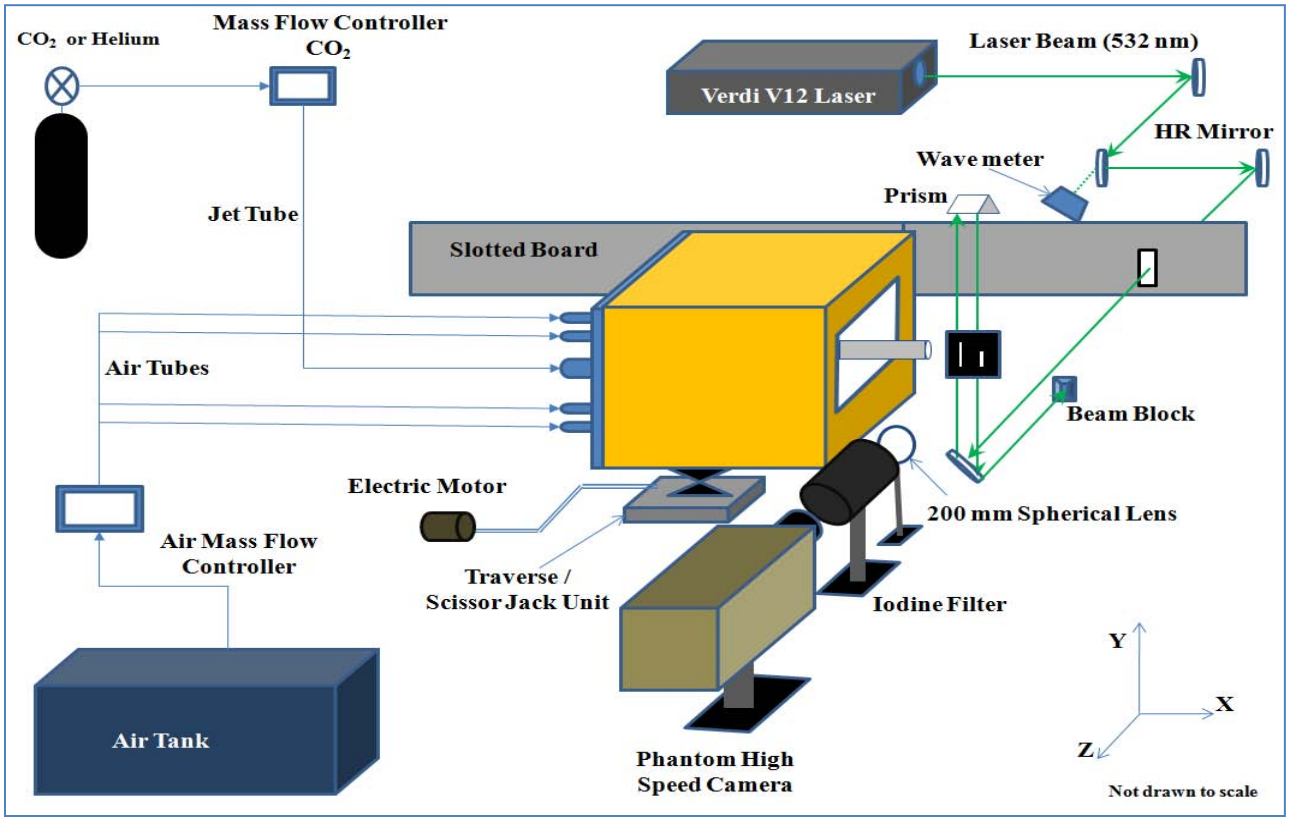

Figure 33. Diagram of Horizontal Buoyant Jet Set Up

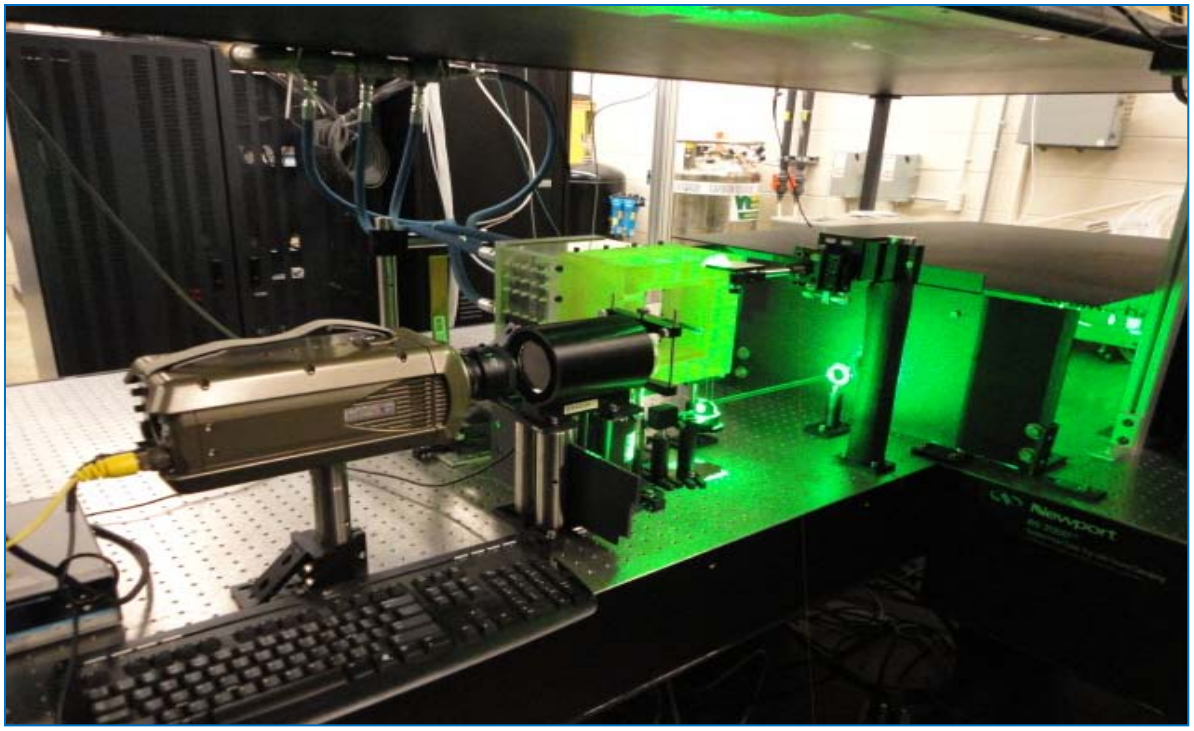

Figure 34. Horizontal Buoyant Jet Set Up Photo for the CO_2 Configuration

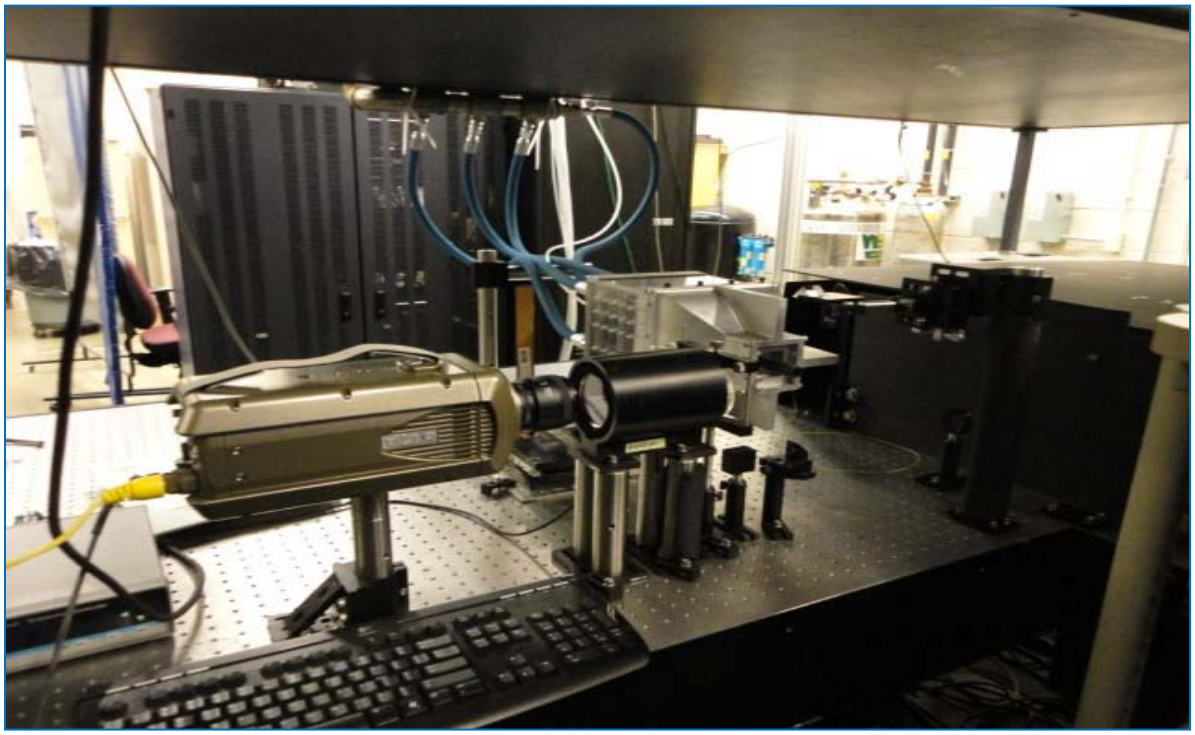

Figure 35. Horizontal Buoyant Jet Set Up Photo for the Helium Configuration

For both configurations (helium and CO_2), the core jet flow is provided by a stainless steel tube whose diameter can be varied to alter the Froude number and Reynolds number values. The Brooks Instruments 5850i mass flow controller was used to control the jet mass flow rate. The co-flow was delivered from an air tank through a mass flow controller that could be adjusted to ±0.01 kg/min. Air then entered a plenum made of Plexiglas via four orifices at which were placed four washing nozzles to ensure a uniform flow of air. The co-flow passed through a honeycomb screen with 9.5 mm openings (as shown in Figure 36) prior to passing through a converging duct (the yellow box for the CO_2 configuration and the metal one for the helium case). The Plexiglas tank was sealed at one end using a 0.375'' thick metal plate. As shown in Figure 36, a PVC fitting (going through the metal plate) was used to feed in the CO_2 (or helium) to the stainless tube.

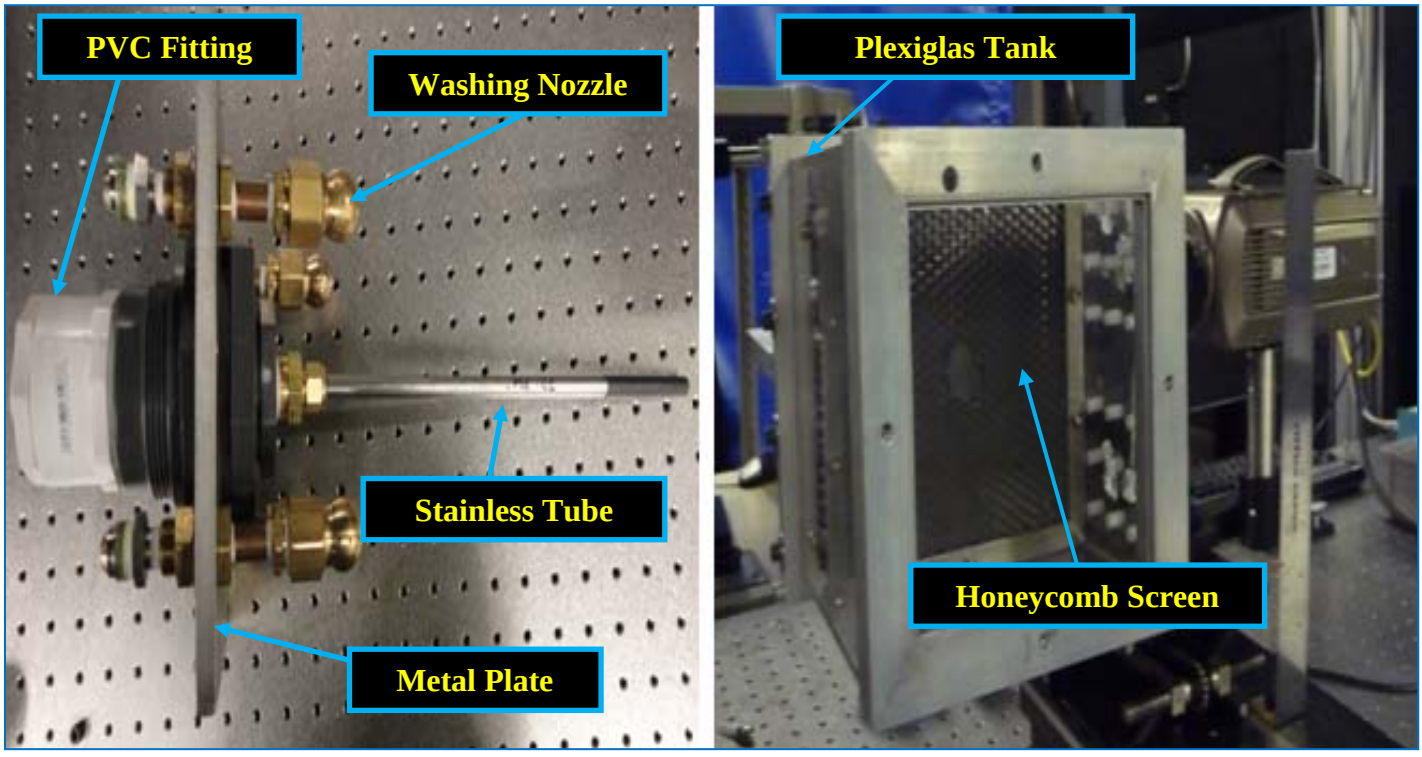

Figure 36. Equipment Used to Feed in Both the Jet (CO_2 and Helium) and Air.

As mentioned earlier, the laser used for this study was a Coherent 12 W CW Verdi V12 with a wavelength around 532 nm. As shown in Figure 33, the beam was routed to the test section using four highly reflective (HR) mirrors at 532 nm. The closest mirror to the tube directed the laser vertically to a prism that reflected the beam back to the same mirror and then to a beam block. This created two vertical laser beams intersecting with the jet and the co-flowing air. The intent behind using two laser beams as opposed to a laser sheet (as used in previous FRS studies) was to maintain the high power of the beams to maximize the scattered light intensity known to be proportional to the incident light intensity. Using the Phantom V12.1 high speed camera, data was captured at 400 Hz for the CO_2 (and 80 Hz for the helium) jet allowing the capture of images at an adequate signal to noise ratio. The camera has a maximum resolution of 1280x800 and an exposure time down to 1μsec. The camera was focused at the area of intersection between the laser beams and the gases (both the jet and the co-flowing air).

Before the scattered light was captured by the camera, it was filtered by the iodine cell positioned in front of the camera. The temperature inside the filter was controlled by a Cole-Parmer Digi Sense control box. The goal was to ensure that most of the scattered light (broadened and shifted) fell outside the absorption well of the filter while ensuring near total absorbtion of the incident signal itself, the background noise, and Mie scattering (due to particles). In addition, a 200 mm spherical lens was placed in front of the iodine filter to increase the effective focal length of the camera allowing for a better focus and hence a better spatial resolution. The Bristol (Model 621) wavemeter (as shown in Figure 28) monitored the wavelength of the laser to ensure maximum absorbance of background noise by the filter. Further, a slotted board minimized the background noise before reaching the filter.

In order to enable data collection at different stream-wise and vertical locations a traverse/ scissor jack unit was employed. As shown in Figure 37, the scissor jack (which is attached to the Plexiglas tank) allowed for a maximum vertical range of 2.25''. The traverse allowed for a horizontal displacement of 2.3''. The unit was controlled using a joy stick, an Anilam Wizard 150 power supply and a Questar digital readout.

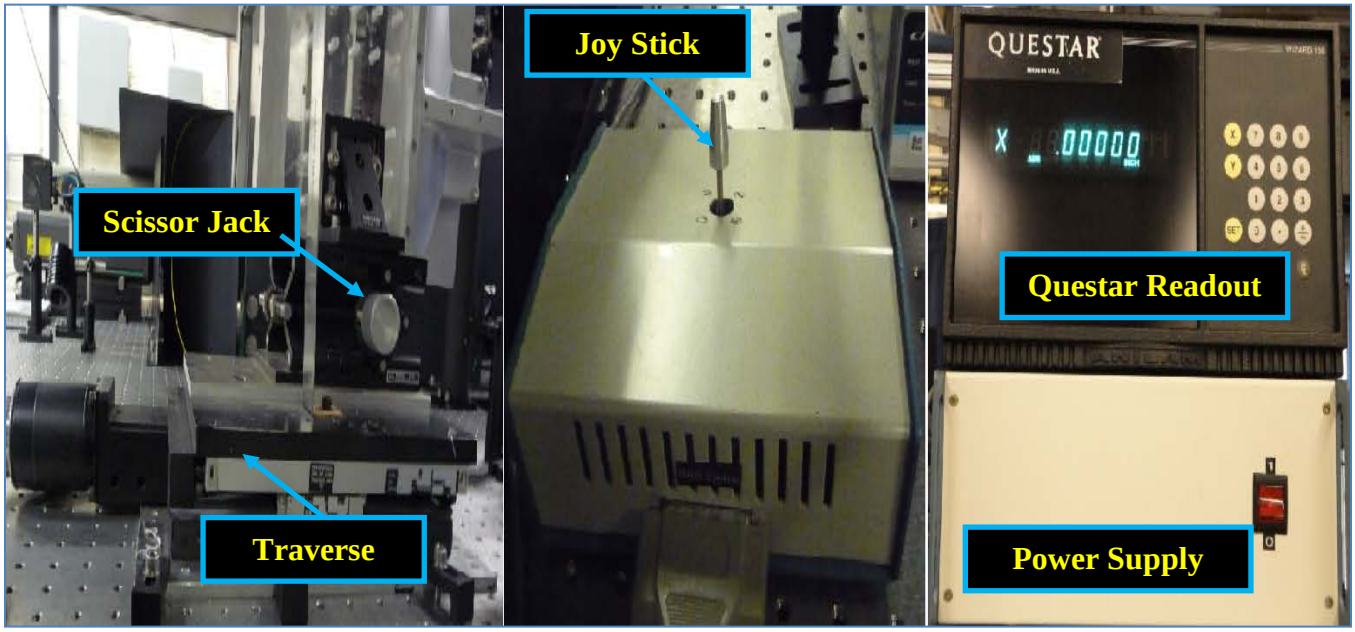

Figure 37. Traverse and Scissor Jack Unit and Accessories

III.4. Experiment # 3: G-loaded Buoyant jet in a Co-flow

The experimental set up to collect scattered light images off of a G-loaded buoyant jet in a co-flow is shown in Figure 38. The set up for this experiment involved, in general, the use of the same equipment of the second experiment (horizontal jet). The straight configuration consisting of the cubic plenum and the horizontal tube used in the second experiment, were replaced by an SLA curved hallow section in which flowed air around a bent stainless tube as shown in Figure 39 and Figure 40. The shape of this curved section was designed by Mr. Jacob Wilson who based his drawings on the actual UCC rig used in the COAL lab. The SLA section, of which a

CAD drawing is shown in Figure 41, has a radius of curvature 38c m (15 inches) and a squared cross section with 4.8 cm (1.9 inches) on each side. Three different tubes of different inner diameters of 0.635 cm (0.250 inches), 0.775 cm (0.305 inches), and 1.09 cm (0.430 inches) were used during this experiment. Due to the flow of the gases (both co-flowing air and the jet) along the curvature of the section and the stainless tube, the gases were subjected to a normal outward acceleration. Carbon Dioxide was used as a jet for this experiment to easily separate the effects of buoyancy (pulling the jet down) and those of the G-loading (expected to push the CO_2 molecules outwards).

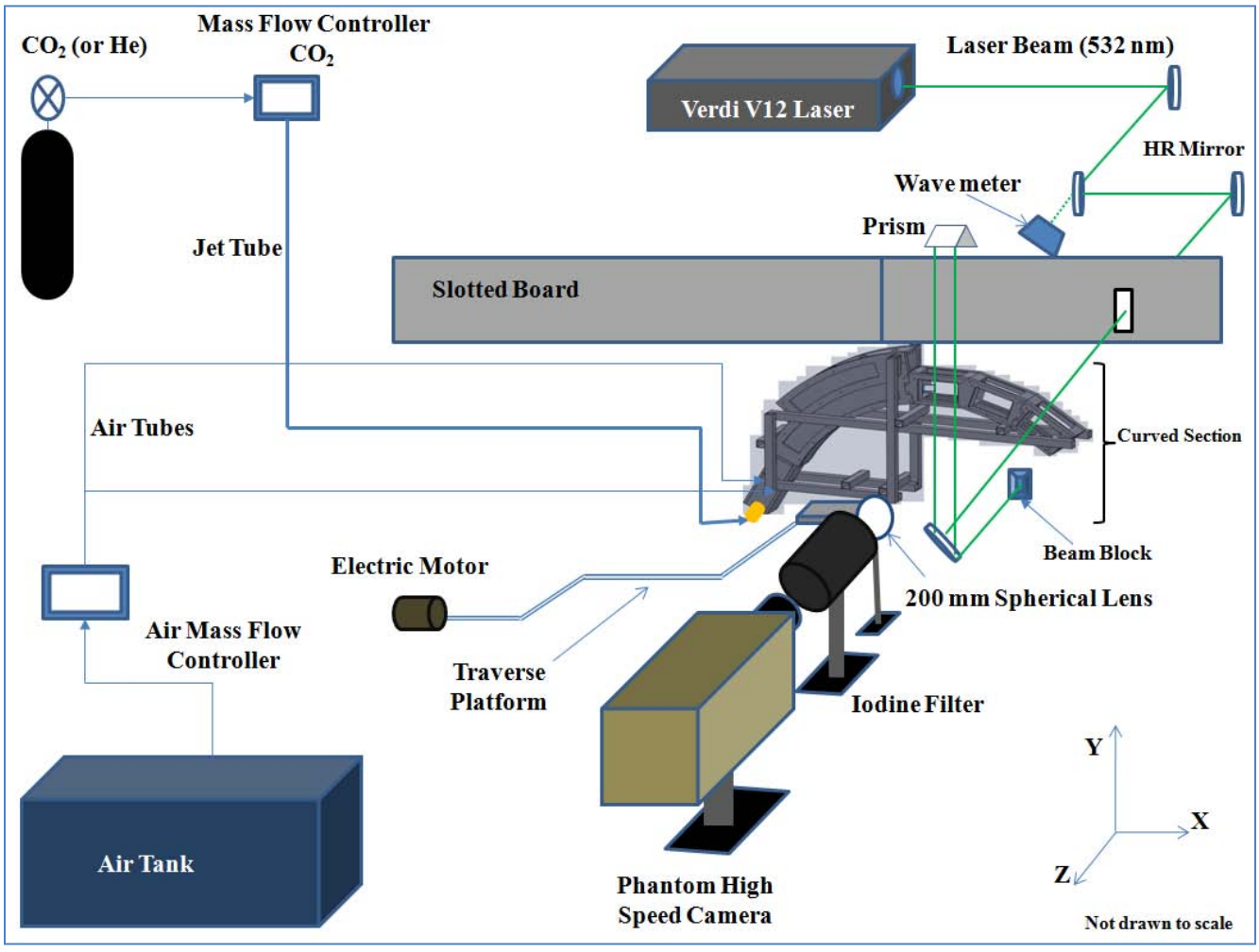

Figure 38. Diagram of G-loaded Buoyant Jet Set Up

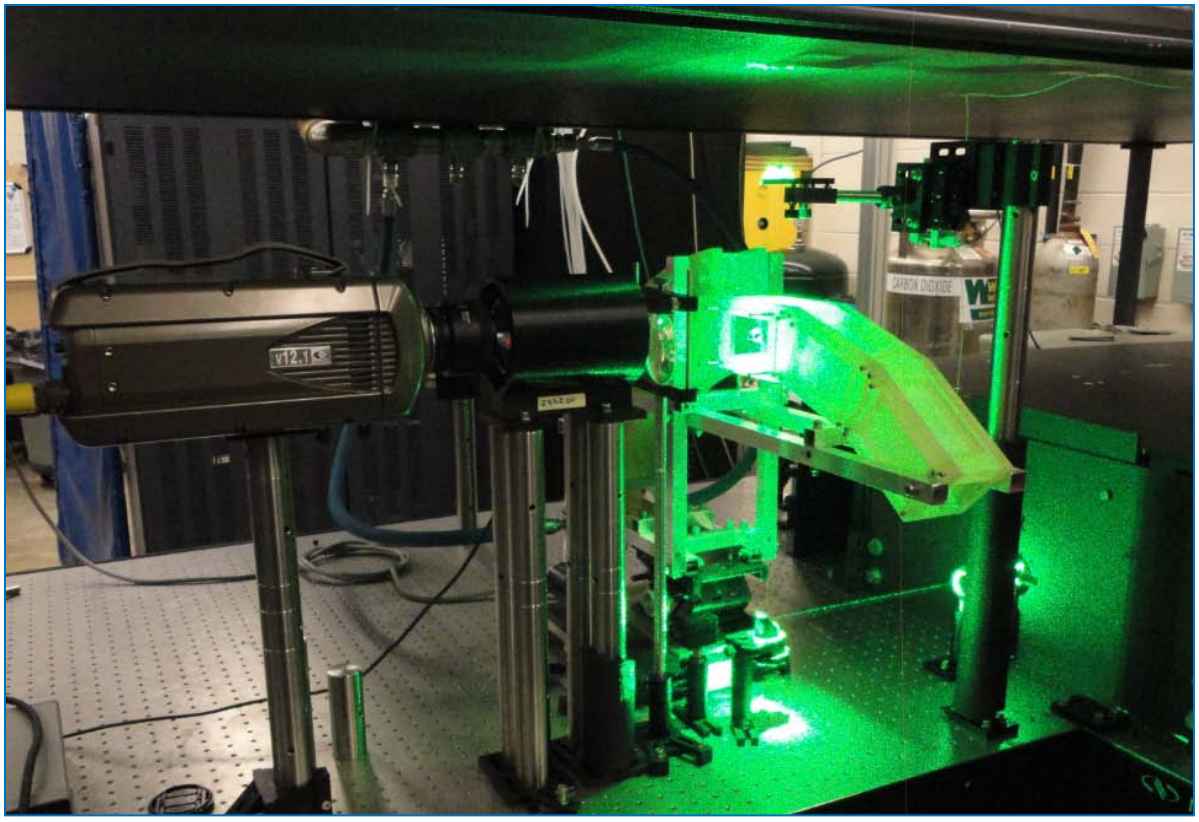

Figure 39. G-loaded Buoyant Jet Set Up Photo

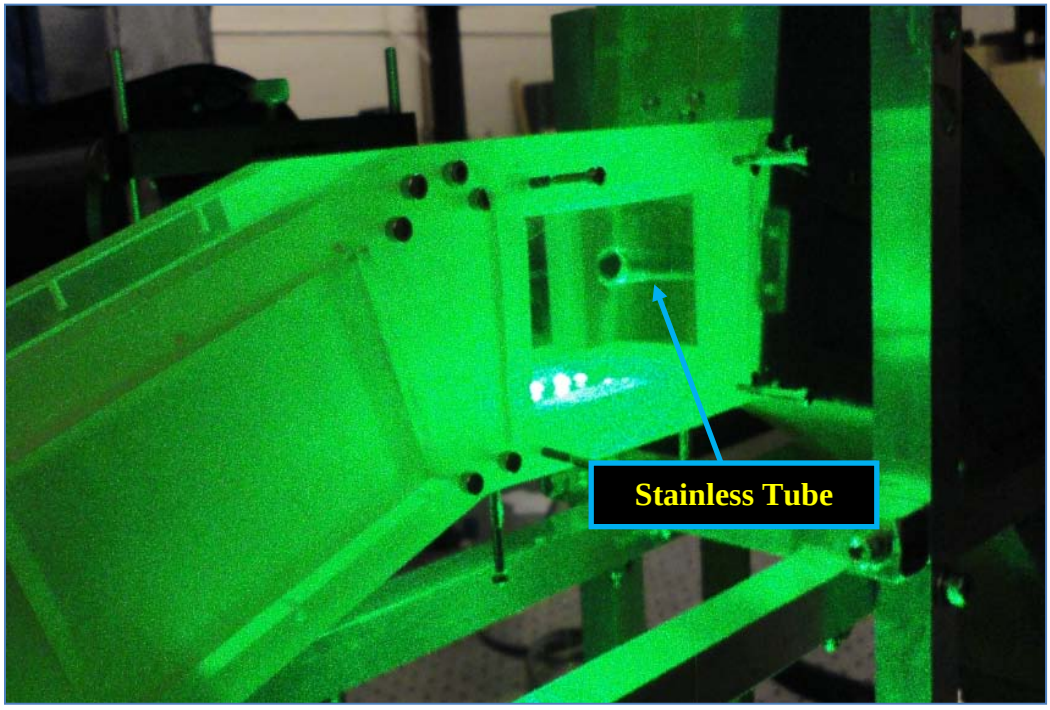

Figure 40. Stainless Tube Used to Feed in the CO_2

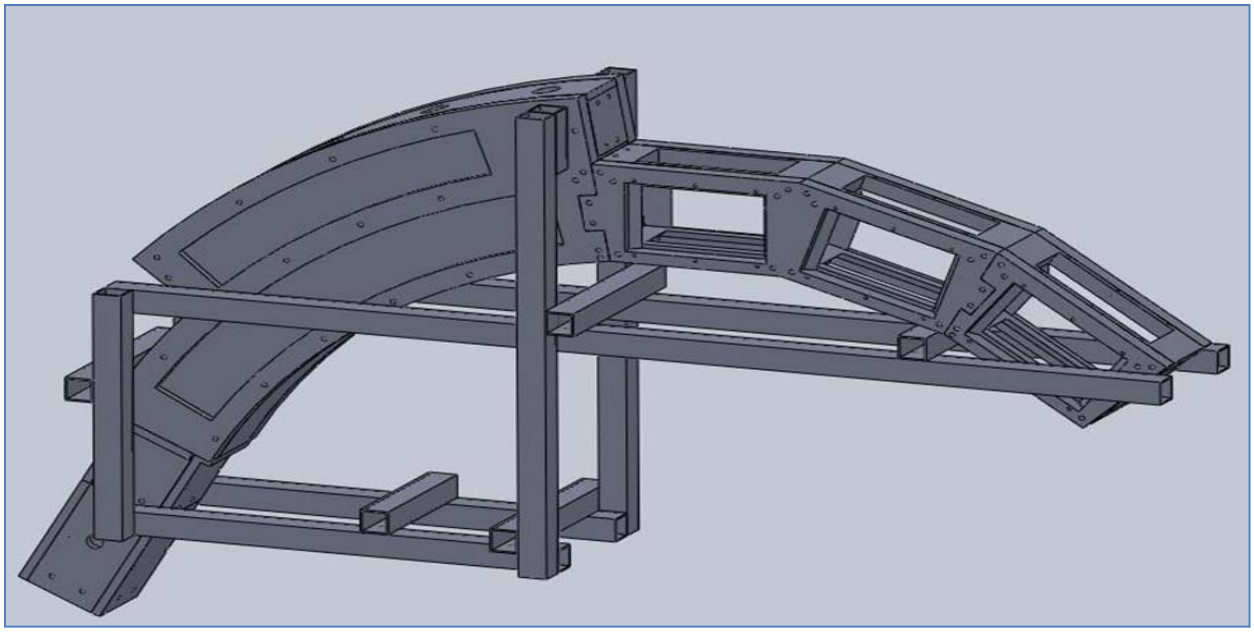

Figure 41. Curved Section CAD Drawing

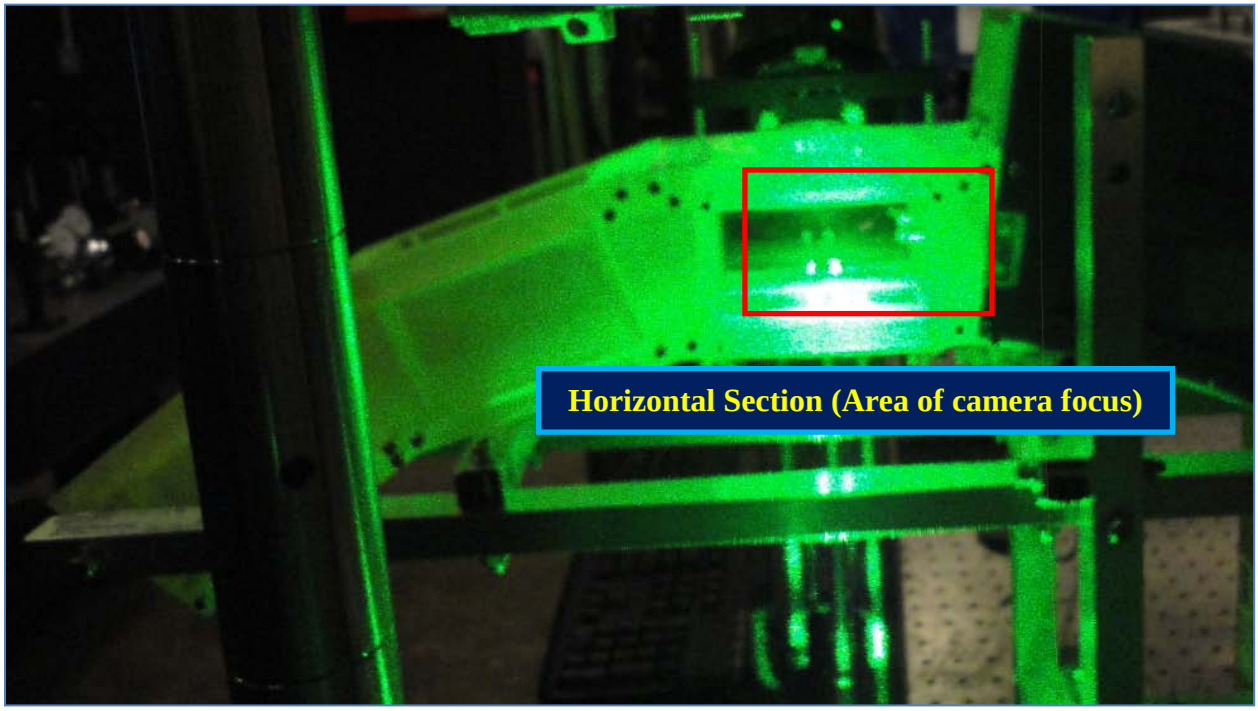

Figure 42. G-loaded Buoyant jet Horizontal Area of Focus

This experiment was set up in a way such that the area of interest at which the camera was focused was a horizontal section as shown in Figure 42. In order to allow the laser beams to pass through the sides of the horizontal section and intersect with the jet and the co-flowing air, four

different pieces of Quartz were used to seal the sides of the test section (the area of interest). The laser was directed to the area of interest using the same optics used in the second experiment. Imaging occurred along two vertical laser beams allowing the collection of intensity (or concentration) data at two different stream-wise locations for each run. The curved section was fixed on top of the traverse platform allowing the entire unit to move horizontally. This enabled data collection at different stream-wise locations. The co-flow was delivered from the same air tank used in the horizontal jet experiment. Before entering the curved section, air was collected at a rectangular shaped chamber (shown in Figure 43). Through this chamber the stainless tube was passed. The tube brought the jet of CO_2 from the tank through the Brooks mass flow controllers and to the measuring station. As mentioned earlier, the Brooks 5850i mass flow controller was used for low velocity (and G-loading) measurements while the Brooks 5853i mass flow controller was used for the high G-loading data collection.

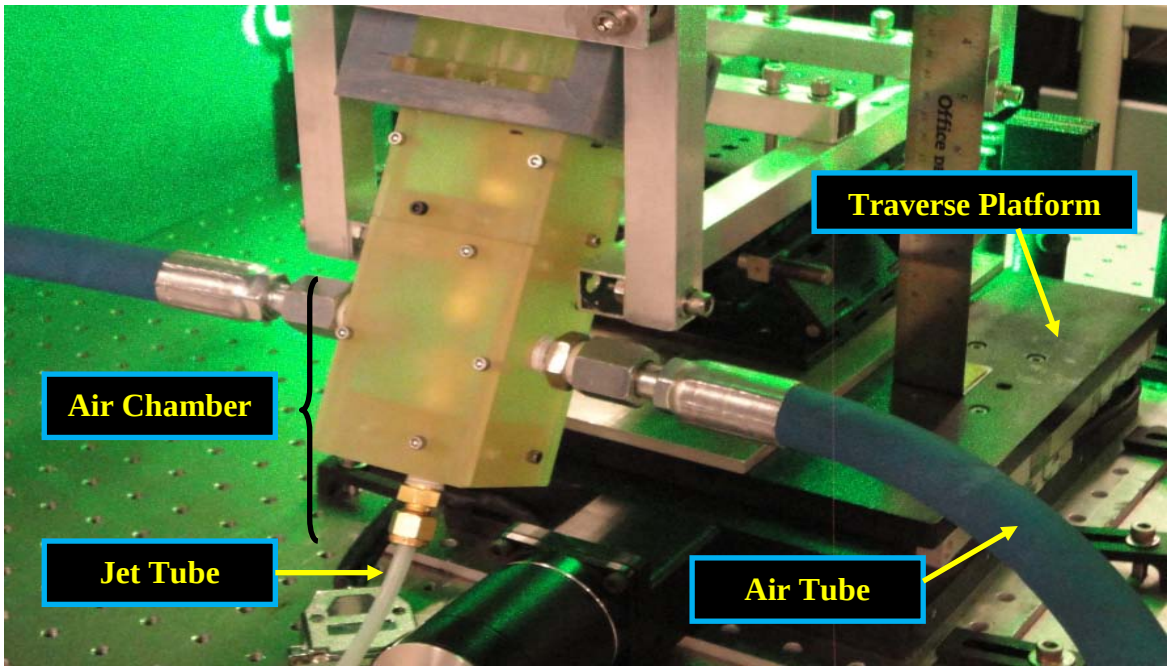

Figure 43. G-loaded Buoyant jet: Air Collection Chamber

III.5. Buoyant Jet Experimentation Methodology

In order to ensure the collection of Rayleigh scattering images of which useful information can be drawn, three main considerations were taken into account. These considerations involved the proper choice of the frame rate, the investigation of the Doppler Effect, and the development of formulas allowing the conversion of the Rayleigh scattering signal intensity to percent concentrations. Details of these considerations are as follows:

III.5.1. Data Acquisition Considerations

Given the jet's velocity and diameter values considered for the case of the CO_2 jet, initial jet's shedding frequency calculations were predicted to have values up to 25 Hz. Considering the rule of thumb that an adequate sampling rate is about ten times the maximum frequency of the signal, a frame rate of 250 Hz seems to be a minimum value to consider. When using a pulsed laser, the data acquisition rate is usually limited by the pulse rate. Fortunately, this is not the case when using a continuous wave laser such as in this study. The sampling rate, in this case, is only limited by the ability of the camera/lens unit to gather enough scattering light resulting in a sufficiently large signal to noise ratio.

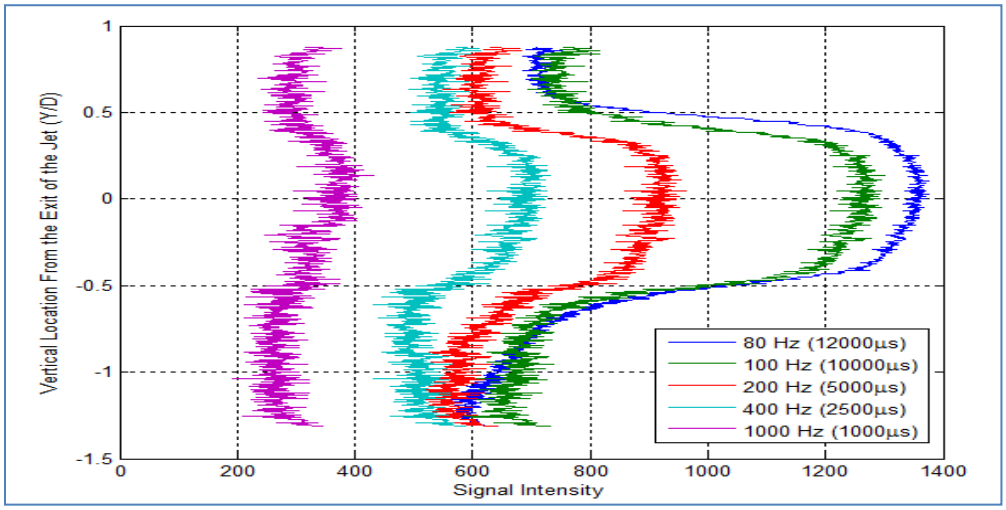

Figure 44. Frame Rate Sensitivity Analysis for the CO_2 Jet Configuration

Inherently, the higher the frame rate, the smaller the exposure time is, and hence the smaller the signal to noise ratio. Keeping this compromise in mind, it is therefore important to perform a frame rate (or exposure time) sensitivity analysis to figure out the highest possible frame rate value that would allow for an adequate signal to noise ratio. As shown in Figure 44, a frame rate of a 1000 Hz results in a poor signal to noise ratio (N/S of 70%). At 400 Hz however, it is easy to discern the Rayleigh scattering signal due to CO_2 from the one due to air (N/S of 21%). The signal intensity shown in Figure 44 is the sum of raw intensity values of five adjacent pixels. The signal due to CO_2 molecules is higher than the one due to air molecules since the CO_2 molecule has larger Rayleigh scattering cross section than the air molecule as it will be discussed in the data processing section of this thesis. Due to the fact that sampling rate and exposure time are inversely proportional, the signal is much higher for frame rates lower than 400 Hz (N/S of 7 % at 80 Hz for instance). However, due to the shedding frequency consideration discussed earlier, a frame rate of 400 Hz is chosen for the case of the CO_2 jet.

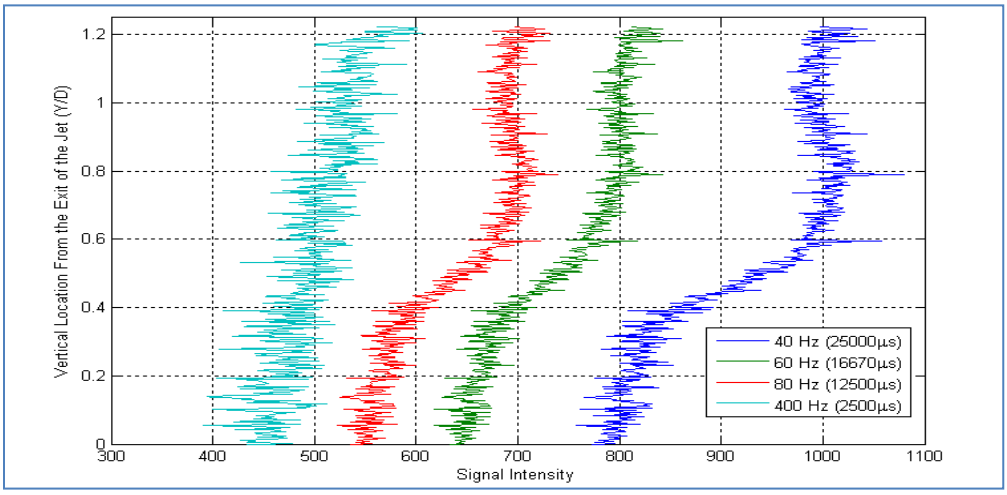

Figure 45. Frame Rate Sensitivity Analysis for the Helium Jet Configuration

Similar analysis is performed to choose a data acquisition rate for the case of the helium jet. There was no shedding frequency consideration in this case, since time resolved analysis

was only considered for the case of the CO_2 jet due to time limitation. A data acquisition rate of 80 Hz (with a N/S of 25 %) was considered for the case of the helium jet as it allows for the balance between a relatively high frame rate and an adequate signal to noise ratio as shown in Figure 45. The noise to signal ratio (N/S) for both CO_2 and helium measurement appears to be high (about 25 %). However, this sensitivity analysis was based on raw intensity data. When the intensity is converted to concentration, as will be explained in the data processing section, the background signal is subtracted which eliminates a significant amount of noise. An uncertainty analysis is performed in the data processing section to quantify the estimated percent error of the collected data and analysis.

III.5.2. Doppler Effect Considerations

As mentioned in the literature review section, the Rayleigh scattering central frequency can be Doppler shifted due to the motion of the molecules present in the flow. This shift, if not taken into account, could drive the Rayleigh scattering signal out of the absorption well and hence give false readings relating to the intensity of the signal. This study involves collecting Rayleigh scattering signal of moving CO_2, helium, and air molecules. Therefore, the Doppler Effect on the measurements needs to be addressed. When associated with the Rayleigh scattering phenomenon, the Doppler Effect, due to the motion of the molecules, results in a frequency shift $\Delta\upsilon$ given by Equation (14):

$$\Delta v = \frac{1}{2\pi}\overrightarrow{V_{jet}}.\vec{K} \qquad (14)$$

As shown in the equation, the frequency shift is the dot product of the jet velocity vector and the interaction wave vector. As shown in Figure 46, the frequency shift is associated with the secondary velocity in the direction of the interaction wave vector [7]. For the case of the

experiments performed in this study, however, the frequency shift due to the stream-wise direction is negligible since the jet velocity vector and interaction wave vector are perpendicular. Therefore, the measured Rayleigh scattering signal is primarily associated with concentration of the gas species.

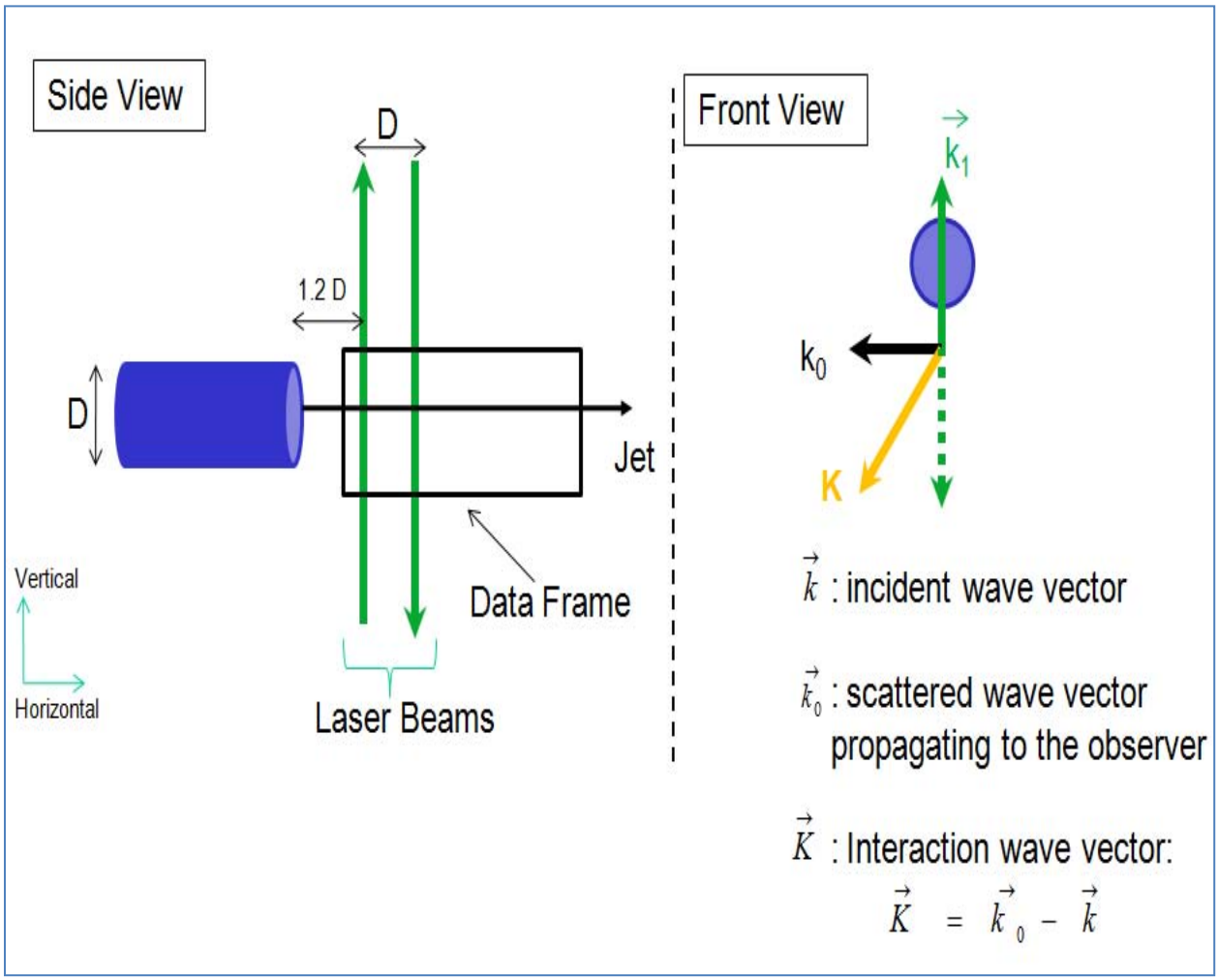

Figure 46. Sensitivity of the Rayleigh Scattering Signal to the Doppler Effect.

III.5.3. Data Processing

The data collection consisted of taking sets of 3000 images of the region of intersection between the jet and the two laser beams at 400 Hz for the CO_2 jet and 80 Hz for the helium jet. As discussed earlier, these frame rates were thought to result in the best signal to noise ratio while maintaining a relatively high sampling rate. The incident light power was kept at 12 W

during data collection. The camera was focused at the region of interest (intersection of the two beams with the horizontal or curved jet). The image resolution was set at 1280x800 pixels for all data measurements covering an area of interest of 59.5x37.5 mm as shown in Figure 47 below. Some distortion can be seen on the edges of the frame in Figure 47 due to the use of the spherical lens. However, the level of distortion in the area where the laser beams were was very small and hence no correction was made during data processing. The bright regions of Figure 47 correspond to an intensity of 130 counts while the dark regions correspond to about 35 counts.

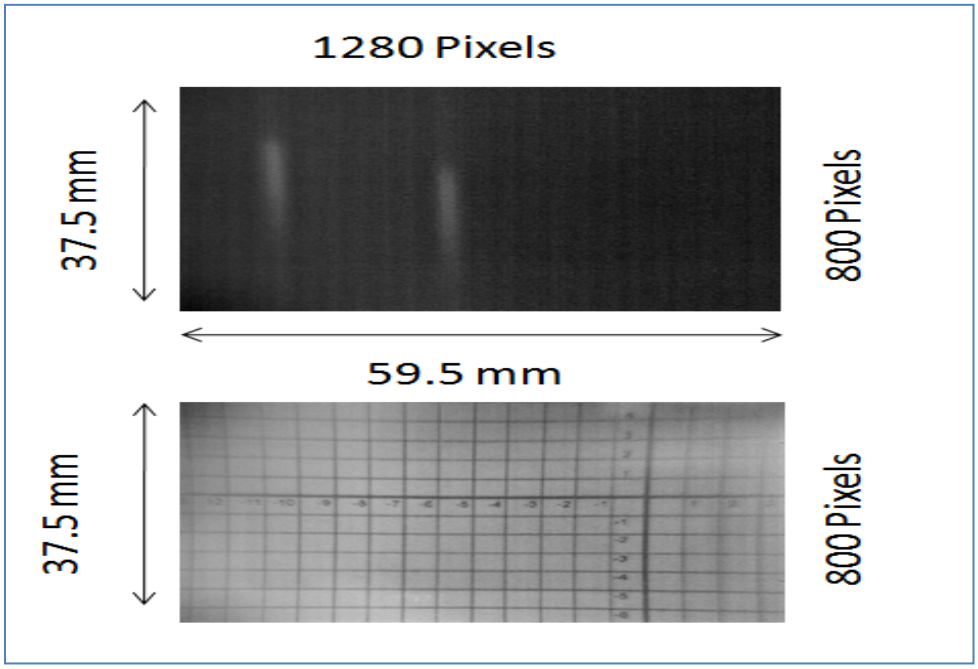

Figure 47. Unprocessed Image of Scattered Light of the Laser Going Through the CO_2 Jet and Air at 400 Hz (Top) and the Grid Used for Spatial Reference (Bottom).

For both the CO_2 and helium configurations, essentially three different types of images were collected to extract concentration information from the Rayleigh scattering signal. These sets of data of which samples are shown in Figure 48 were the signal due to jet and air molecules, signal due to air only, and background signal corresponding to collected images with the laser turned off (or with the lens cap on).

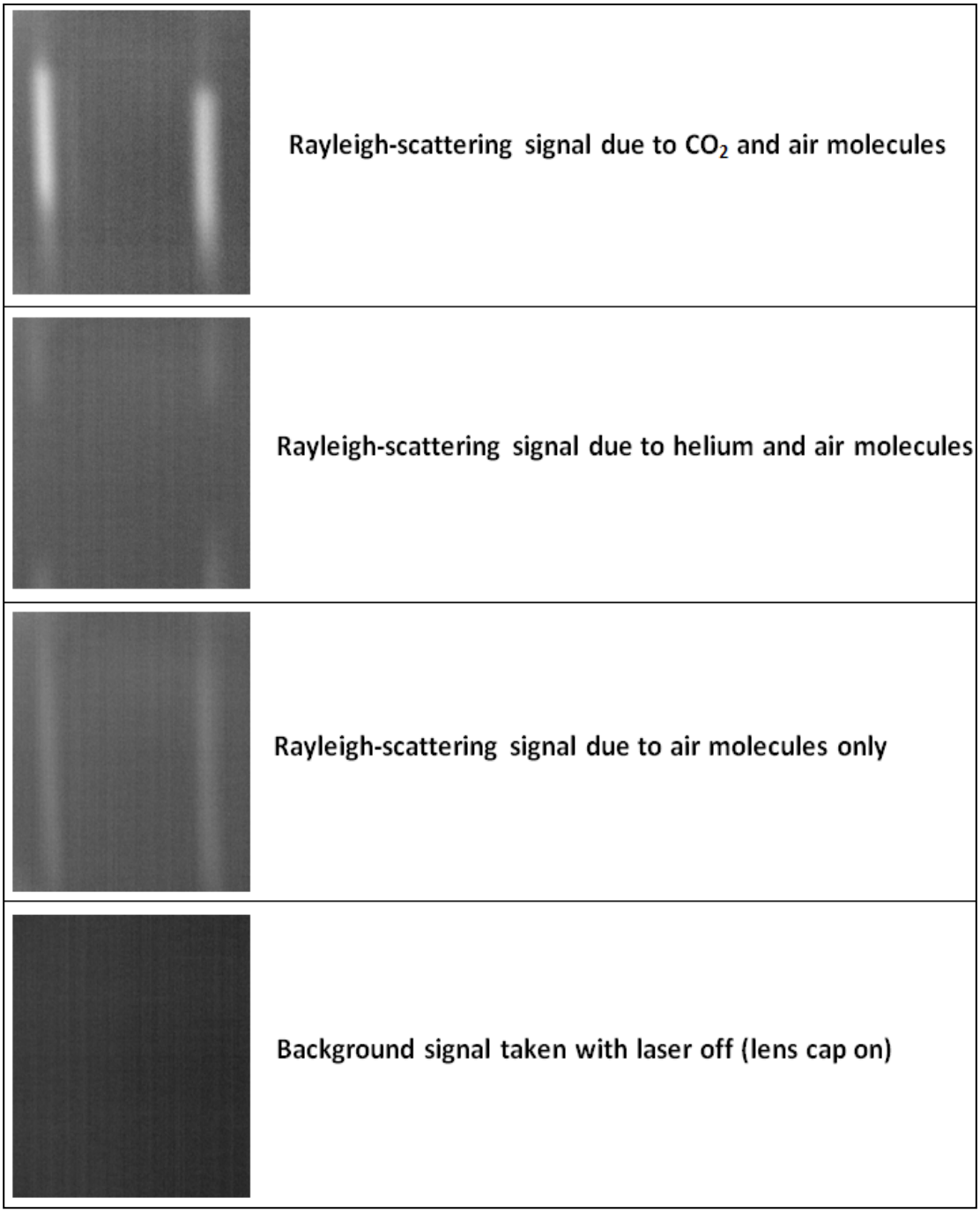

Figure 48. Sample Images of Signals Used for Data Processing of Both the CO2 and Helium Configurations

For the purpose of the data processing, only the areas of intersection of the laser beams with the jet were considered. Therefore, each frame was reduced to two matrices of dimensions 13x800 pixels. The width of 13 pixels corresponds to approximately 0.60 mm. The 16 bit

videos of the scattered light were initially converted to "*Multipage. TIFF*" format and then to "*.mat*" using MATLAB. The raw intensity for any frame at any given imaging location was a summation of the intensity due to Rayleigh scattering *I*, and the intensity of any captured background light I_o. This latter term included reflections off test equipment such as the stainless tubes used for this experiment or any lights in the laboratory. The background intensity was corrected for and subtracted from the raw intensity. In addition, the electronic signal generated by the camera was subtracted off from the scattered light signal. The electronic signal was obtained by capturing images with the lens cap on.

The outcome of the initial post processing described above is the intensity I_R which is the scattered light from both CO_2 (and helium) and air molecules combined with background signal subtracted. In order to convert the intensity I_R to concentration of the jet only, the intensity I_A of air only was removed from the signal. I_A was obtained by capturing images of the scattered light of the ambient air only and subtraction of the electronic signal of the camera. The formula used in this work to convert the intensity I_R to CO_2 concentration is given by:

$$\%CO_2 = \frac{I_R - I_A}{fI_A - I_A} \tag{15}$$

where *f* is a correction factor that takes into account the ratio in cross section between air and CO_2 molecules. Typically, the Rayleigh scattering signal of the CO_2 transmitted through the filter is about twice the signal associated with air molecules. The ratio of the CO_2 cross section to the N_2 cross section is about 2.23 while it is approximately 2.7 with respect to O_2 [25] which yields the following relationship:

$$2.23 \leq f = \frac{\sigma CO2}{\sigma Air} \leq 2.7 \tag{16}$$

For this study; the correction factor *f* turns out to be about 2.45 to ensure 100% CO_2 concentration at the core of the jet. I_A is set to 28 intensity counts (and approximately 22 for the case of the curved jet due to imaging through quartz) which correspond to the maximum value of air intensity. Considering this peak intensity values into the equation allows for the use of a more conservative calculation of the CO_2 (or helium) jet concentration.

On the other hand, the formula used to convert the Rayleigh scattering signal intensity to helium concentration is given by:

$$\%He = \frac{1-\frac{I_R}{I_A}}{1-\frac{\sigma He}{\sigma Air}} \tag{17}$$

The Rayleigh scattering cross section ratio used in the formula above is 1.4 % as given by Su *et al.* in their quantitative planar imaging of buoyant jet study [26].

Figure 49 and Figure 50 illustrate sample processed data for respectively the CO2 and helium jets' cases. For the case of CO_2, brighter regions correspond to the Rayleigh scattering signal due to CO_2 molecules (Figure 49) while signal due to helium molecules is associated with areas of dimmer intensity (Figure 50). The concentration plots were created by averaging the intensity values of all 3000 images for each pixel. The intensities were then converted to concentrations using Equations (16) and (17) described above.

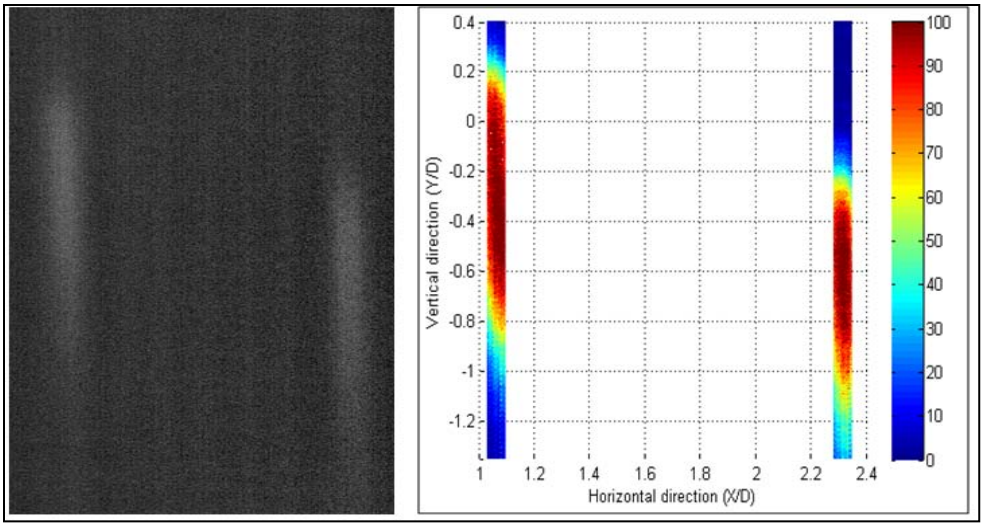

Figure 49. Raw Rayleigh Scattering Image (Left) and Processed Concentration Plot (Right) for the CO2 Configuration

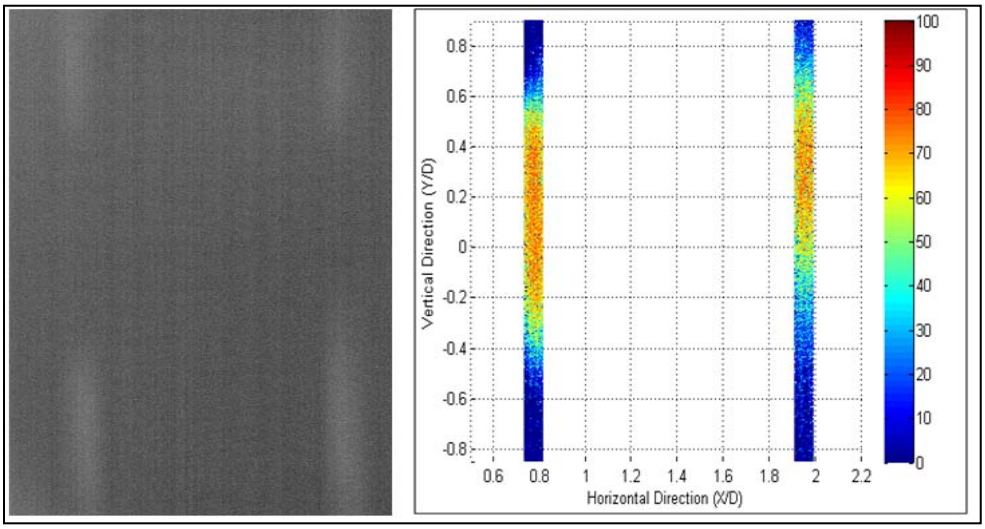

Figure 50. Raw Rayleigh Scattering Image (Left) and Processed Concentration Plot (Right) for the Helium Configuration

In addition to concentration plots, concentration profiles were obtained by averaging the concentration lines along the X/D (stream-wise) direction in a way to obtain a strip of concentration running across the entire vertical direction as shown in Figure 51b. As part of the analysis of the jet behavior, trajectory plots were also generated by tracking the maximum value of the jet's concentration along each strip located at every X/D location as shown in Figure 51c.

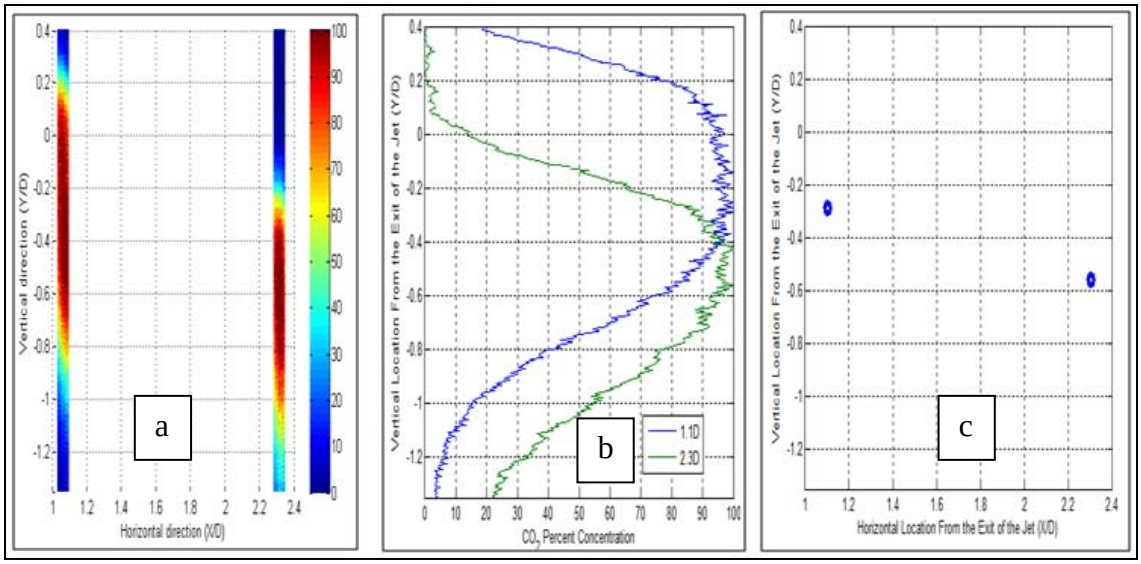

Figure 51. Sample CO_2 Process Data: (a) Percent Concentration, (b) Concentration Profile, (c) Jet's Trajectory

In order to monitor the variation of the Rayleigh scattering intensity over time, standard deviation of the signal's raw intensity were generated using the *std* command of MATLAB. These plots will be discussed in details in the Results and Analysis section of this report.

In order to ensure the extraction of relevant and trust worthy information from the collected data and analysis, it is important to approximate the overall percent error. There is obviously instrumentation errors as specified when describing the equipment used for this research. The equipment associated with the instrumentation errors include but are not limited to mass flow controllers, traverse unit, laser power instability, thermocouples regulating the iodine filter temperature, etc. All these errors could affect the end result which is the concentration of the jet. In fact, this concentration depends on various parameters such as the incident power, the laser's wavelength, the position of the beam with respect to the jet, and others. The problem is that, for this research, there is no direct equation that could relate all these parameters directly to the concentration of the jet. Classical formulas of uncertainty cannot therefore be used in this case. However, a repeatability analysis could be used to investigate the consistency of the information

given by the collected signal. For that purpose, one case corresponding to a given flow condition was run twice at two different times and results were compared. The standard deviation between the jet concentrations of the two runs, when normalized by the mean, is considered to be an approximation of the overall error of this analysis. Between the two presumably identical runs, other cases were ran to allow for the manifestation of the inherent measuring errors such as the change in the laser power over time, the drifting of the wavelength which affects the transmitted light, the imperfection in the traverse unit setting and readout, etc. The case considered here was one of the cases of the third experiment involving the investigation of G-loaded buoyant jet. It was a case involving the presence of co-flowing air to take into account any errors due to the vibration of the jet's tube in the presence of co-flow. One stream-wise position was considered which was an X/D of 1.3. Figure 52 illustrates the concentration profiles corresponding to the 1.3 D position from the first and second run.

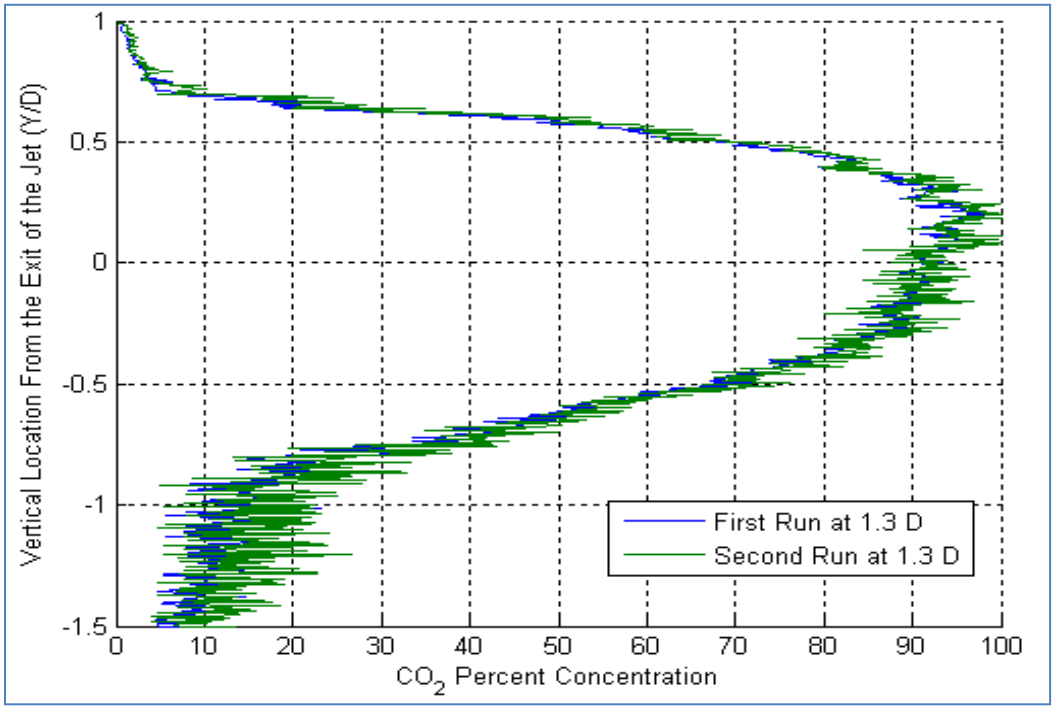

Figure 52. Jet's Concentration Profiles at 1.3 D

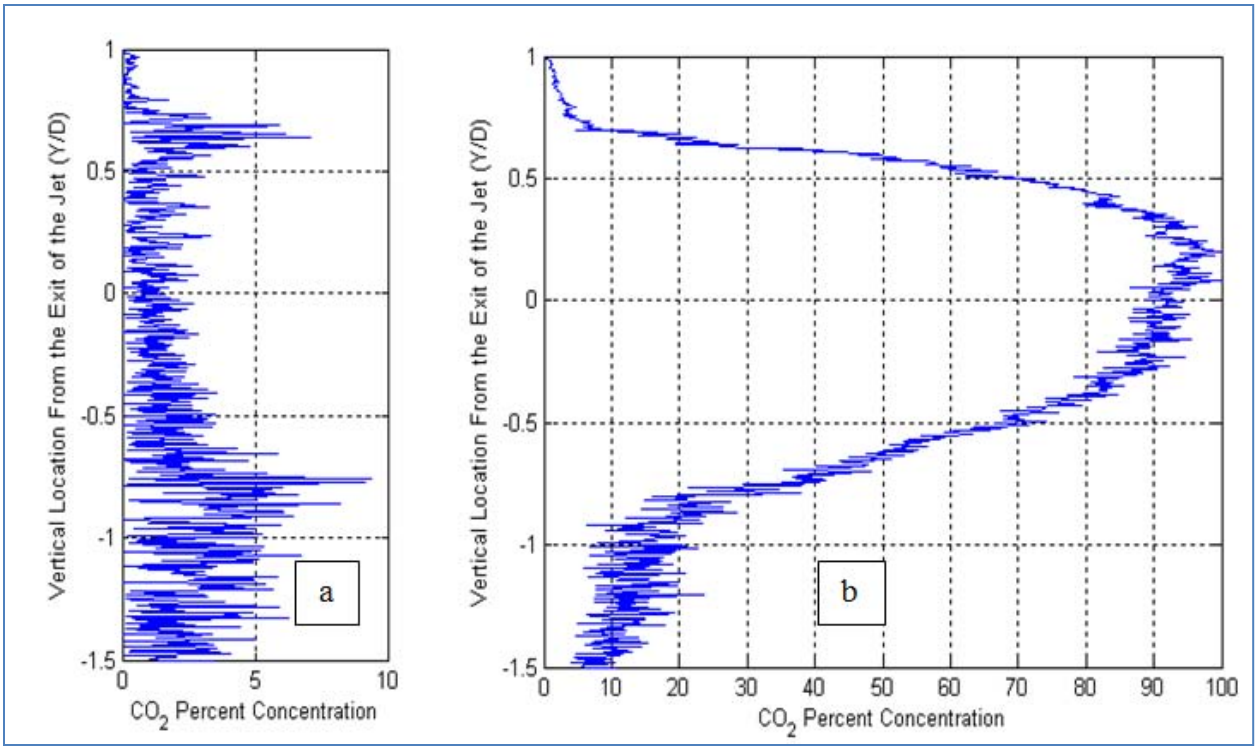

Figure 53. Position one (X/D=1.3): (a) Standard Deviation and (b) Mean

As shown in Figure 52, the two runs are very close to each other. It is however hard to quantify the difference between them. For that purpose, Figure 53 was generated to estimate the error between the two runs based on the standard deviation. At this position (X/D = 1.3), the standard deviation in the area of the core of the jet is approximately 3 % while the mean has a maximum value of 98%. This results in an error of approximately 3 % in the core of the jet which is the interest of this study mainly when tracking the trajectory of the jet. The error in the areas around the core of the jet is higher than at the core. In addition, the errors increase as the stream-wise location increases due to the weakening of the signal as a result of mixing and due to the slight difference power of the two laser beams off of which the Rayleigh scattering signal is collected.

Every time, a laser beam hits the surface of a mirror or a prism it loses a small percentage of its power. The second laser beam is created off of the first beam through the use of a prism.

In order to quantify the difference in power between the two laser lines, the Rayleigh scattering signal due to the presence of air only collected off of both laser beams was considered.

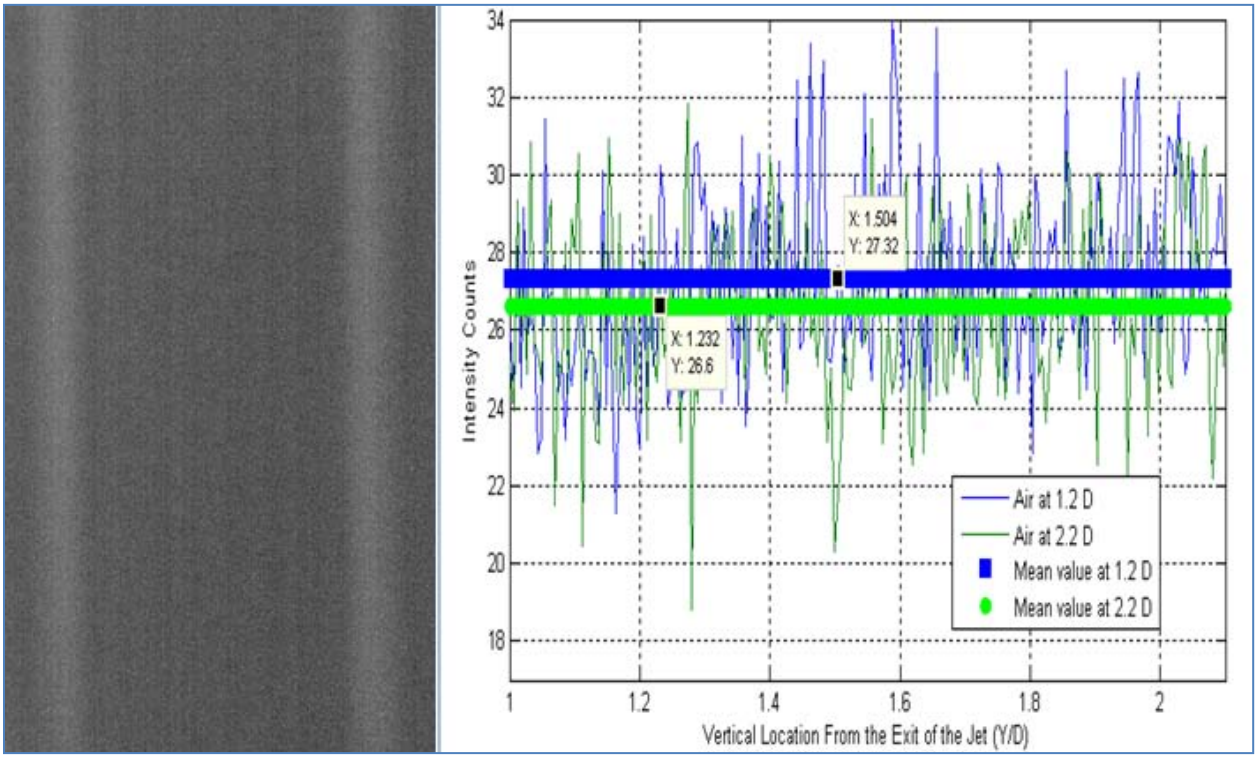

Figure 54. Rayleigh-Scattering Signal Due to Air Associated with the First and Second Laser Beams: (a) Raw Images and (b) Intensity Counts

A raw images of the two signals is shown in Figure 54a. Figure 54b illustrates the intensity counts of the two Rayleigh scattering signals due to air. Based on the ratio of the average intensity values of the two signals, the second line has approximately 97.5 % power of the first line. This difference was taken into account when generating the concentration data. When processing the data for this research the information corresponding to the first line was chosen in favor of the one (in most cases) associated with the second line every time there was an overlap between the two lines. The laser beam comparison leads to adding a 2.5 % possible error to the 4% error found above.

IV. Results and Analysis

IV.1. Experiment # 1 : Iodine Filter Characterization

The data obtained for iodine filter characterization is transferred to an EXCEL sheet and transformed into graphs to be laid out and discussed in this section. Multiple runs were performed in order to validate the consistency of both the filter's behavior and the data acquisition method. For the iodine cell temperature set at 90 ^{o}C and 40 ^{o}C, two tests were performed for each temperature. Figure 55 and Figure 56 below illustrate the findings of this step and show negligible variation of the results when comparing the two tests.

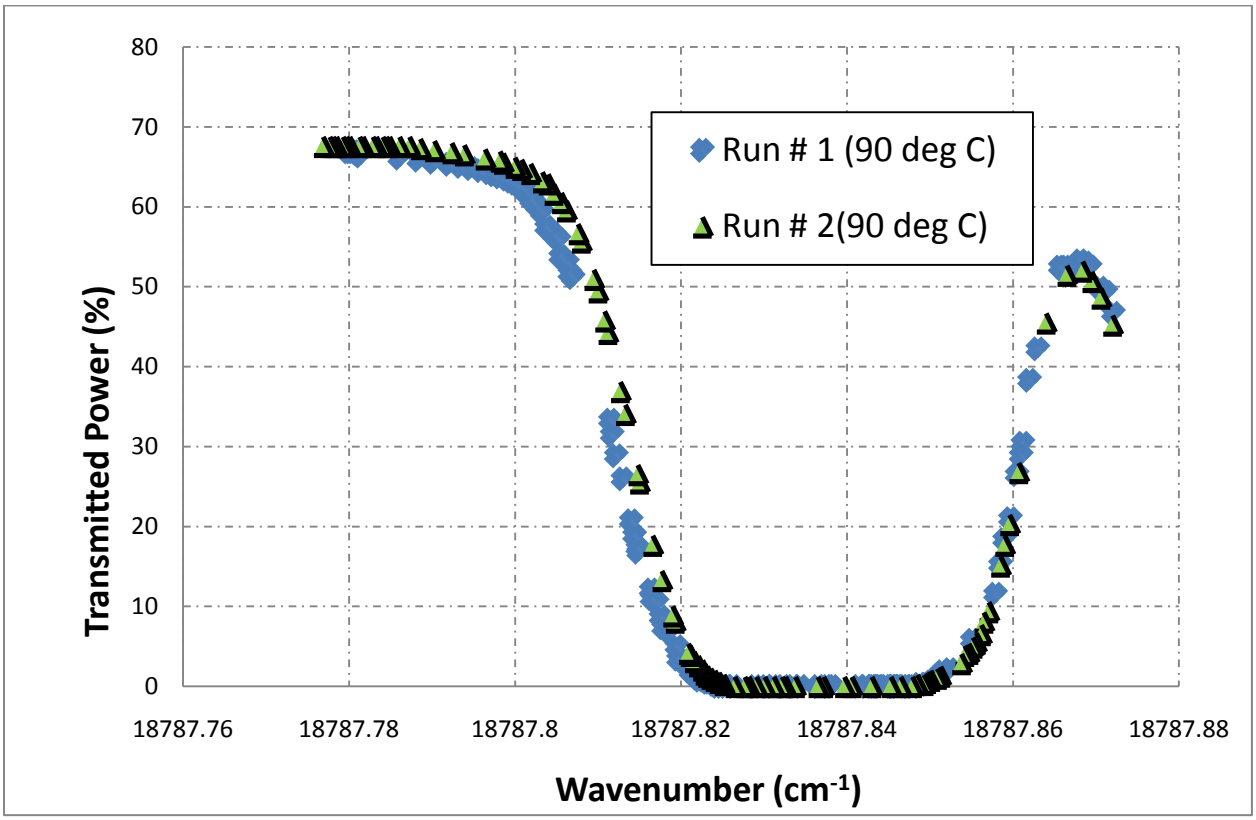

Figure 55. Repeatability Test of the Transmitted Power of the Filter at 90 ^{o}C

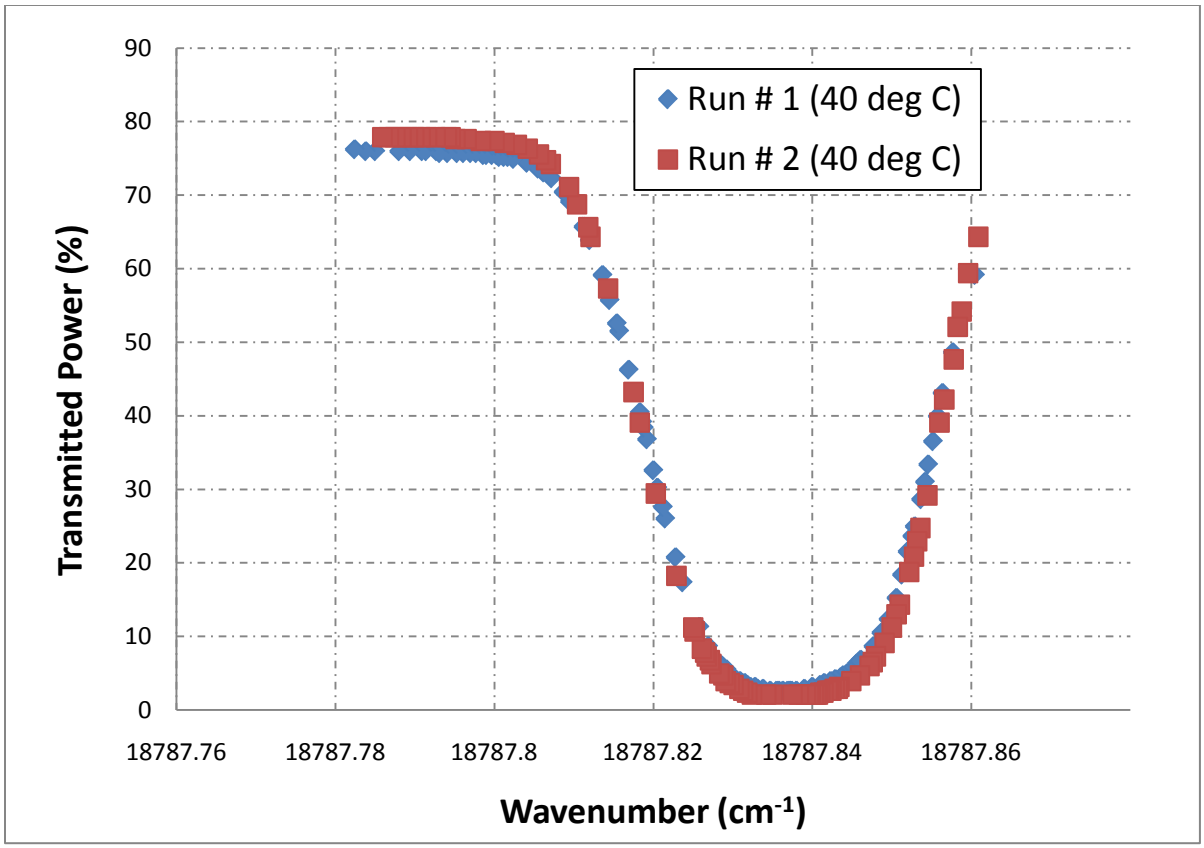

Figure 56. Repeatability Test of the Transmitted Power of the Filter at 40 ^{o} C

The optimal iodine cell temperature corresponds to the temperature at which the frequency range corresponding to transmission is the largest. Operating the cell temperature at the optimal temperature ensures maximum blocking of the unwanted background signal. Based on Figure 57 below, among the three tested temperatures, 90 ^{o} C appears to be the optimal temperature for the iodine molecular filter in use. In addition, the absorption well depth increases as the temperature increases. Therefore, for future uses of the iodine filter (the second and third experiment), the cell temperature will be set at 90 ^{o} C.

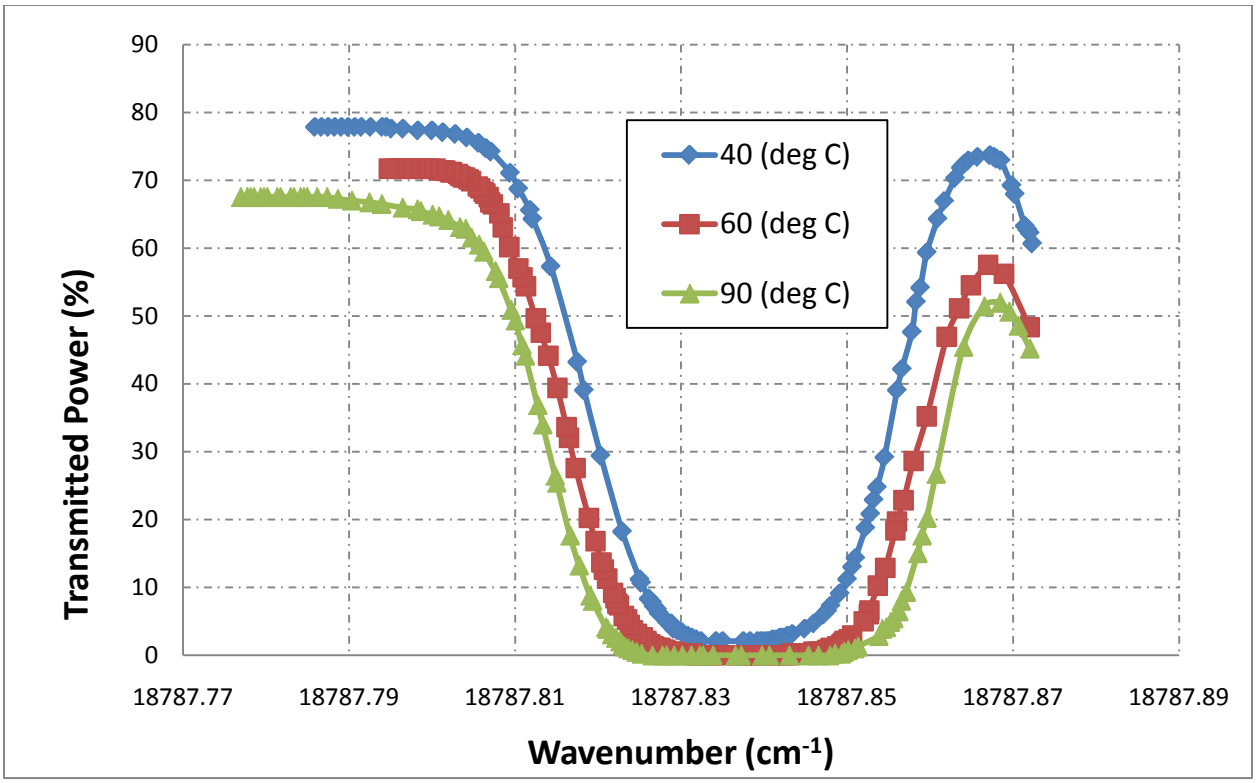

Figure 57. Iodine Filter Absorption Well for Three Different Cell Temperature

The details of the absorption well are given in Figure 58 below. The maximum absorption occurs between 18787.8265 cm^{-1} and 18787.8479 cm^{-1}. In order to optimize the scattered signal quality when using Rayleigh scattering for the remainder of this work, the laser wavelength (wave number) must be tuned to be in this range of values during the period of the test. A less restrictive range of 5% transmission is also depicted in Figure 58. When performing the Rayleigh scattering measurement, it is recommended to start with values of wave number greater than that of the upper portion of the well. Then let the wave number drift down to the range of zero transmission. At that point testing can began while monitoring the wave number (or wavelength) to ensure that the values stay within the appropriate range.

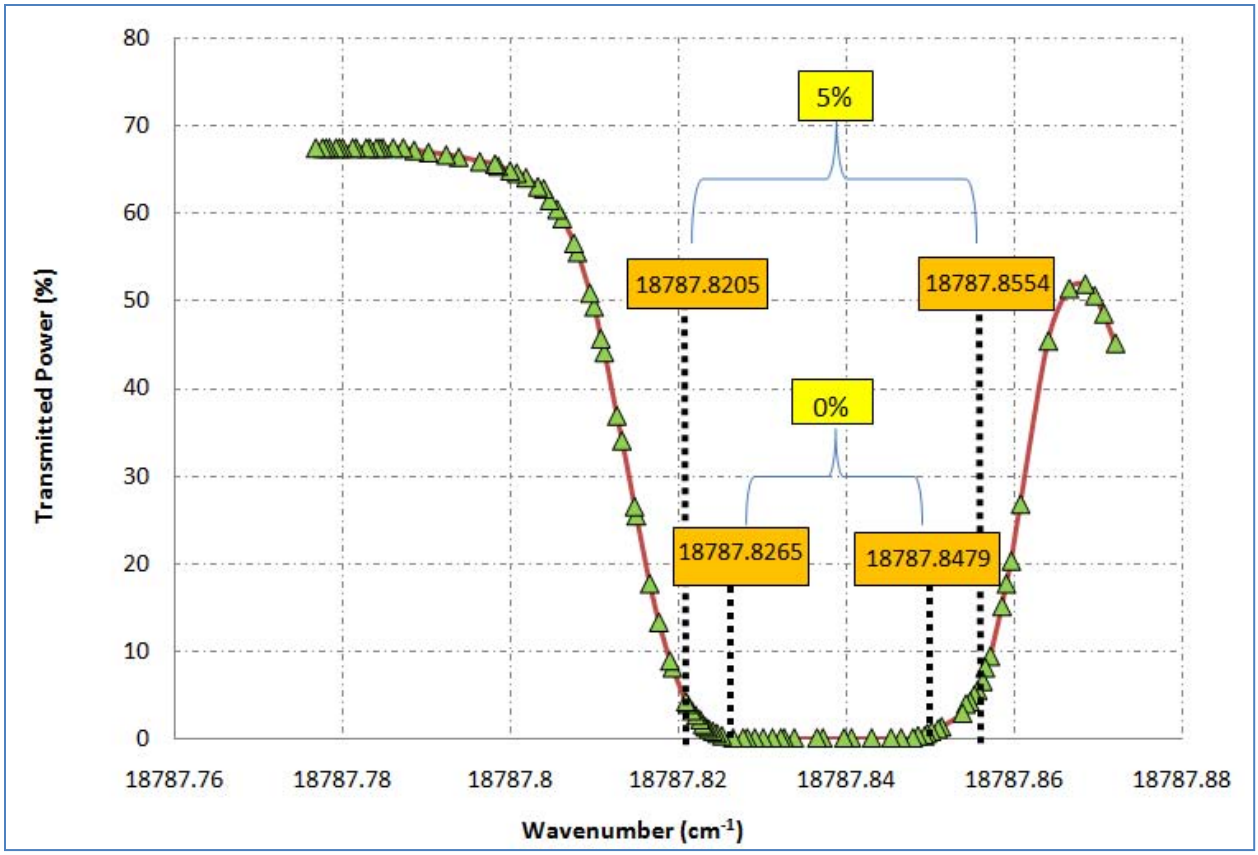

Figure 58. Iodine Filter Absorption Well at 90° C

Based on the literature, the absorption well can be expressed also as a function of the wavelength (in nm) or a relative frequency (in GHz). The relative frequency is calculated by taking the difference with respect to a reference frequency that corresponds to the center of the well. In order to be able to compare the results with previous filter's characterization in the literature, three more graphs Figure 59 , Figure 60 , and Figure 61 were also generated. The center of the well corresponds to a wavelength of 532.1099054 nm in air, a wavelength of 532.2580152 nm in vacuum, and a reference frequency of 563245.1895 GHz.

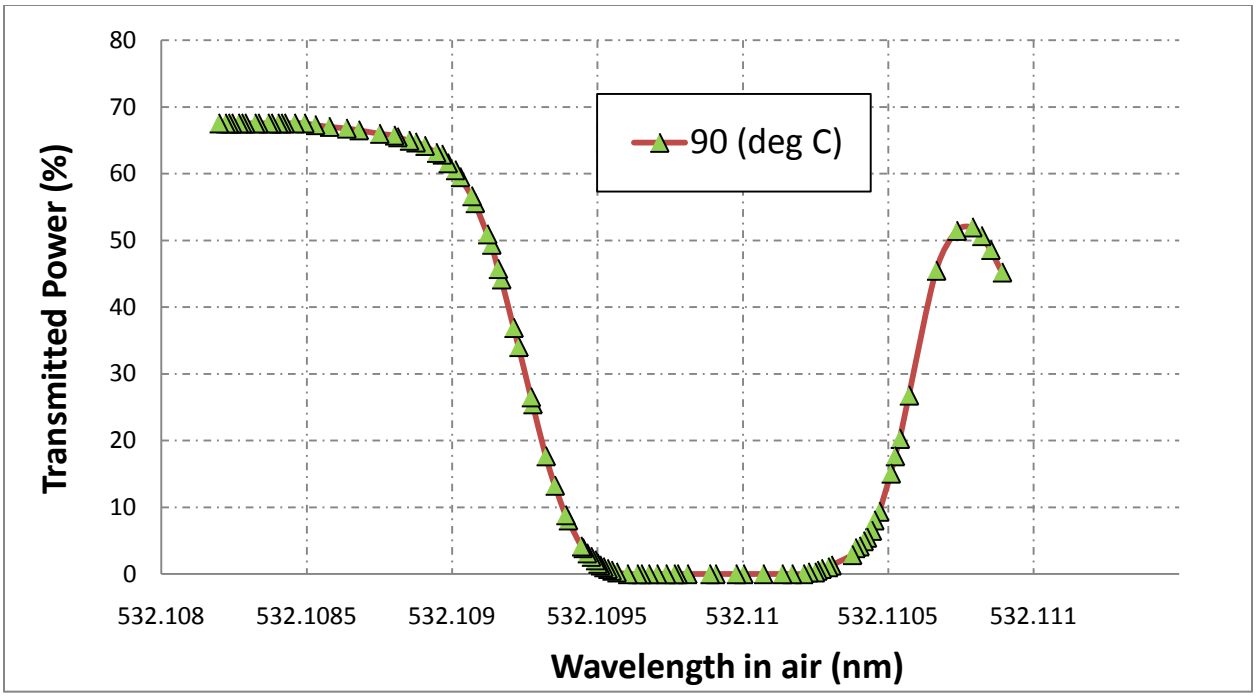

Figure 59. Iodine Filter Absorption Well with Respect to Wavelength in Air

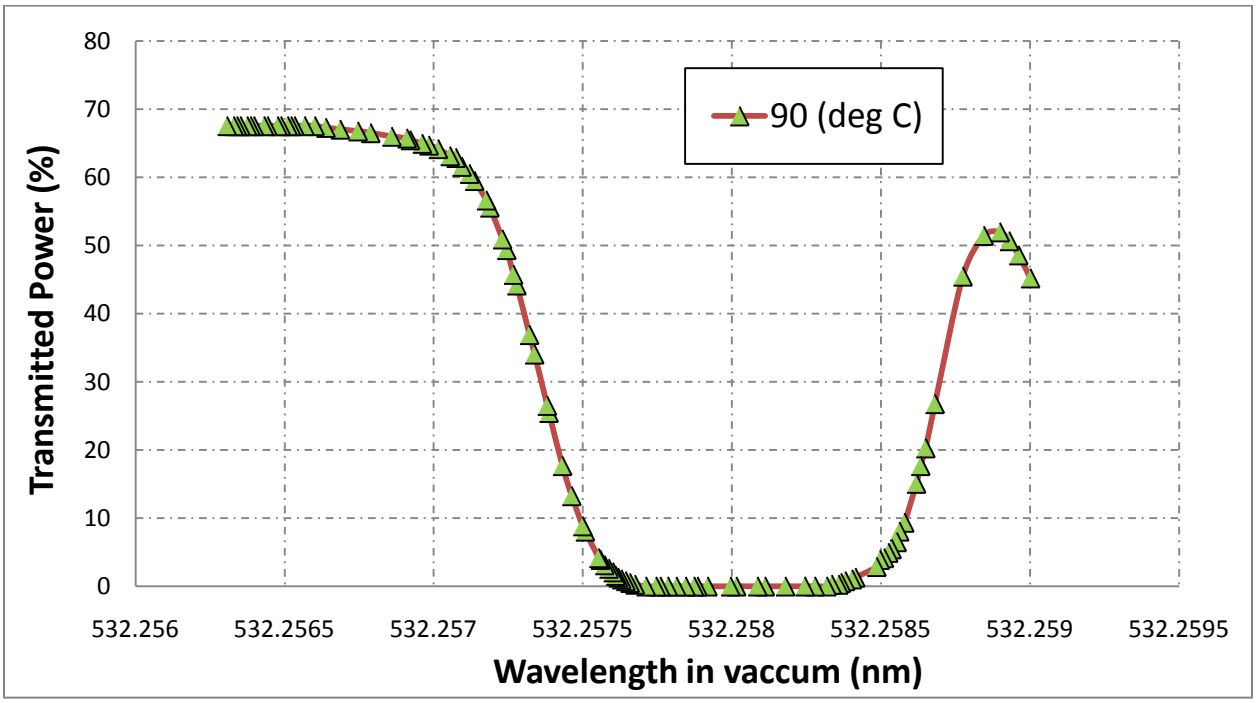

Figure 60. Iodine Filter Absorption Well with Respect to Wavelength in Vacuum

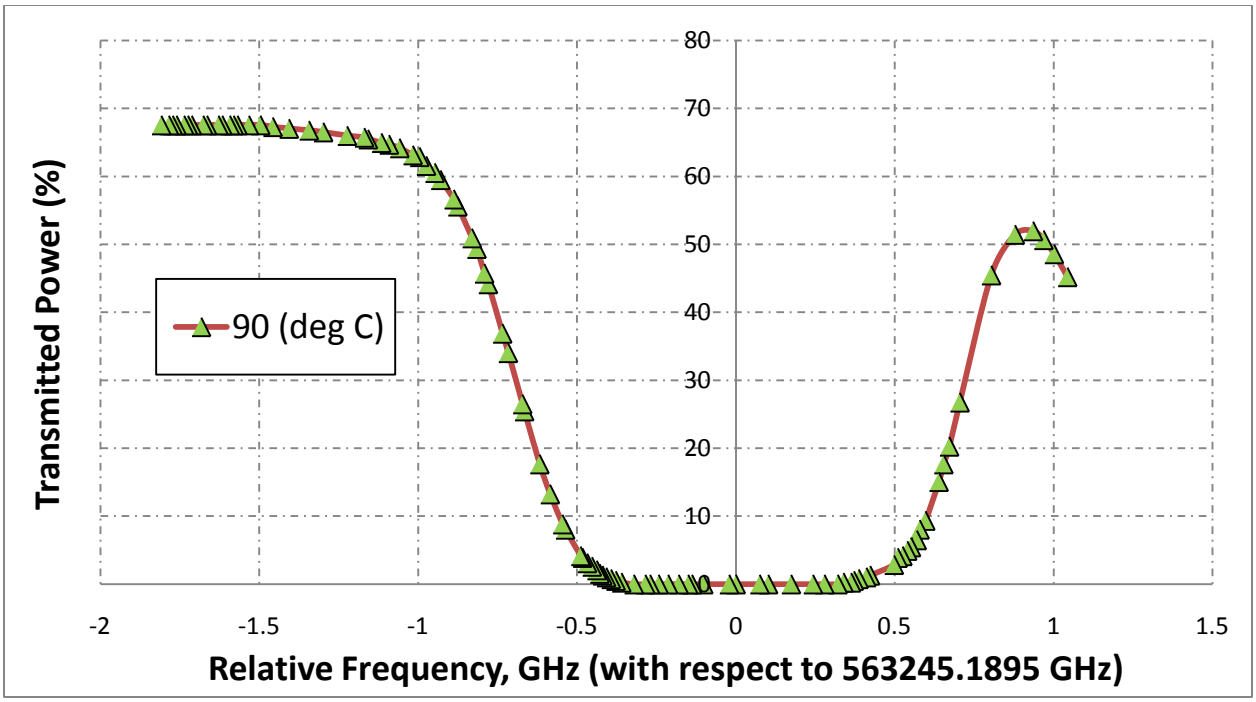

Figure 61. Iodine Filter Absorption Well with Respect to Relative Frequency

Although the well constructed in this section depicts the shape of a typical absorption well, it is not ideal for two reasons. First, it does not have steep and sharp edges which characterize a near ideal molecular filter. Second, we expected the filter to have 100% transmittance outside the well. It only reached 68% on the left edge and 52% on the right edge. In fact, it appeared to be entering a second well on the upper end of the well. In order to see the filter's behavior at the upper end of the first well, the transmitted power is calculated for wave number values greater than 18787.872 cm^{-1}. This resulted in Figure 62 below.

Results from the iodine filter's characterization (which will be discussed in the Results and Analysis chapter) were taken into consideration. The incident beam wavelength was monitored to ensure maximum blockage of background noise and unwanted signal when taken data. In addition, and by closely watching the image of the Rayleigh scattering signal collected by the camera, it was relatively easy to identify the times when the incident beam's wavelength was

within the range of the filter's absorption well. Figure 63 illustrates the difference between the transmitted Rayleigh scattering signal when inside and outside the filter's absorption well.

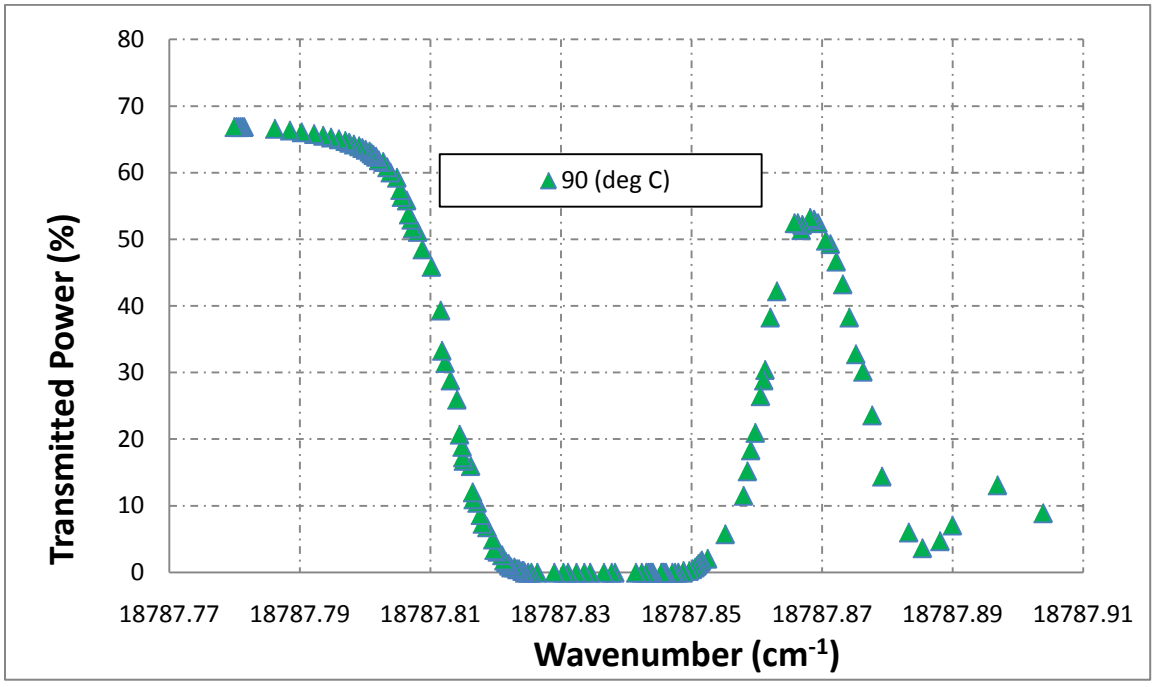

Figure 62. Investigation of the Upper End on the Absorption Well

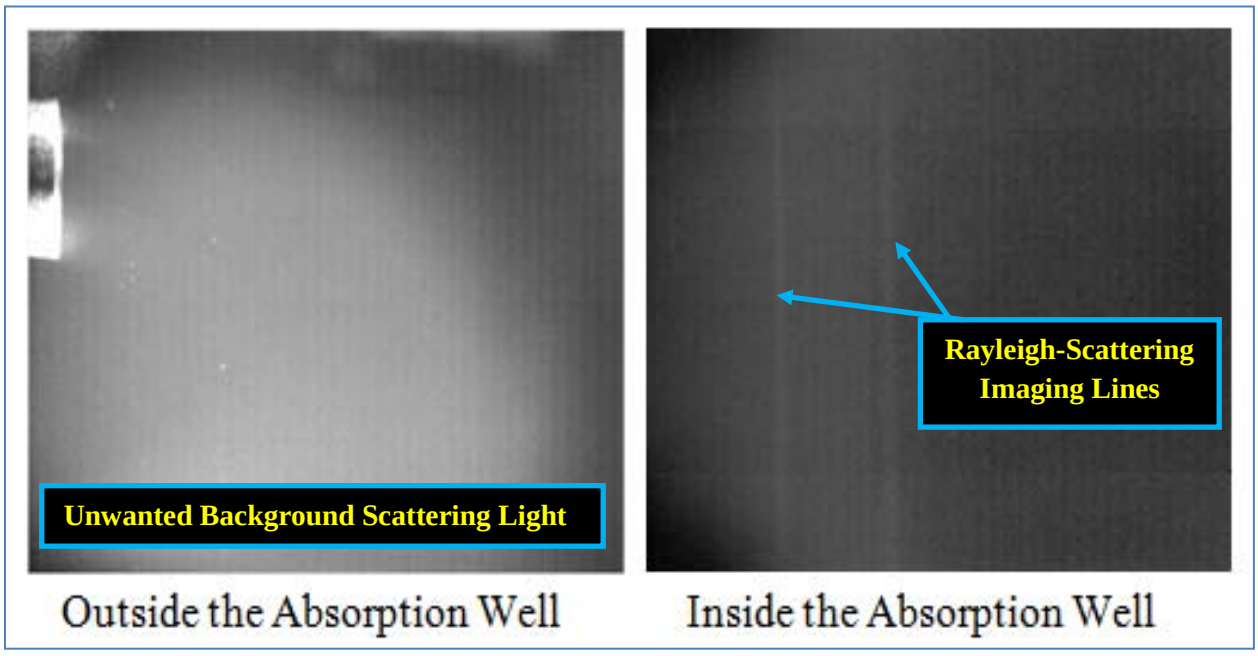

Figure 63. Rayleigh-Scattering Signal Inside and Outside the Filter's Absorption Well

IV.2. Experiment # 2: Horizontal Buoyant Jet in a Co-flow

This experiment sheds the light on the interaction between the co-flowing gas (air) and the jet (helium or CO_2) in the presence of buoyancy effects. The goal is to understand and characterize the effects of both buoyancy and the addition of the co-flow to the flow field on the trajectory and mixing properties of the jet. The use of both helium (a lighter than air jet) and CO_2 (heavier than air jet) allows for the comparison between the jet's behavior in the presence of positive and negative buoyancy effects.

IV.2.1. Cases With Helium Gas

Table 2. Processed Cases of Different Flow Conditions for the Helium Jet

Cases	D (mm)	V_{air} (m/s) (co-flow)	V_{He} (m/s)	$V_{ratio} = \frac{V_{He}}{V_{air}}$	$\Delta V = \lvert V_{He} - V_{air} \rvert$ (m/s)	Re_{jet}	Fr_{jet}
1	11.53	0	0.914	∞	0.914	89	1.1
2	11.53	0.914	0.914	1	0	89	1.1

Several cases of various flow parameters and conditions were examined for the case of CO_2 to allow for a time resolved concentration analysis and a jet's trajectory investigation. On the other hand, only two flow conditions were examined for the case of the helium jet due to the weakness of the Rayleigh scattering signal and the similarity in the jet's behavior between the helium and CO_2 cases. These two cases, which are described in Table 2, highlight the effects the addition of the co-flow to the flow field has on the jet trajectory and its mixing properties. The helium configuration data analysis will be presented first since it is much shorter. It will essentially consist of a comparison between Case 1 (without co-flow) and Case 2 (with co-flow).

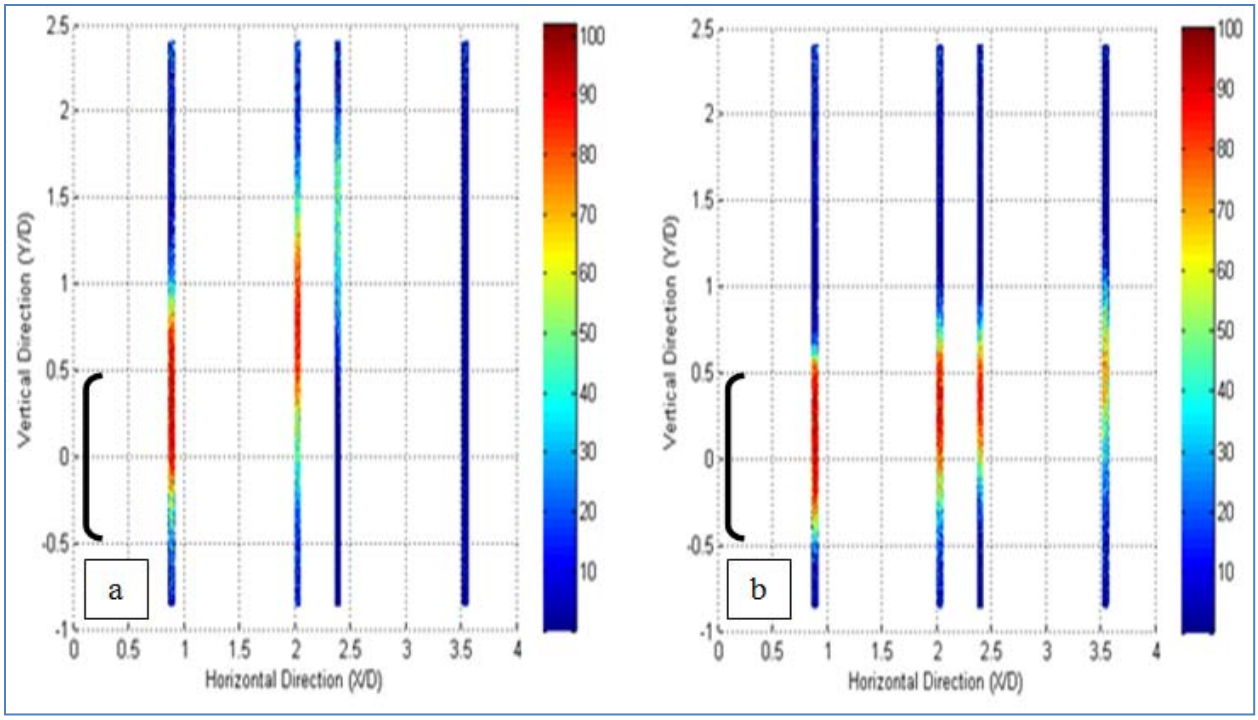

Figure 64. Helium Jet Concentration Plots: (a) Without Co-flow (Case 1), and (b) With Co-flow (Case 2)

Using the concentration formula of the helium (Equation 16), the Rayleigh scattering intensity values are converted to concentration plots shown in Figure 64a and Figure 64b. Concentration is obtained along two lines for each data measurement set. The four lines (or six lines for the case of the CO_2 configuration) shown on the figures for the remainder of this analysis are generated by joining data taken at different stream-wise (X/D) locations. As shown in Table 2, Case 1 corresponds to a jet velocity of 0.914 m/sec. Case 2 maintains the same conditions of Case 1 except for the addition of a co-flow of air going at the same velocity of the jet for comparison purpose. As shown in Figure 64, both jets follow an upward curvature due to positive buoyancy. This is expected since helium is much lighter than air and tends to naturally flow upward. However, it is obvious that the addition of the co-flowing air contributes to the straightening of the helium jet. In fact, due to the addition of the co-flow, the center of the jet goes from being at 1.25 Y/D for about a 2.4 X/D to roughly 0.5 Y/D. Y/D is the relative

normalized vertical location of the jet with respect to the center of exit of the tube while X/D is the normalized horizontal (stream-wise) location of the jet measured from the exit of the tube. As far as the mixing of the jet with air, it seems that the diffusion of the helium into air, at the same X/D location, is more significant in the absence of the co-flow. However, for both cases the mixing and the level of turbulence of the jet increases downstream of the jet as shown in Figure 65 of the standard deviation plots.

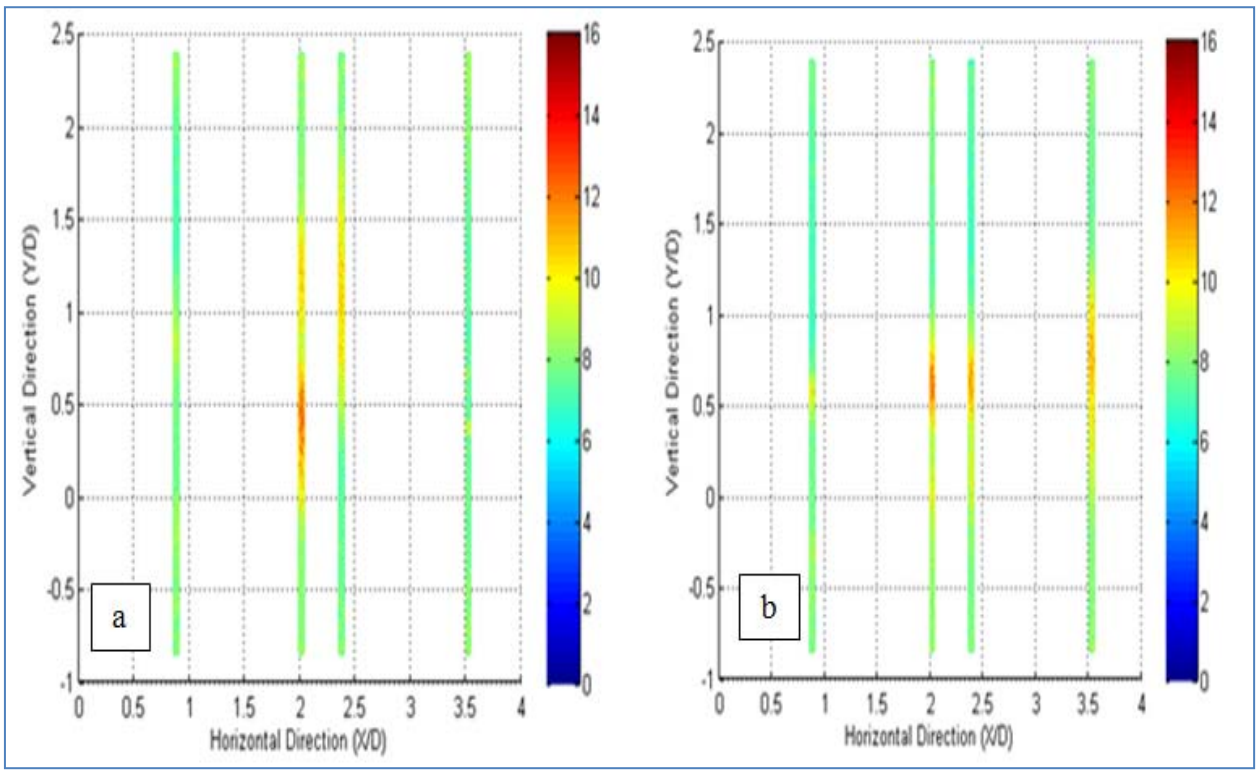

Figure 65. Standard Deviation of Helium Intensity: (a) Without Co-flow (Case 1) and (b) With Co-flow (Case 2)

For both cases (Figure 65a and Figure 65b), the mixing occurs initially in the top and bottom shear layers of the regions of interaction between the jet and the co-flowing air. As the jet moves downstream, it loses a lot of its momentum and the mixing moves progressively toward the center of the jet as shown in both Figure 65a and Figure 65b. It is important to note

as well that for Case 2 (with co-flow), the top shear layer is much more significant than the bottom shear layer due to the tendency of the jet to go up (positive buoyancy) which is expected.

The observations noted based on Figure 64 and Figure 65 can also be extracted by simply examining the concentration profile plots of Figure 66.

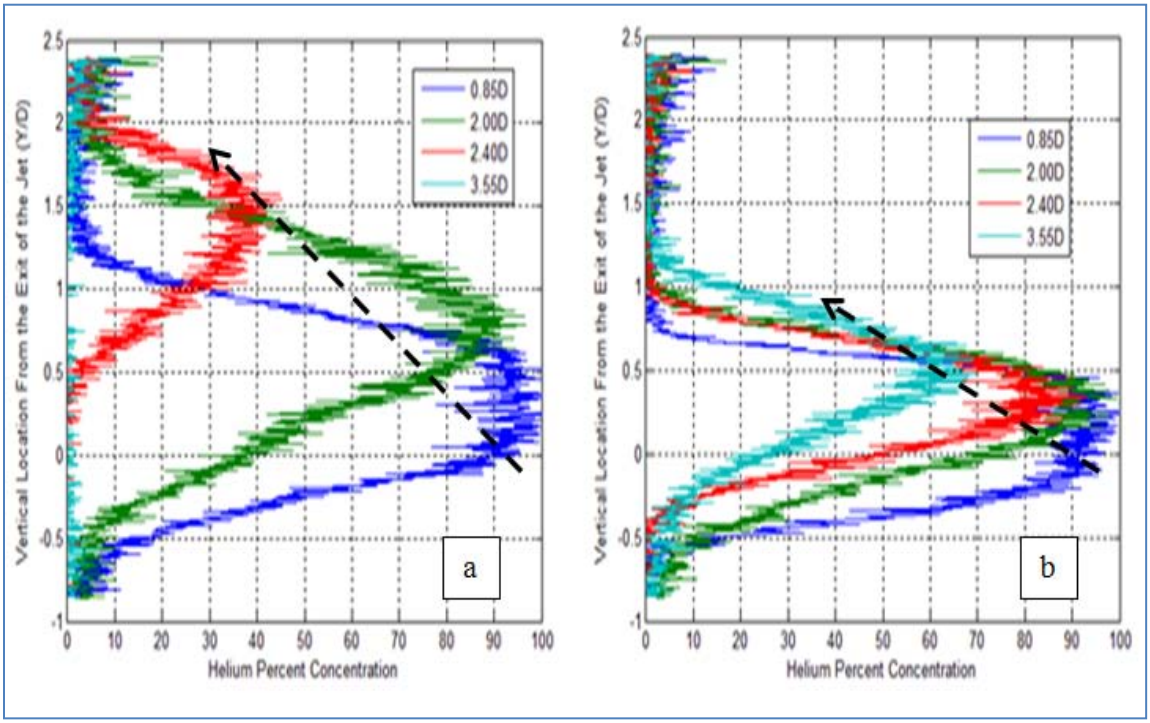

Figure 66. Helium Concentration Profiles: (a) Without Co-flow (Case 1) and (b) With Co-flow (Case 2)

Clearly, the addition of the co-flow straightens the trajectory of the helium jet which maintains its overall upward curvature due to positive buoyancy effects. In addition, the profiles (in both cases) get wider as the stream-wise location increases due to the diffusion of the jet into air. The straightening and flattening of the jet can also be seen in the trajectory plots of Figure 67. The idea here is to track the approximate position of the center of the jet by identifying the location of the maximum value of concentration.

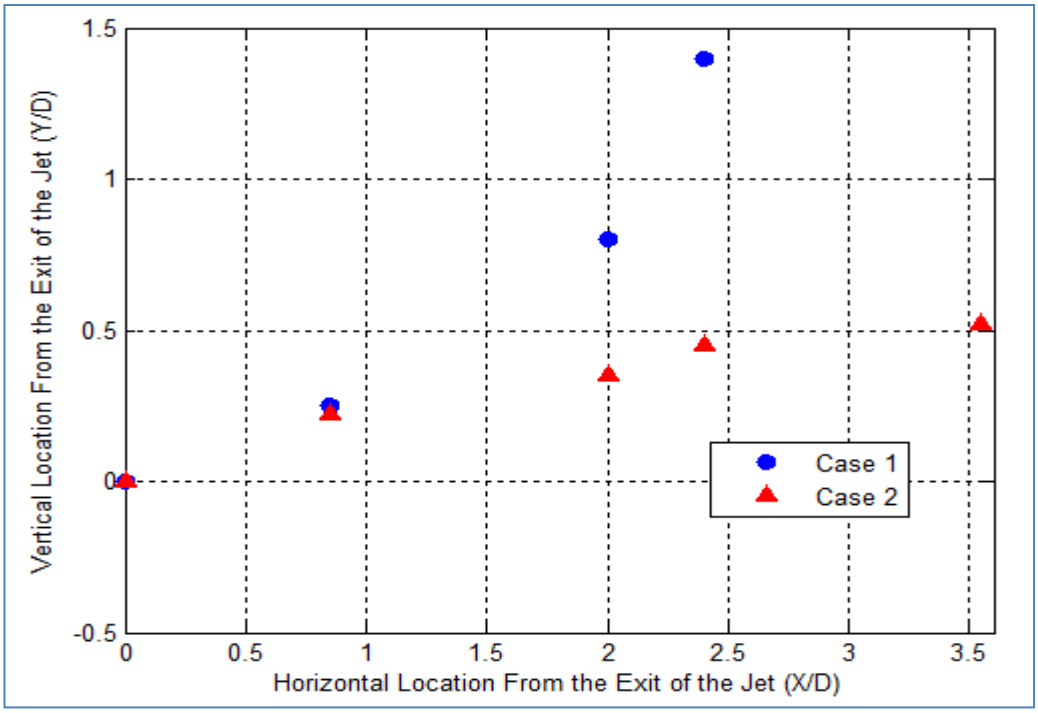

Figure 67. Helium Jet Trajectory With Co-flow (Case 1) and Without co-flow (Case 2)

The work of Reeder *et al.*, mentioned earlier in the literature review section, provides jet core trajectory data that could be checked against the findings of this study. The horizontal and vertical locations have to be, however, normalized by a length scale for "the transition of a horizontal buoyant jet to a plume" L_M defined by the authors as follows [18]:

$$L_M = \frac{(V_{jet}{}^2 A)^{\frac{3}{4}}}{\left[\frac{V_{jet} A g \left|\rho_{air} - \rho_{jet}\right|}{\rho_{jet}}\right]^{\frac{1}{2}}} \qquad (18)$$

The velocity of the jet is V_{jet}, A is the cross sectional area of the jet, g is the gravitational constant; ρ_{air} and ρ_{jet} are respectively air and jet densities. The value of L_M for Case 1 is calculated to be 12.0 mm. As shown in Table 2, Case 1 corresponds to a Froude number of 1.1. Case 1 trajectory points are then plotted against a case from Reeder *et al.* study with a value of Froude number of 1.14 as shown in Figure 68. Reeder *et al.* used a weighted averaged method to generate the trajectory data points shown in Figure 68. Despite the fact that the two studies used

different methods to track the trajectory of the jet, the two curves are in a very strong agreement. This comparison indicates that that tracking the jet using the maximum value of concentration for each stream-wise profile is a valid approach.

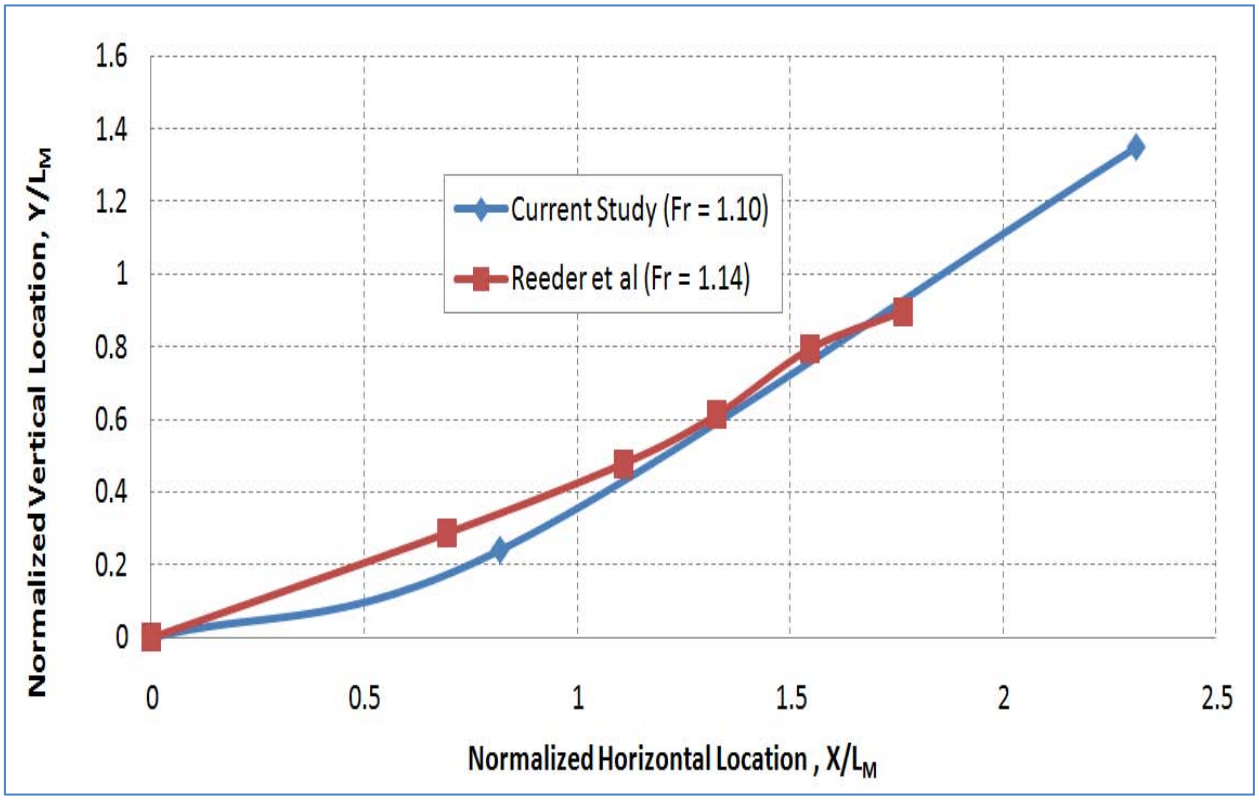

Figure 68. Comparing Case 1 of the Helium Configuration Trajectory Points to the Literature

IV.2.2. Cases With CO_2 Gas

Various cases were run to construct sufficient data to allow for the qualitative investigation of both the trajectory behavior and mixing properties of the CO_2 jet as a function of different parameters. These parameters include the velocity of air (the co-flow velocity), the CO_2 jet velocity, the relative velocity of the jet with respect to the co-flow, the velocity ratio, Reynolds number, and Froude number. These cases are illustrated in Table 3.

Table 3. Processed Cases of Different Flow Conditions for the CO_2 Jet

Cases	D (mm)	V_{air} (m/s) (co-flow)	V_{CO2} (m/s)	$V_{ratio} = \frac{V_{CO2}}{V_{air}}$	$\Delta V = \lvert V_{CO2} - V_{air} \rvert$ (m/s)	Re_{jet}	Fr_{jet}
1	8.94	0	0.305	∞	0.305	339	1.73
2	8.94	0.305	0.305	1	0	339	1.73
3	8.64	0	0.458	∞	0.458	509	2.6
4	8.94	0.305	0.458	1.5	0.153	509	2.6
5	8.94	0	0.610	∞	0.610	678	3.45
6	8.94	0.305	0.610	2	0.305	678	3.45
7	8.94	0.153	0.153	1	0	149	0.75
8	8.94	0.610	0.610	1	0	678	3.45
9	8.94	0.610	0.914	1.5	0.305	1017	5.18
10	11.53	0.610	0.695	1.14	0.085	992	3.45
11	17.15	0.610	0.854	1.4	0.24	1800	3.45
12	8.94	0.610	1.23	2	0.610	1356	6.91
13	8.94	0.914	1.83	2	0.914	2034	10.37
14	8.94	1.23	1.23	1	0	1370	7
15	17.15	0.67	0.67	1	0	1430	2.75
16	11.53	0.779	0.997	1.128	0.218	1430	4.97
17	8.94	1.117	1.28	1.15	0.163	1430	7.3

Figure 69a and Figure 69b show the mean concentration for series of 3000 images taken for two different cases. The six separate vertical lines in each plot correspond to three separate runs as two lines are imaged in each time sequence. Case 1(shown in Figure 69a) represents a typical jet flow, with a jet velocity of 0.305 m/sec and no co-flow configuration. Case 2, however, shown in Figure 69b differs from Case 1 (Figure 69a) by the addition of a co-flow of air going at the same speed as the CO_2 jet of Case 1. As expected, the heavier than air jet is subject to a negative buoyancy effects resulting in the CO_2 concentration locations following a curved down trajectory in both cases.

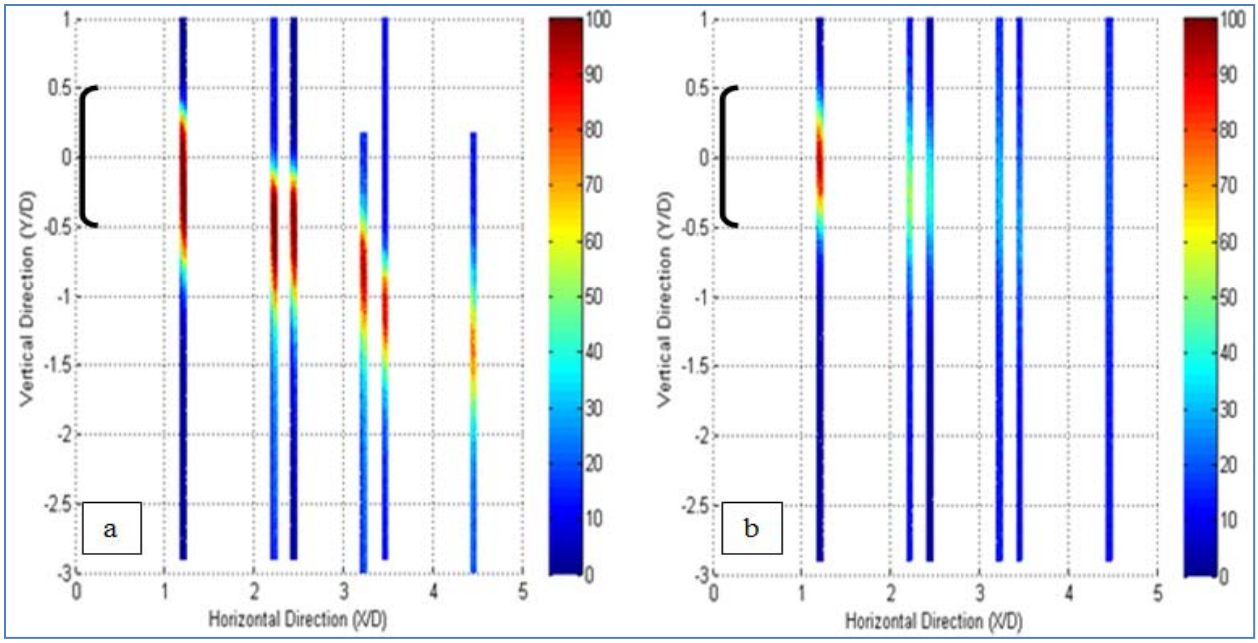

Figure 69. CO_2 Jet Concentration Plots: (a) Without Co-flow (Case 1), and (b) With Co-flow (Case 2)

Significant changes occur to the flow structure and behavior when a co-flow of air is introduced as seen in Case 2 concentration and standard deviation plots. First, the trajectory becomes flatter as noticed when comparing Figure 69a and Figure 69b. The concentration of the CO_2 drops to less than 10% at X/D = 4.4 as opposed to 65% at the core of the jet in the Case of no co-flow. Furthermore, stronger regions of mixing (as seen in Figure 70b) are developed even at closer locations away from the exit of the jet (X/D = 1.2). For both Case 1 and Case 2, the increase in mixing is more pronounced with downstream distance. As shown in Figure 70b, for instance, starting from a jet location of X/D = 3.2, the fluctuation of the jet intensity (concentration) becomes more significant especially along the shear layers on the top and bottom of the core of the jet. At 4.4 D, the region of the center of the jet was subject to the strongest fluctuations indicating mixture of the center of the jet with ambient air. As expected, the level of fluctuation is more significant in the bottom shear layer than on the top due to the uneven density distribution resulting from the existing negative buoyancy. The mixing of the jet with the co-

flowing air moves progressively from the top and bottom shear layers to the core of the jet. This entrainment results in the significant decrease of the CO_2 concentration as the jet travels downstream.

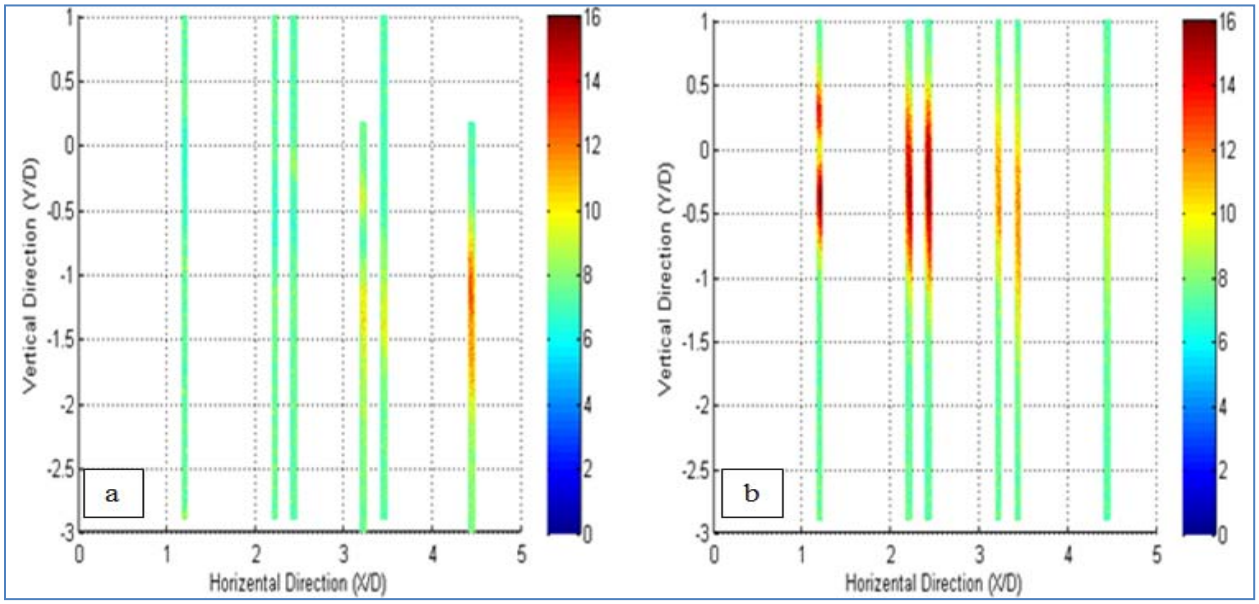

Figure 70. Standard Deviation of CO_2 Intensity: (a) Without Co-flow (Case 1) and (b) With Co-flow (Case 2)

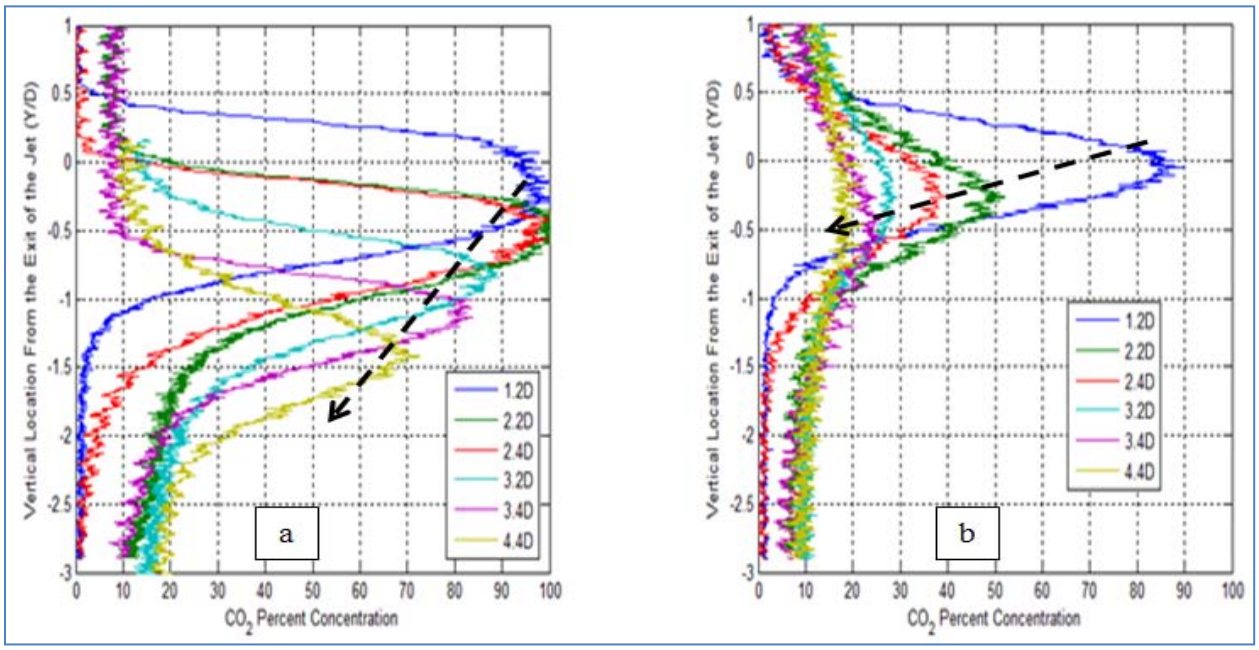

Figure 71. CO_2 Concentration Profiles: (a) Without Co-flow (Case 1) and (b) With Co-flow (Case 2)

The changes in the jet behavior the addition of the co-flow causes are also highlighted in Figure 71. The flattening of the jet trajectory can be noticed by comparing the profiles of Case 1 (Figure 71a) to that of Case 2 (Figure 71b). In addition, the figures indicate a decrease in the CO_2 concentration with downstream distance from the exit of the jet for both with and without co-flow. Furthermore, there is an overall spreading of the jet due to the mixing of the CO_2 with the ambient air. Unlike the cases with the helium jet, the co-flow in the case of the CO2 jet seems to increase the mixing of the jet and its diffusion into air.

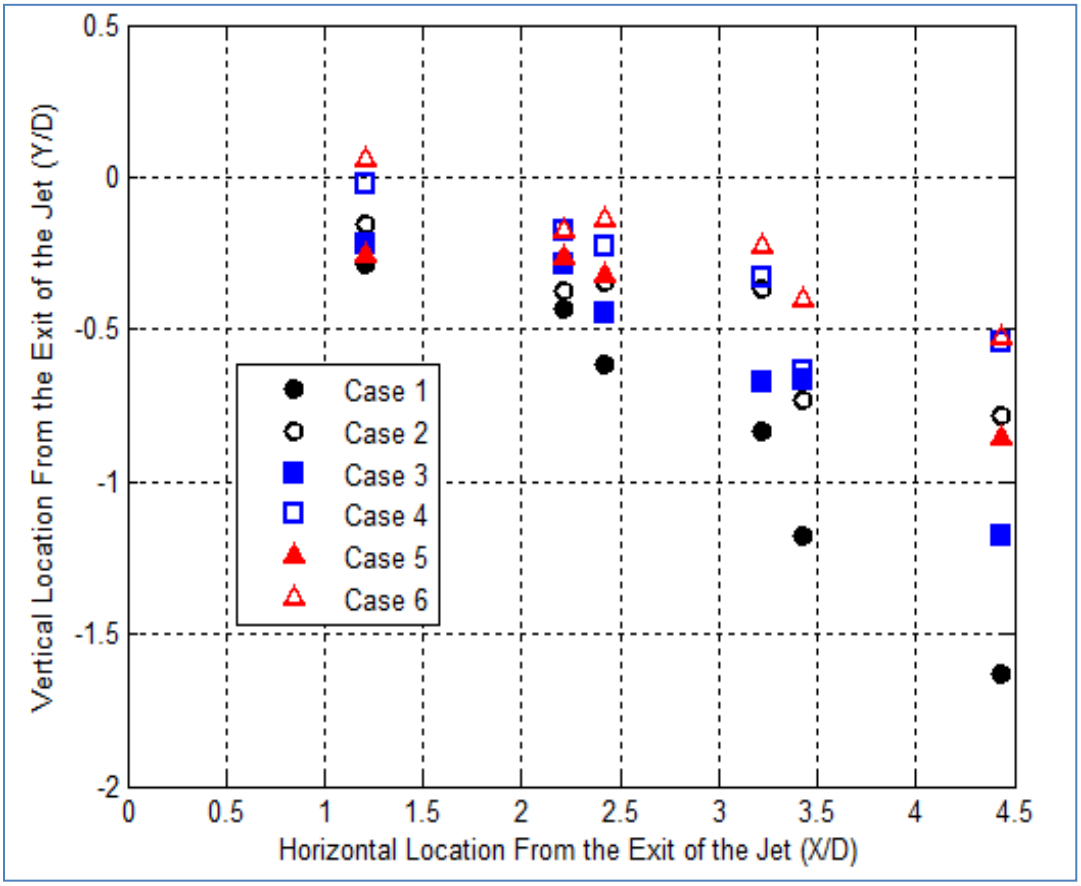

Figure 72. Comparing Jet Trajectory for no Co-flow Cases (1, 3 and 5) and With Co-flow Cases (2, 4, and 6)

As part of the analysis of the jet behavior, trajectory plots were also generated. Figure 72 compares the trajectory of CO2 jets at Froude numbers of 1.73, 2.6, and 3.45 for conditions with

and without a co-flow of 0.305 m/s. Readily apparent is that the addition of the co-flow significantly flattened the trajectory of the jet. For example when the co-flow is added, such as in Case 2, the trajectory curvature decreased and the jet dropped with only a vertical position of Y/D= -0.5 as opposed to approximately -1.5 for Case 1. Although they had the same jet velocity (0.305 m/sec), the two cases had different trajectory pattern which indicates the need to alter the classical definition of Froude number (Equation 8) to incorporate the effects of co-flow on the buoyancy of the jet and its trajectory. In addition, for a velocity ratio of 2.0 (Case 6), the jet has greater momentum than Case 2 (velocity ratio of 1.0) and Case 4 (velocity ratio of 1.5) and hence exhibits a smaller overall vertical drop of 0.40 D at X/D = 3.5 as opposed to 0.60 D for Case 2. Similar investigation was performed by comparing cases 1, 3, and 5. The co-flow velocity for these cases however was kept at 0 m/sec while the jet velocity varied from 0.305 m/sec (Case 1) to 0.458 m/sec (Case 3) to 0.610 m/sec (Case 5). As shown in Figure 72, the effect of buoyancy (curving the trajectory) is more pronounced in the absence of the co-flow. In addition, the higher the jet velocity, the smaller the overall drop of the jet at 4.4 D. Cases 3 and 5 have close values of Froude number (2.6 and 3.45) which explains the similarity between their respective trajectories. This indicates that in the absence of the co-flow, the classical definition of the Froude number holds true. Overall, for both the co-flow and no co-flow cases, the trajectory is less curved as the jet velocity (and thus the Froude number) increases.

Case 1 core jet trajectory, which corresponds to a Froude number of 1.73, can be compared against a comparable case from the literature with Froude number of 1.8. The length scale for Case 1 is found to be about 14.50 mm. Figure 73 below illustrates this comparison which indicates a relatively close agreement between the two studies.

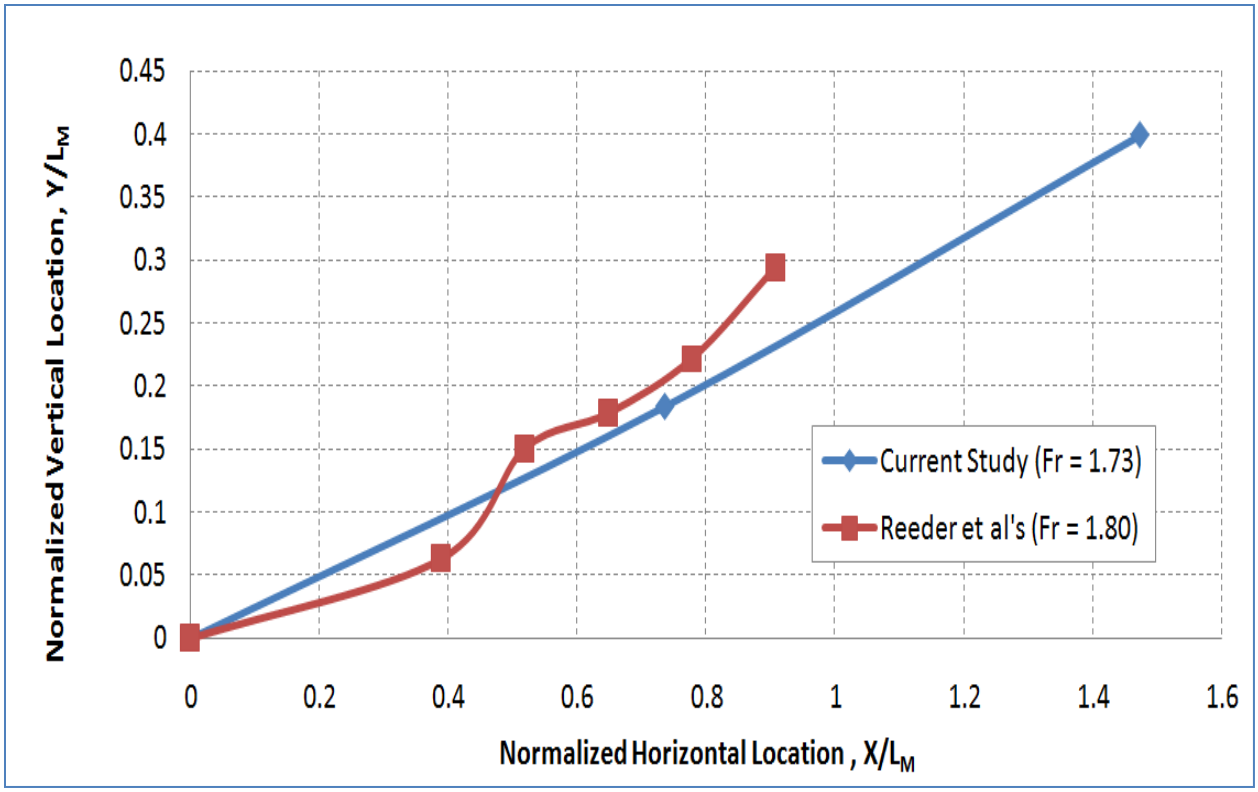

Figure 73. Comparing Case 1 of the CO_2 Configuration Trajectory Points to the Literature

The data presented up to this point with the exception of the standard deviation plots is time averaged data that does not reflect the time resolved aspect of this study. Hence, highlighting the behavior of the jet as a function of time is the objective of this section. As shown in Figure 70, the addition of the co-flow to the flow fields causes the unsteadiness of the jet concentration that increases as the stream-wise location (X/D) increases. In order to convey this unsteadiness seen in the collected images of Case 1 (without the co-flow), and Case 2 (with co-flow), Figure 74 is generated. It illustrates a comparison between these two cases using four images of each case taken at four different instants in time. While the jet remains relatively steady over time in the absence of the co-flowing air, it exhibits significant unsteadiness when air is added to the flow field.

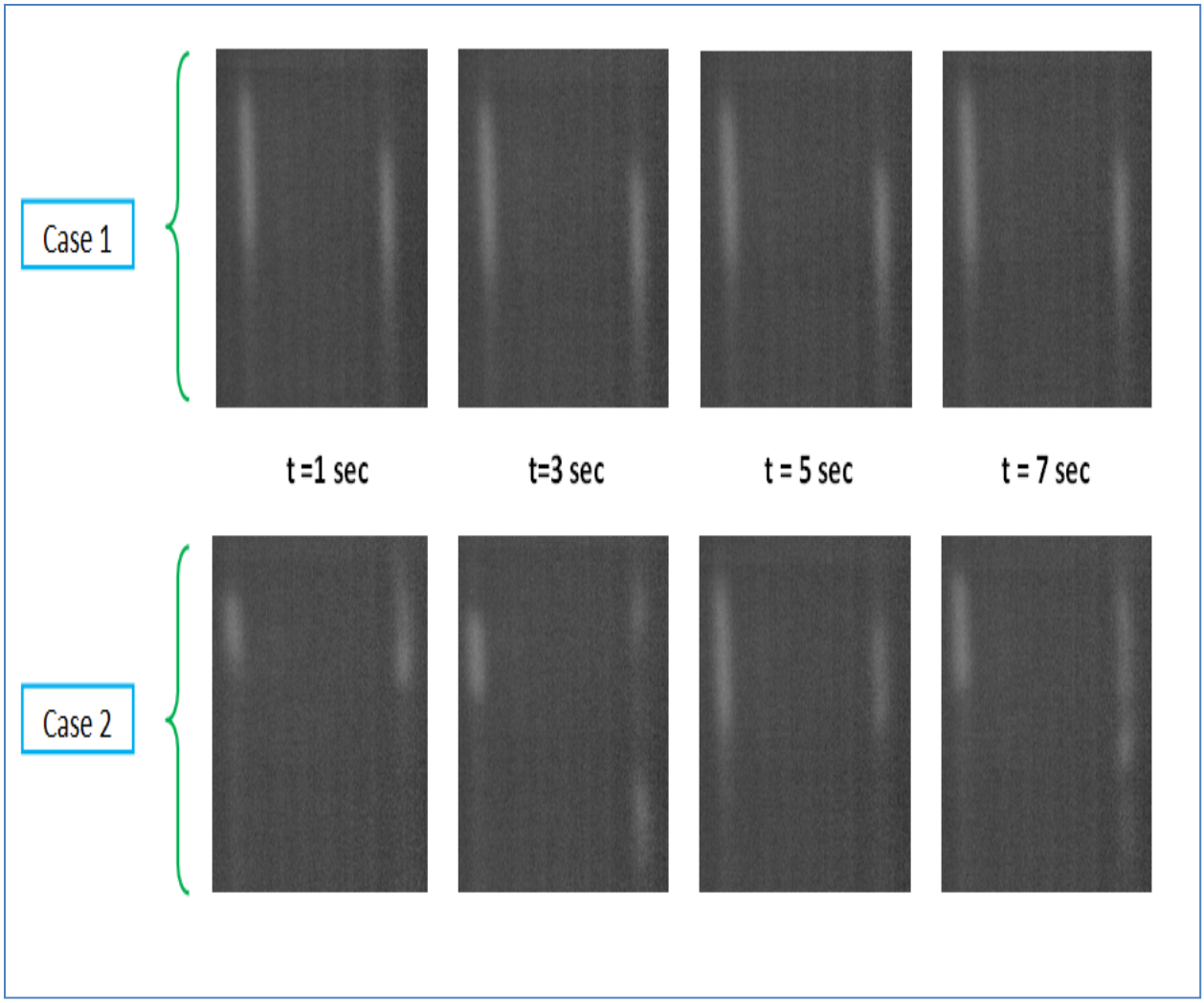

Figure 74. CO_2 Raw Data Images With Co-flow (Case 2) and Without Co-flow (Case 1)

The significant changes introduced by the addition of the co-flow prompts the investigation of time resolved data of the mixing regions. Figure 75a and Figure 75b illustrate the two dimensional standard deviation plots for Case 1 and Case 2 respectively. As shown in Figure 75a, minimal mixing occurs at 1.2 D away from the exit of the jet with a small increase of the level of fluctuations in the top and bottom shear layers. Case 2, however, exhibits significant fluctuations level at the shear layers and was therefore used as a baseline for time histories analysis. The standard deviation plot of Case 2 at X/D = 1.2 D is shown in Figure 75b.

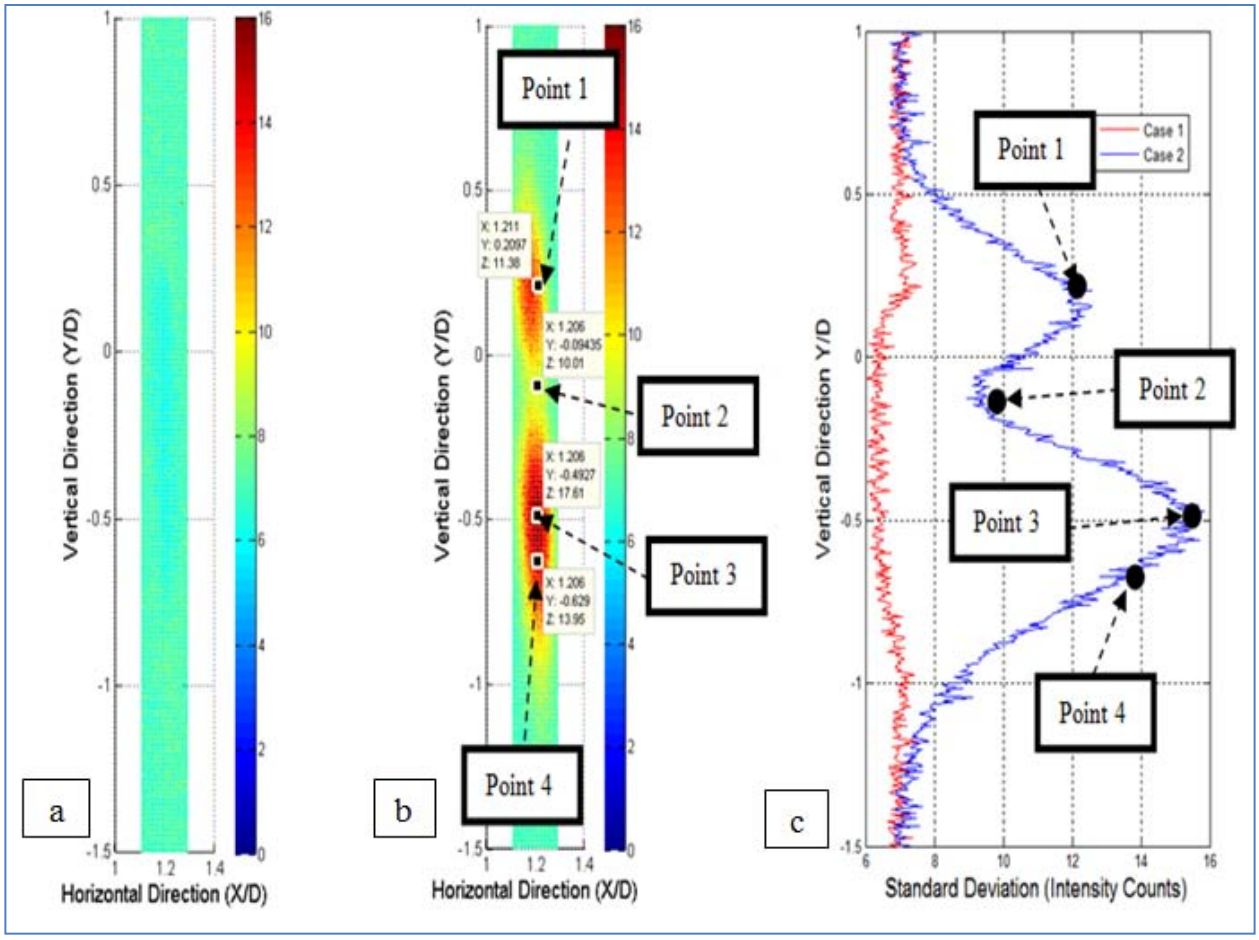

Figure 75. Two Dimensional Standard Deviation Plots of: (a) Case 1 (V_{jet} = 0.305 m/sec, $V_{co\text{-}flow}$ = 0 m/sec), (b) Case 2 (V_{jet} = 0.305 m/sec, $V_{co\text{-}flow}$ = 0.305 m/sec), and (c) Comparison of Case 1 and Case 2

Four points of interest were then chosen based on the plot of the standard deviation (as shown in Figure 75b). Time histories of points 1, 2, 3, and 4 are plotted together in Figure 76. Points 1, 3, and 4 correspond to peaks in the fluctuations due to the top and bottom of the shear layer regions. Point 2 corresponds to a point of low standard deviation which is relatively away from the shear layer and close to the core of the jet where less mixing occurs (at that X/D location). Note that the intensity counts indicated in Figure 76 and Figure 77 are much higher than those shown in previous standard deviation plots. This is because nine pixels are binned together for each point location to minimize noise and obtain cleaner time history plots. As evident from these time histories, the fluctuations in the upper and lower shear layer are regular

in time indicative of steady mixing between the core CO_2 intensity of about 450 and the air only intensity of 100 counts. However, at Point 2 the fluctuations are very intermittent, yet at the same magnitude. This is expected since Point 2 is in the core region of the jet. Pure CO_2 was present most of the time at this location. However, at times, air was clearly penetrating into the core. More likely, what was occurring was that the CO_2 jet was oscillating in space over this time period. This was evident in watching the FRS signal while the data was collected. This oscillation did not occur for Case 1 as seen in Figure 70a, where the unsteadiness was significantly less.

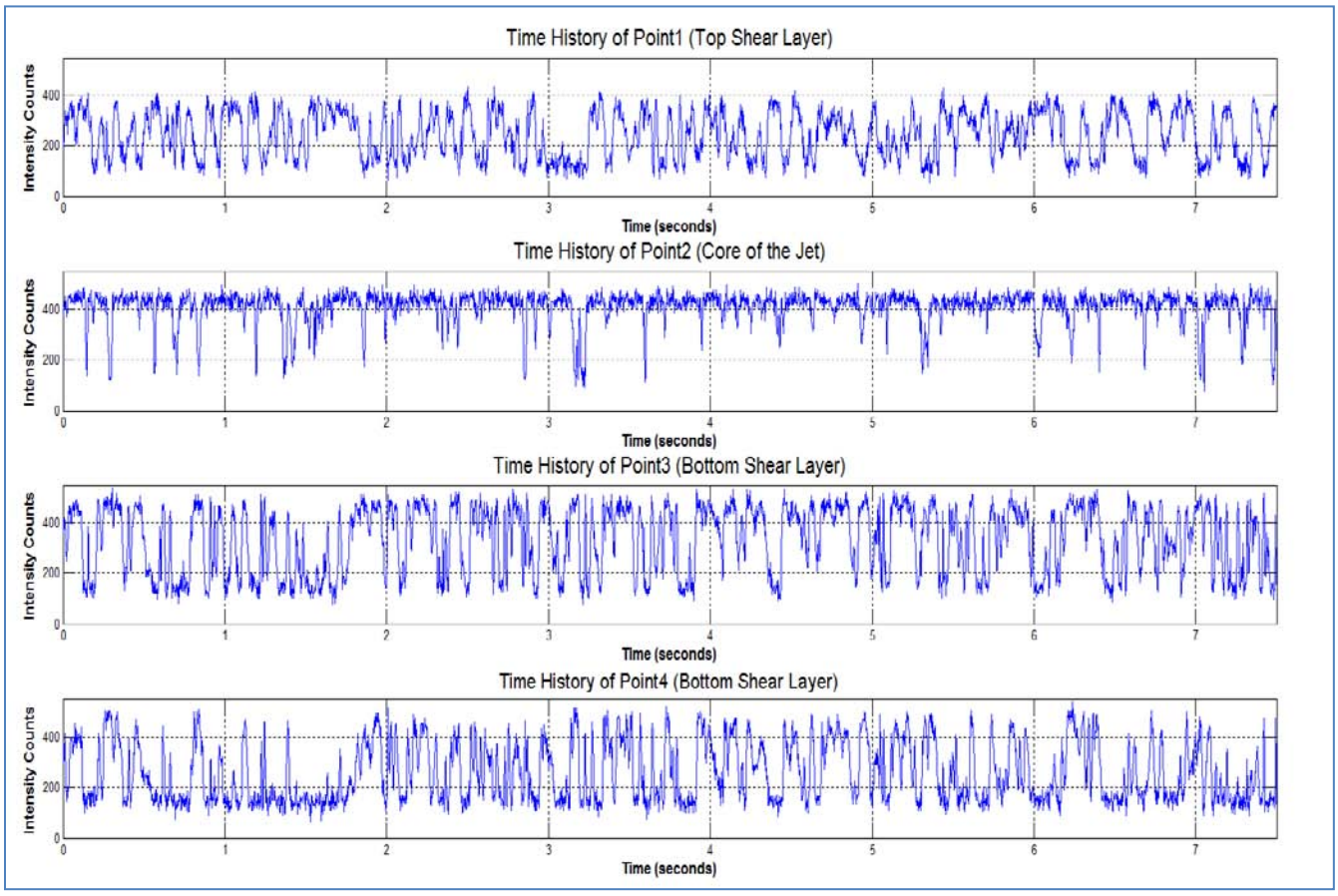

Figure 76. Time Histories of Four Points on the First Line at 1.2 D in the Horizontal Direction for Case 2 (V_{jet} = 0.305 m/sec, $V_{co\text{-}flow}$ = 0.305 m/sec).

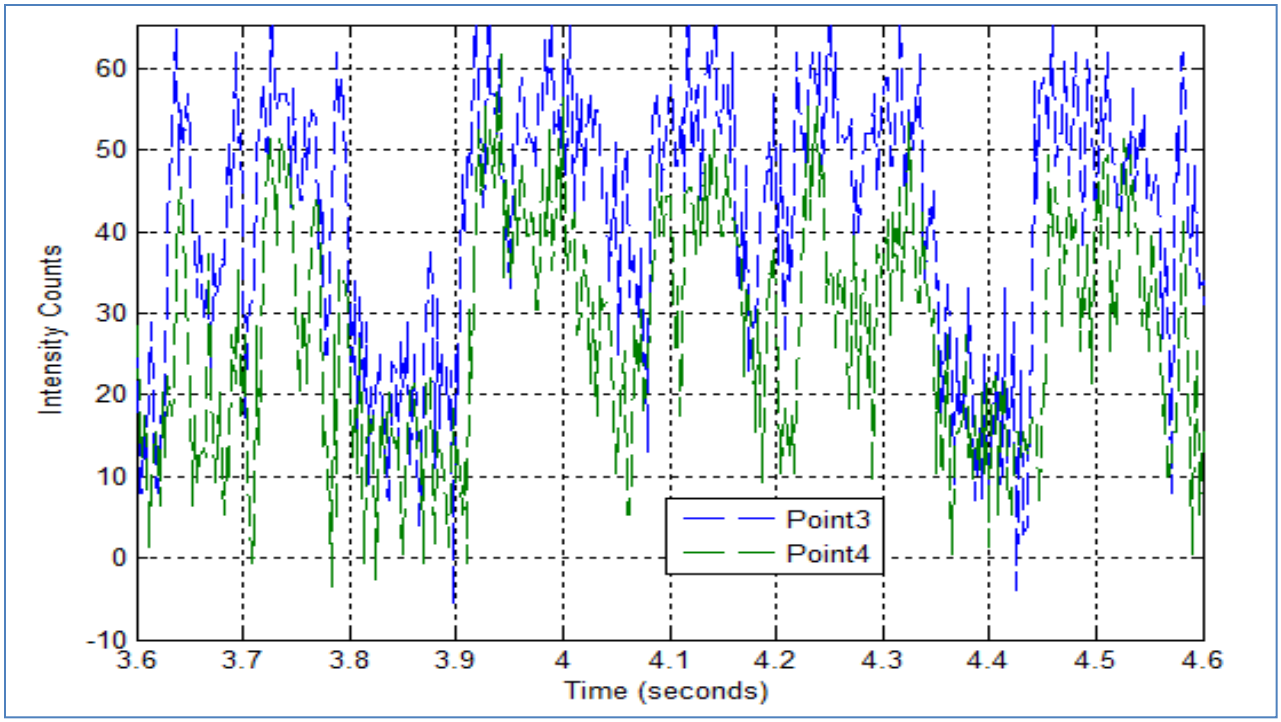

Figure 77. Time Histories of Points 3 and Point 4 of Case 2 (V_{jet} = 0.305 m/sec, $V_{co\text{-}flow}$ = 0.305 m/sec).

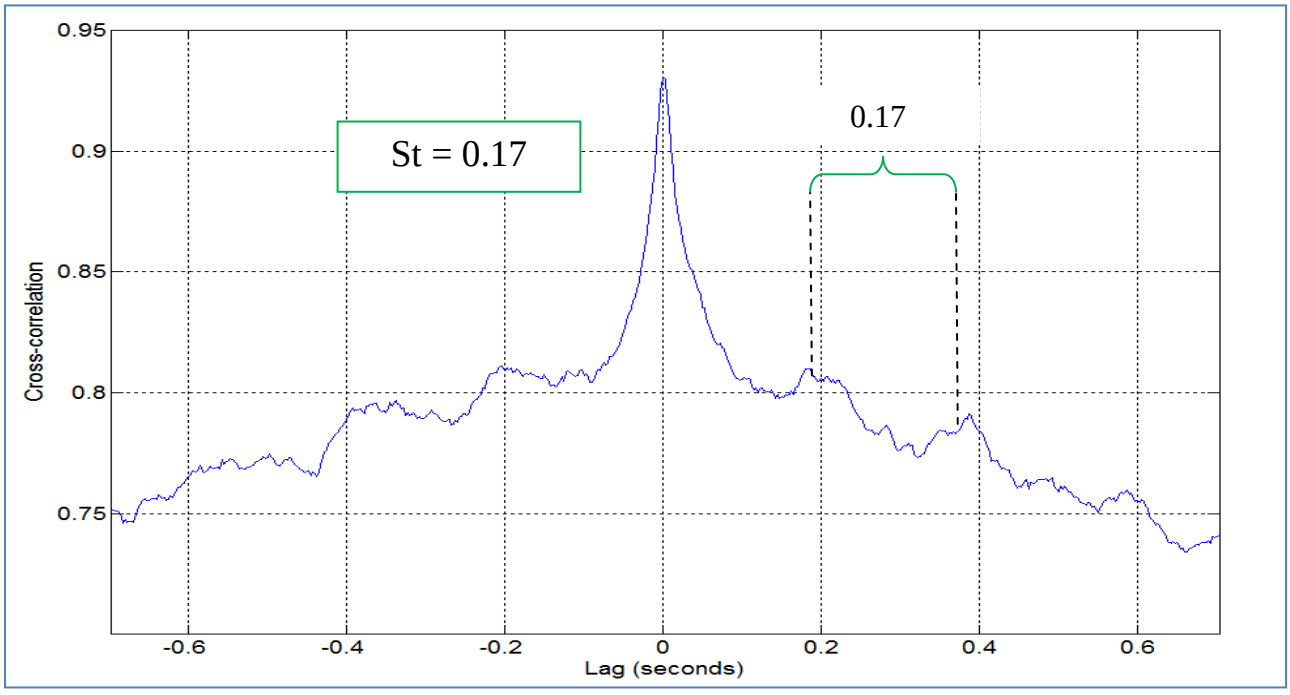

Figure 78. Cross-Correlation of Point 4 to Point 3 of Case 2 (V_{jet} = 0.305 m/sec, $V_{co\text{-}flow}$ = 0 m/sec)

Figure 77 was generated in light of what appeared to be a time lag between Point 3 and Point 4 time histories given in Figure 76. These two points were located in the area of high fluctuations in the lower shear layer, as shown in Figure 75b. As indicated above, the two points have the same X/D location (1.206 D) and are offset by a vertical distance of 0.13 D or 1.15 mm. From the cross correlation plot (shown in Figure 78), there exists a small time lag (less than 0.0025 seconds) between the time histories of the data taken from the two locations. The magnitude of the lag indicates a correlating velocity of 0.46 m/sec between the two points; while the high correlation between Point 3 and Point 4 was indicative of that the structure of the vortices was regular and coherent. Furthermore, the secondary peaks in the cross correlation (shown in Figure 78) suggest the presence of a repeating pattern every 0.17 seconds (5.9 Hz) which could be associated with the shedding frequency of the flow structure. This frequency corresponded to a Strouhal number (St) of 0.173. The Reynolds number is 339 for this case which corresponded to a Strouhal number of 0.20 for a flow around a cylinder traveling at a comparable speed to that of Case 2. This compares favorably with the work of Baranyi *et al.* [27].

In addition, it is often useful when time resolved data is collected to perform a Fast Fourier Transform (FFT) on the time dependent information to identify the frequency content of the signal. An FFT is then performed on a 20 second long time history of Point 3 of Case 2 as indicated above. The frequency spectrum of the signal, shown in Figure 79, indicates the presence of a frequency at 6 Hz which could correspond to the same frequency (5.9 Hz) identified through the correlation plots.

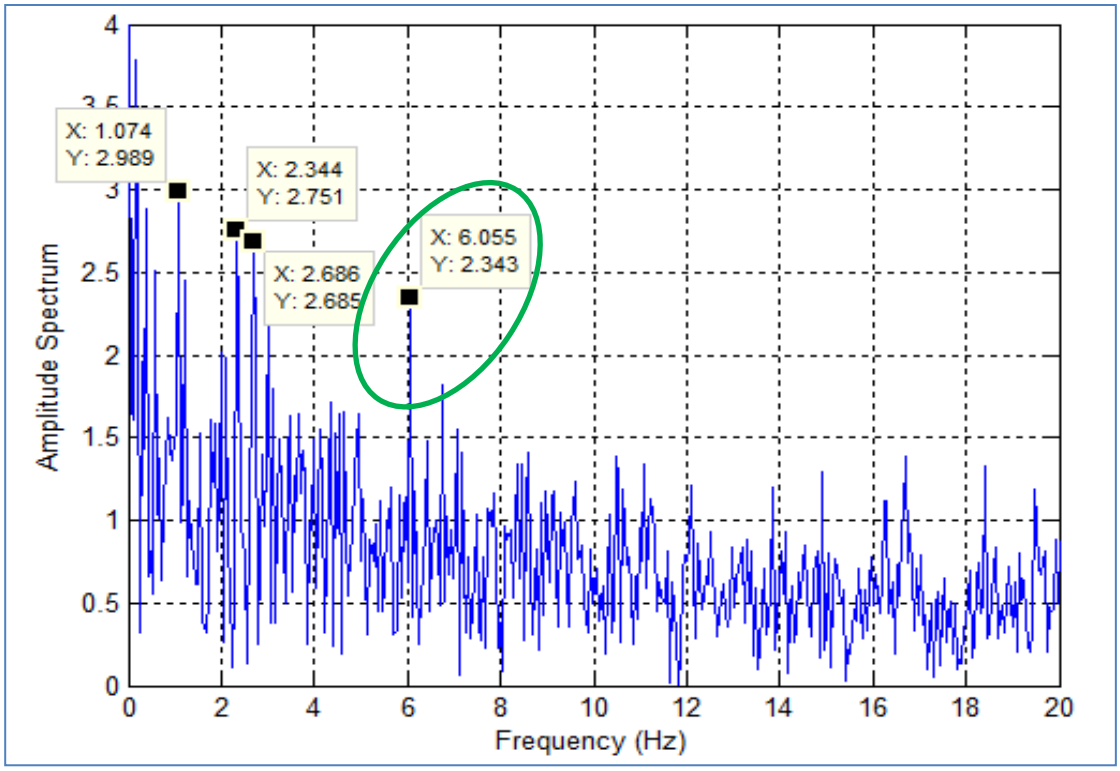

Figure 79. Frequency Content of 20 Second Long Time History of Point 3 of Case 2

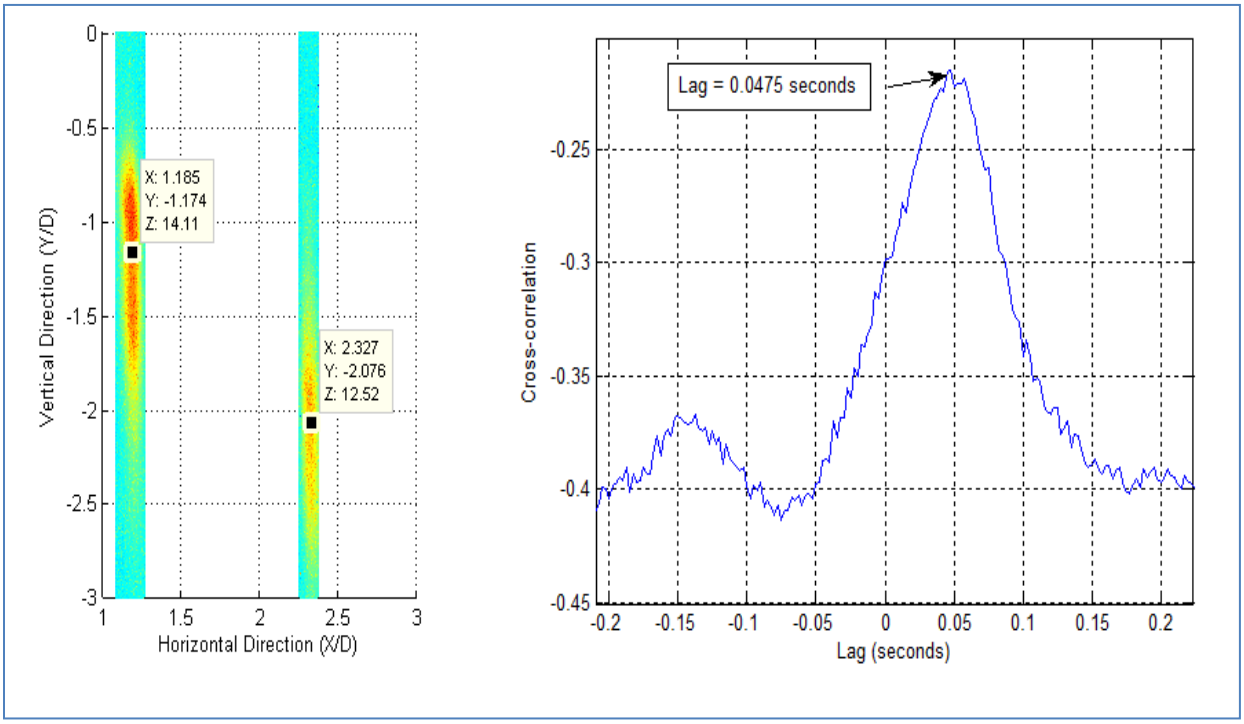

Figure 80. Two Lines Cross- Correlation for Case 7 (V_{jet} = 0.153 m/sec, $V_{co\text{-}flow}$ = 0.153 m/sec)

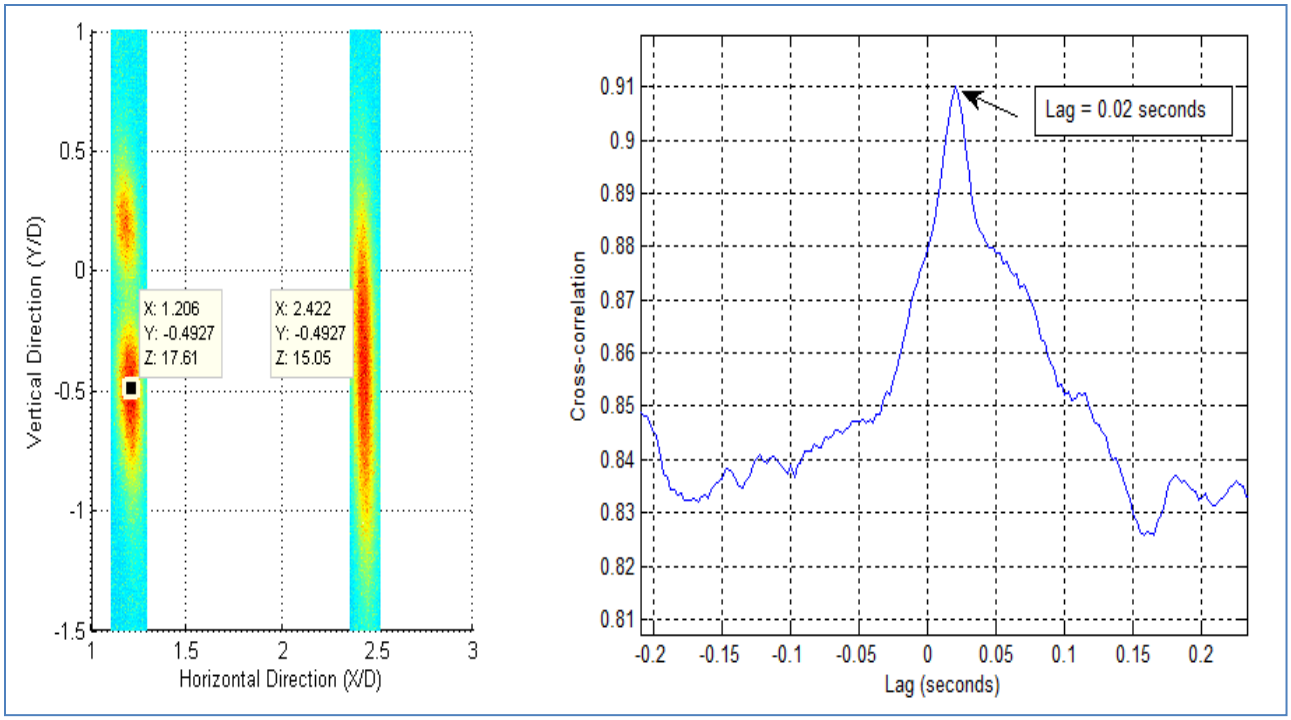

Figure 81. Two Lines Cross- Correlation for Case 2 (V_{jet} = 0.305 m/sec, $V_{co\text{-}flow}$ = 0.305 m/sec)

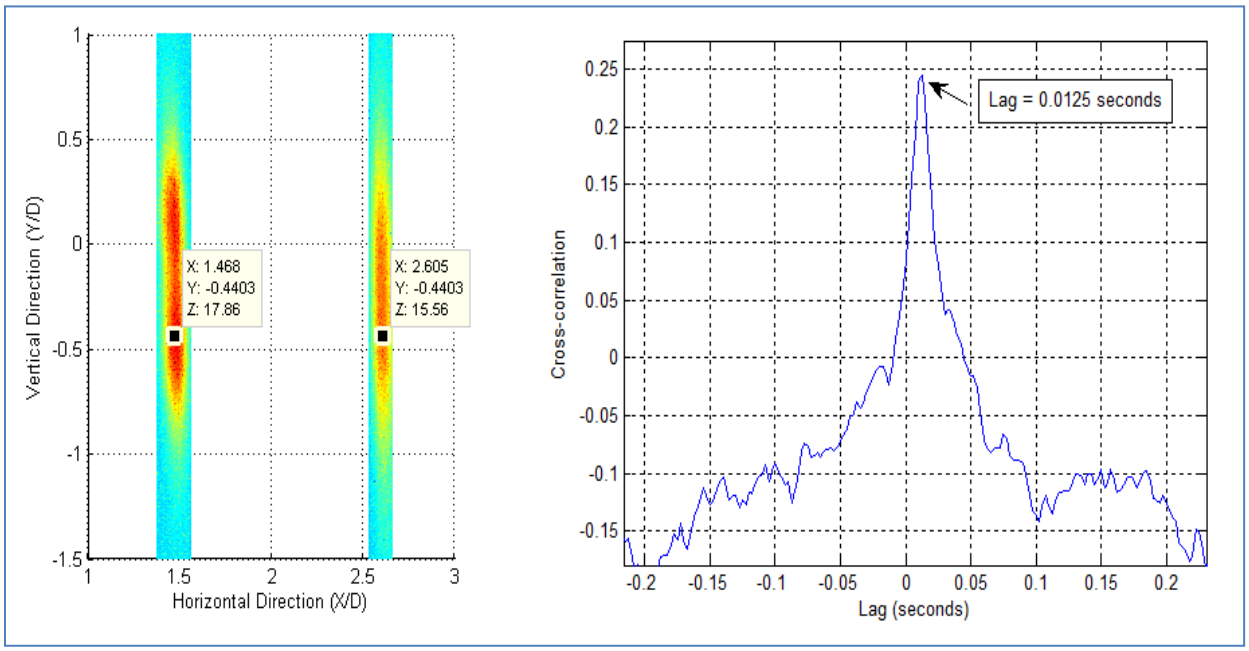

Figure 82. Two Lines Cross- Correlation for Case 8 (V_{jet} = 0.610 m/sec, $V_{co\text{-}flow}$ = 0.610 m/sec)

Figure 80, Figure 81, and Figure 82 show cross-correlation plots between a point on the first line (at 1.2 D away from the exit of the jet) and a point on the second line (at 2.4 D away from the exit of the jet) for cases 7, 2, and 8 respectively. Standard settings for the *xcorr* routine in MATLAB were applied, and as a result, the values on the vertical axis should not be compared from one plot to another, as they are affected by the standard deviation for each point. Nonetheless, the peak corresponding to a lag time for a given plot may be used to characterize events in the flow field. The ratio of the jet velocity to the co-flow velocity was maintained at 1.0 for all three cases. For cases 7, 2, and 8, the jet velocities are respectively 0.153 m/sec, 0.305 m/sec, and 0.610 m/sec. These cases enable correlation plots to deduce the mean convective velocities of flow features within the jet. Figure 80, Figure 81, and Figure 82 indicate the presence of a significant lag of 0.0475 sec, 0.02 sec, and 0.0125 sec respectively between points of the first line and points of the second line which is expected. As shown in Figure 80, the chosen point on the second line is not on the same height as the point on the first line due to the drop of the jet trajectory. This vertical drop due to buoyancy increased the distance the jet traveled between the first and second point and hence added to the time lag. The corresponding convective velocities given the horizontal distances between the points of the first line and those of the second line are respectively 0.225 m/s, 0.536m/s, and 0.858 m/s. These values are higher than the actual jet velocities of cases 7, 2, and 8. This significant difference between the calculated and expected convective velocities can be due in part to the fact that the flow exiting the tube is unlikely to have a top hat profile but, rather, would have velocities higher than the nominal values listed in Table 3 in the core of the jet. On the other hand, as the jet velocity increased proportionally with the mass flow controller setting, the correlation peaks shifts to a smaller time lag, which is an expected trend. In other words, the shift in the time lag is inversely

proportional to the increase in the jet velocity, demonstrating the value of the measurement technique.

The second portion of the data analysis involves investigating the effects of the parameters discussed previously on the jet trajectory. In Figure 83, the relative velocity was kept constant at 0.305 m/sec while the velocity of the jet was changed. The jet velocity for Case 9 was three times that of Case 1 and one and a half that of Case 6 which corresponded to a Froude increase from 1.73 to 3.45 to 5.18. Readily apparent was that the trajectory was straighter for the higher Froude number jet (i.e. higher velocity). This highlights the importance of the jet velocity in shaping the trajectory. This also suggests that the relative velocity between the jet and core flow is not the proper scaling velocity for buoyant flows.

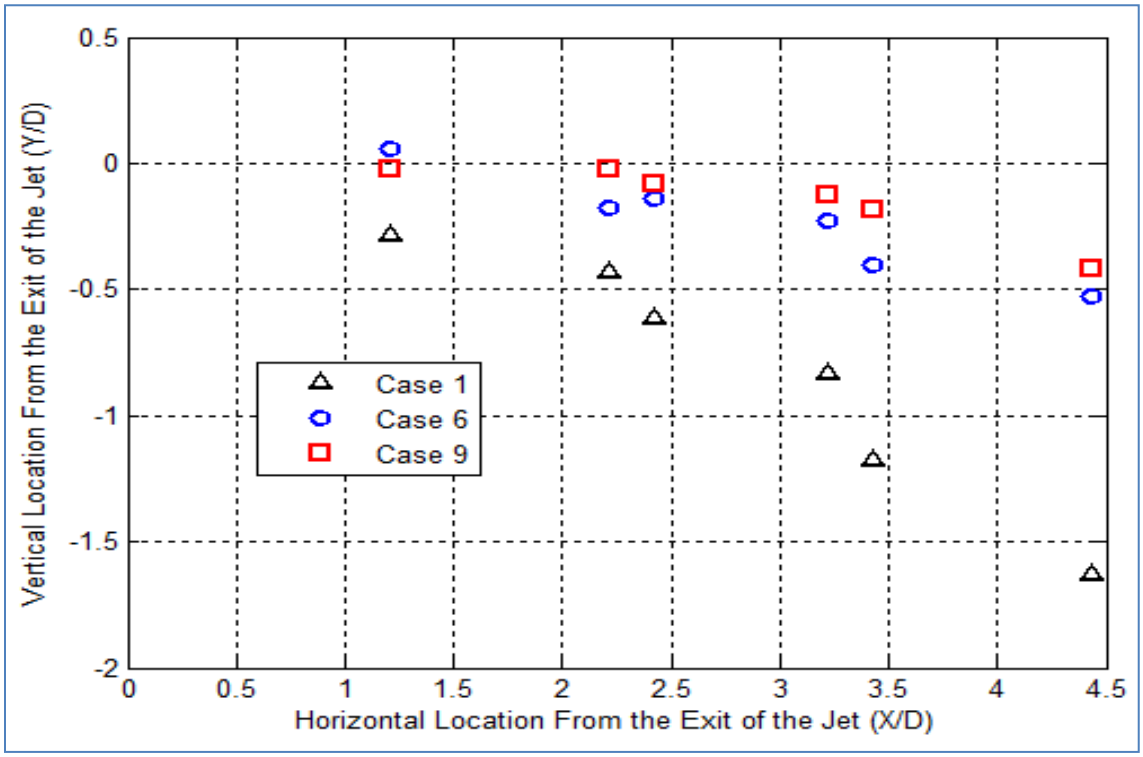

Figure 83. Effects of Jet Velocity on the Jet's Trajectory

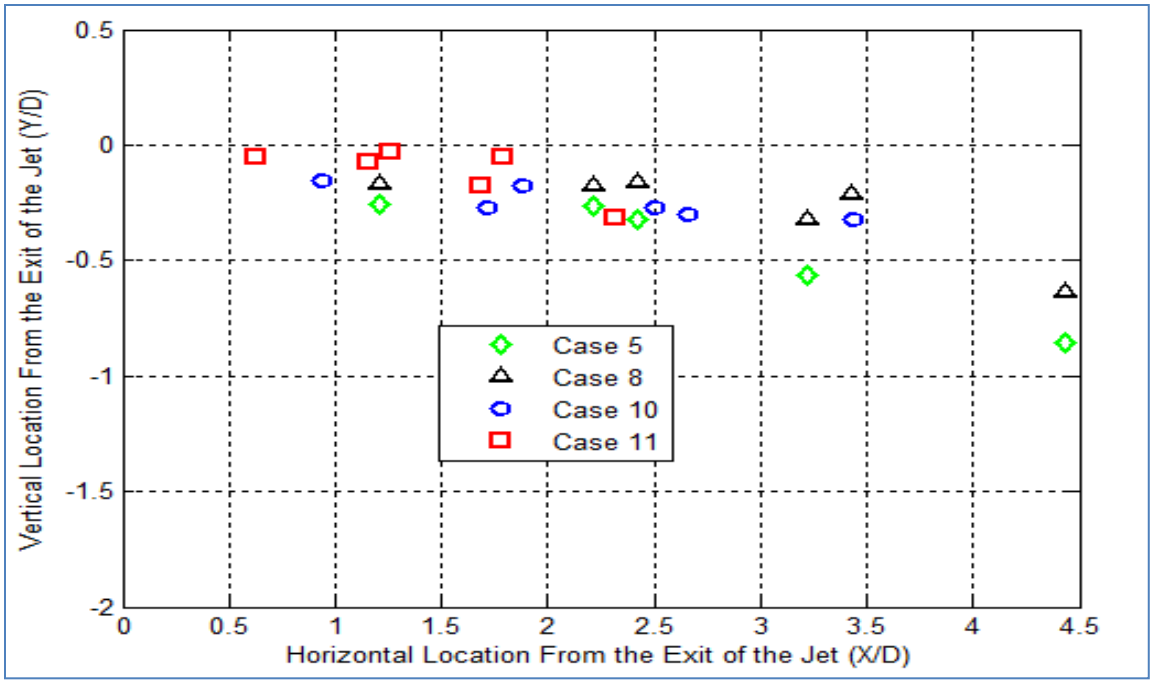

Figure 84. Effects of Froude Number on the Jet's Trajectory

A set of runs were performed while maintaining the Froude number constant. To accomplish this, three different combinations of jet diameter were used. Cases 8, 10 and 11 shown in Figure 84, corresponded respectively to Reynolds number values of 678, 992, and 1800. It might be expected that Case 11, with a Reynolds number of 1800, would have a relatively higher trajectory than the other two cases. However, all these cases corresponded to a Froude number of 3.45 based on jet velocity and diameter (based on the classical definition of the Froude number of Equation (8)). As indicated in Figure 84, all three of these cases maintained a tight distribution suggesting that the Froude number has a substantial impact on the trajectory. One note is that these three cases all maintained a constant co-flow velocity of 0.610 m/s. To look specifically at the effect of the co-flow, Case 5, which corresponds to Case 8 without the co-flow, was also plotted. The curvature of the trajectory was more pronounced in Case 5. This reemphasized that the presence of the co-flow impacts the overall structure of the jet, including the turbulence, as well as altering the buoyancy. However, it does not appear that

once the turbulence is increased, that any further increases in the co-flow velocity has any further effect.

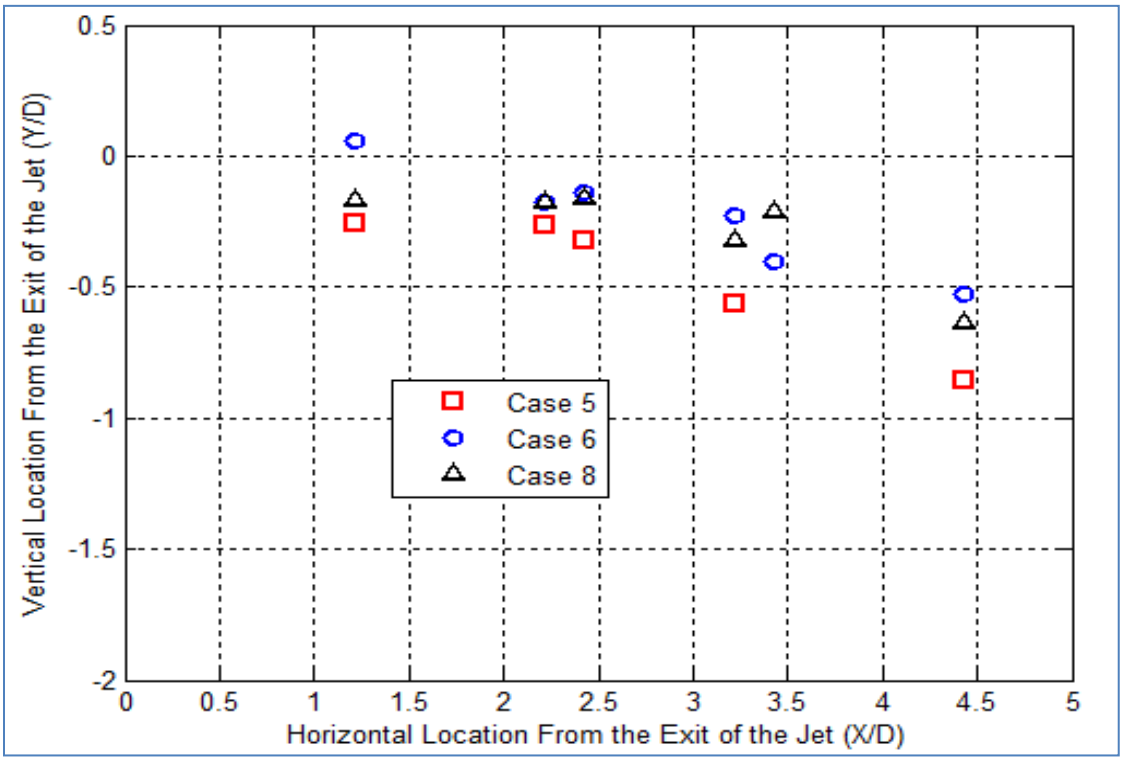

Figure 85. Effects of Relative Velocity on the Jet's Trajectory (Maintaining Fr = 3.45)

In order to further investigate the impact of the relative velocity on the jet's trajectory, Cases 5 and 6 were further compared to Case 8. These three configurations corresponded to a Froude number of 3.45 based on the classical definition of Froude number outlined in Equation (8). The co-flow velocity was changed from 0 (Case 5) to 0.305 m/sec (Case 6) to 0.610 m/sec (Case 8). This resulted in a substantial change in the velocity ratio and the relative velocity between the jet and the co-flow. As shown in Figure 85, Cases 6 and 8 trajectories were similar. This indicates that the relative velocity parameter had a minimal effect on the jet trajectory. It also emphasizes the significant change that occurred when the co-flow was added. The addition of the co-flow to the flow field seems to have the effect of increasing the turbulence and thus the

spreading rate of the jet. Once this turbulence is activated, a further increase in the co-flow velocity is not significant.

To better understand the impact of velocity ratio on the jet's trajectory, Cases 6, 12, and 13 were further compared. Each of these cases maintained velocity ratio of 2.0 between the jet and the co-flow. Both the jet velocity and the co-flow were increased between these cases. This resulted in an increase in the relative velocity and Froude number. For the highest value of Froude number (Case 13), the trajectory of the jet is almost linear as shown in Figure 86a. The velocity ratio between the two flows was clearly not the normalizing factor as changing the relative velocity altered the impact of the buoyancy. For these conditions, the relative velocity was increased by a factor of 2 (from Case 6 to Case 12) and by a factor of 3 (from Case 6 to Case 13). To remove influence of the relative velocity, four other cases were interrogated. These cases maintained the velocity ratio at 1.0 while also maintaining the relative velocity constant at 0. Figure 86b reveals still a significant variation in the trajectory of these jets indicative that the buoyancy still has a dominant effect. This effect is not attributed to either the velocity ratio or the relative velocity between the jet and co-flow. What did change significantly for these cases was the Froude number which took on the values of 0.75 (Case 7), 1.73 (Case 2), 3.45 (Case 8), and 7 (Case 14). Clearly for these cases, the higher the Froude numbers (and hence the jet trajectory) the straighter the trajectory of jet was. This clearly indicates that the jet velocity itself has stronger impact on the buoyancy than the co-flow velocity.

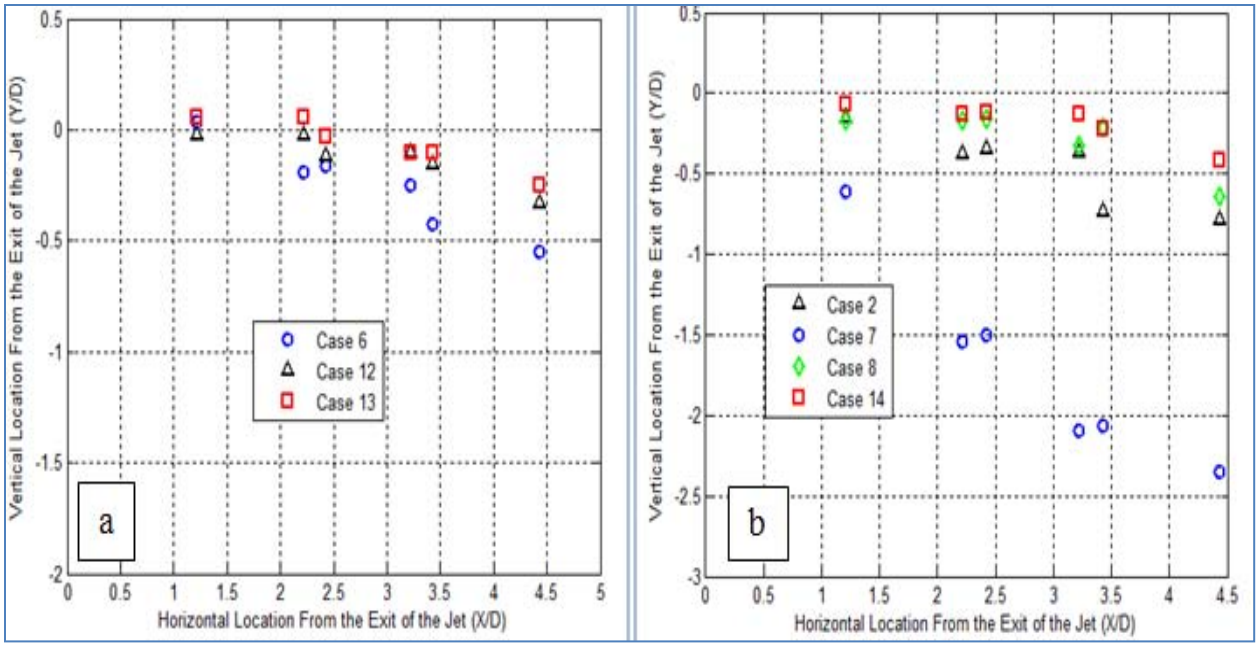

Figure 86. Effects of Velocity Ratio on the Jet's Trajectory: (a) V_{ratio} = 2.0 , (b) V_{ratio} = 1.0

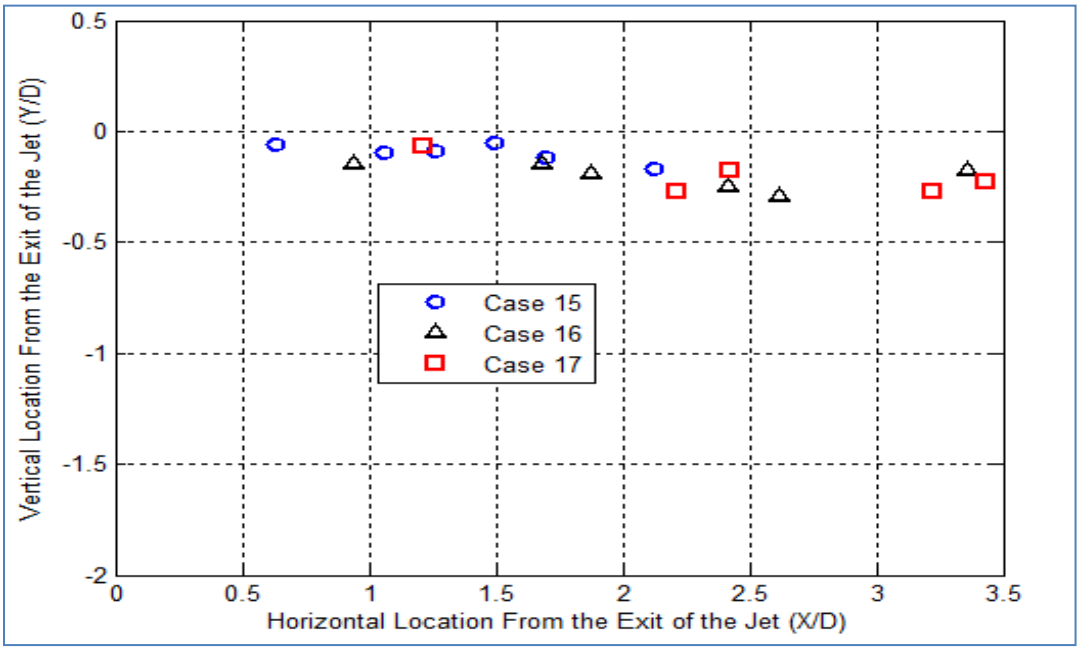

Figure 87. Effects of Reynolds Number on the Trajectory

To validate this, the Reynolds number was investigated in Cases 15, 16, and 17. Figure 87 presents a comparison of the jet trajectory at a constant Reynolds number of 1430 while the

Froude number is respectively 2.75, 4.97, and 7.3. This was accomplished by varying the jet diameter and the jet velocity systematically. The respective trajectories were nearly flat for these cases. This highlights that the buoyancy is dictated by characteristics of the jet such as the jet's velocity and diameter. This in turns validates the dependence of the jet trajectory on the Froude number (which depends on the jet's characteristics). However, as mentioned above, the effect of the co-flow in straightening the overall trajectory of the jet cannot be ignored and has to be incorporated in the formula of the Froude number.

IV.3. Experiment # 3: G-loaded Buoyant Jet in a Co-flow

Various cases were run and processed to investigate the effect of G-loading on the trajectory and mixing behavior of the jet. As shown in Table 4 cases of high (up to 1500) and low G-loading (as low as 0.07) were considered.

Table 4. G-loaded Buoyant Jet Cases

Cases	D (mm)	V_{air} (m/s) (co-flow)	V_{CO2} (m/s)	$V_{ratio} = \frac{V_{CO2}}{V_{air}}$	G_{Jet}	G_{Air}	Re_{jet}	Fr_{jet}
1	6.35	0.457	0.512	1.12	0.07	0.05	404	3.45
2	6.35	0	0.512	∞	0.07	-	404	3.45
3	10.94	2.652	1.989	0.75	1	1.77	2700	10.2
4	10.94	0	1.989	∞	1	-	2700	10.2
5	10.94	2.652	2.811	1.06	2	1.77	3280	14.4
6	10.94	0	2.811	∞	2	-	3280	14.4
7	10.94	2.652	3.447	1.3	3	1.77	4685	17.7
8	10.94	0	3.447	∞	3	-	4685	17.7
9	10.94	2.652	3.978	1.5	4	1.77	5400	20.4
10	10.94	0	3.978	∞	4	-	5400	20.4
11	10.94	13.411	20.120	1.5	100	45	27341	103
12	10.94	0	20.120	∞	100	-	27341	103
13	10.94	29.718	44.577	1.5	500	222	60585	228
14	10.94	0	44.577	∞	500	-	60585	228
15	10.94	42.062	63.093	1.5	1000	445	85751	320
16	10.94	0	63.093	∞	1000	-	85751	320
17	10.94	47	70.5	1.5	1500	650	105014	390
18	10.94	0	70.5	∞	1500	-	105014	390

Earlier analysis on the horizontal buoyant jet indicated that the co-flow contributed in straightening the jet trajectory and increasing the mixing of the jet with air. Plots of the jet's raw intensity counts or percent standard deviation are usually employed to highlight areas of mixing and changes of the jet's concentration. However, for the G-loaded jet's experiment, the laser beams went through windows of quartz through which imaging occurred. This significantly lowered the overall collected intensity of the Rayleigh scattering signal causing a lower difference between the intensity counts in the core of the jet and in the top and bottom shear layer. Changes in the fluctuations of the jet could not then be picked up by the standard deviations and hence standard deviation plots were not generated for this section. Another reason for which the standard deviation plots were not useful in this case was that at high G-loading, the velocity of the jet was so fast to the point the changes due to mixing were not picked up. To illustrate this observation, three points, as shown in Figure 88, were considered on the first position line (X/D = 1.33 D) of Case 11 where some fluctuations were noted by visually inspecting the collected images. Point 1 is located in the top shear layer, Point 2 is in the middle of the jet, and Point 3 is in the bottom shear layer.

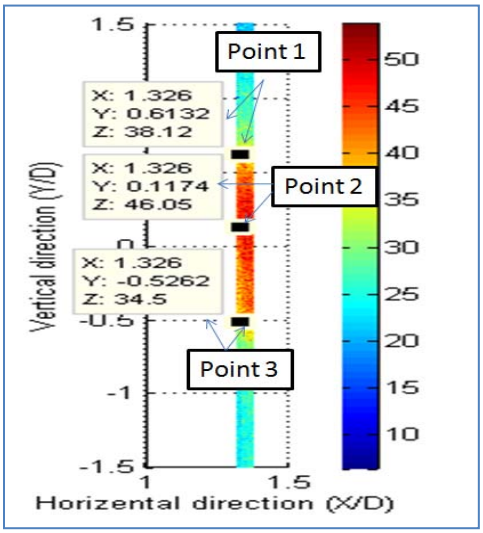

Figure 88. Locations of the three Considered Points of Case 5 (G-loaded Jet)

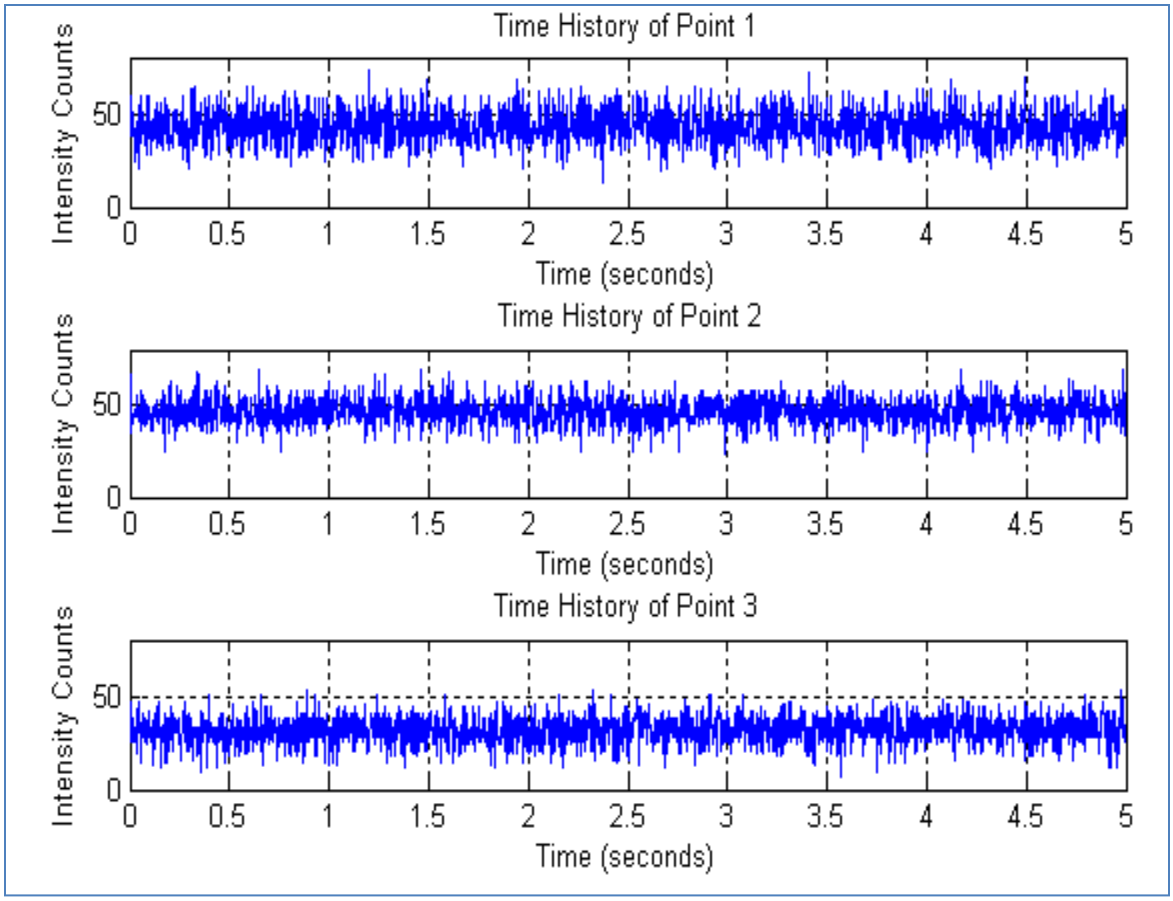

Figure 89. Time Histories of the Three Points of Figure 88

As indicated in Figure 89, the standard deviations of the Rayleigh scattering signal intensity of the three points had similar values around 20 counts. There were no significant changes in the standard deviation going from the top shear layer, to the core of the jet, and to the bottom shear layer. Based on the collected video (and images) for this case, the signal to noise ratio was very low. For cases 1 through 5, the velocity of the jet was comparable to cases run in the horizontal jet experiment where standard deviation plots exhibited relatively higher values. The signal to noise ratio, for the case of the G-loaded jet however, was much lower due to the fact that imaging now occurs through quartz (which was not the case for the case of the horizontal jet experiment). This explains the irrelevance of plotting the standard deviation of which a sample plot is provided in Figure 90.

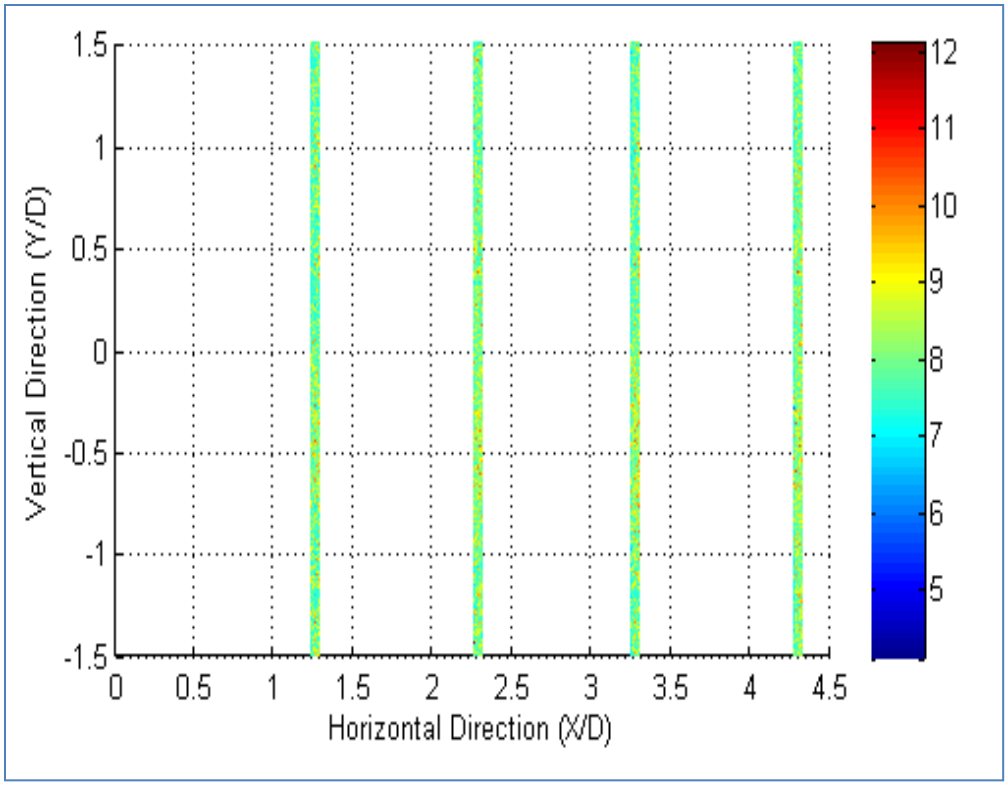

Figure 90. Case 11 Standard Deviation (Intensity Counts) Plot

Initially, when processing the data, the intent was to plot the concentration data of the jet at six different stream-wise locations. However, due to the inconsistency in the laser power and possible (unnoticed) minor drifts of the laser's wavelength over time, the concentration lines which correspond to the third position (after the traverse was moved two diameters) for cases 1 through 10 and 17 were ignored. In addition, the lines corresponding to second position (after the traverse was moved one diameter) for cases 11 through 16 and 18 were also ignored for the same reason.

Part of the analysis in this section involves understanding the effects of the addition of the co-flow to the flow field on the jet's behavior in the presence of G-loading. Figure 91, Figure 92, Figure 93, and Figure 94 illustrate concentration plots of the CO_2 jet when it is subject to respectively a G-load of 0.07, 4,100, and 1000.

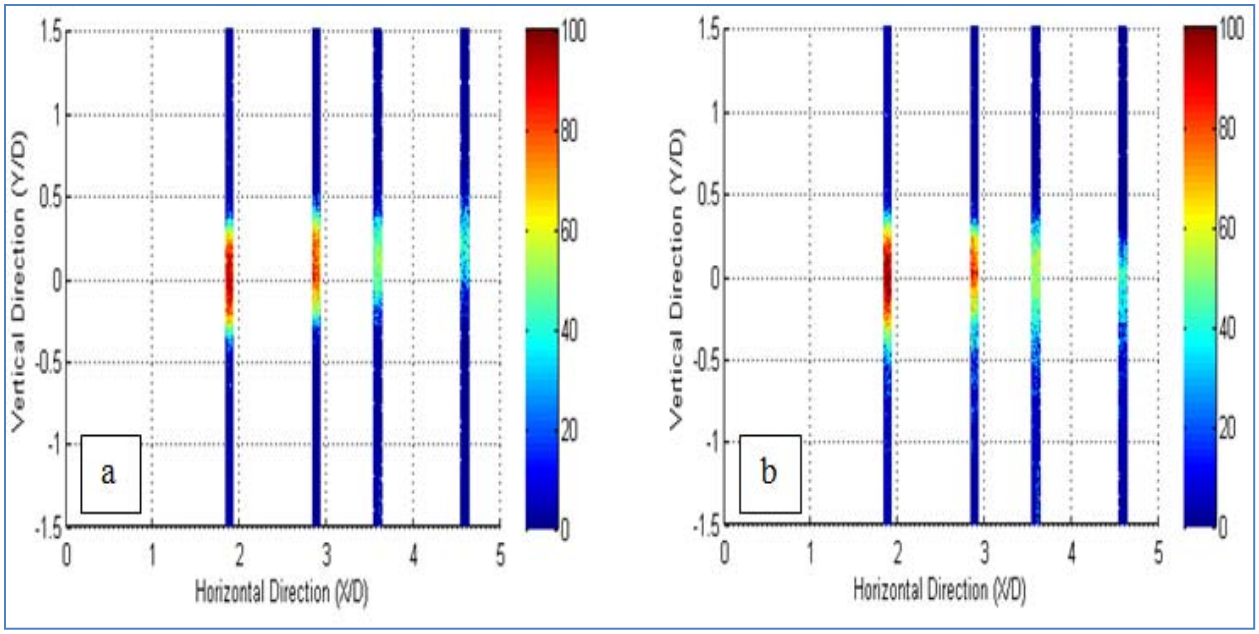

Figure 91. CO_2 Jet Concentration Plots for G_{jet} = 0.07: (a) Case 1 (With Co-flow) and (b) Case 2 (Without Co-flow)

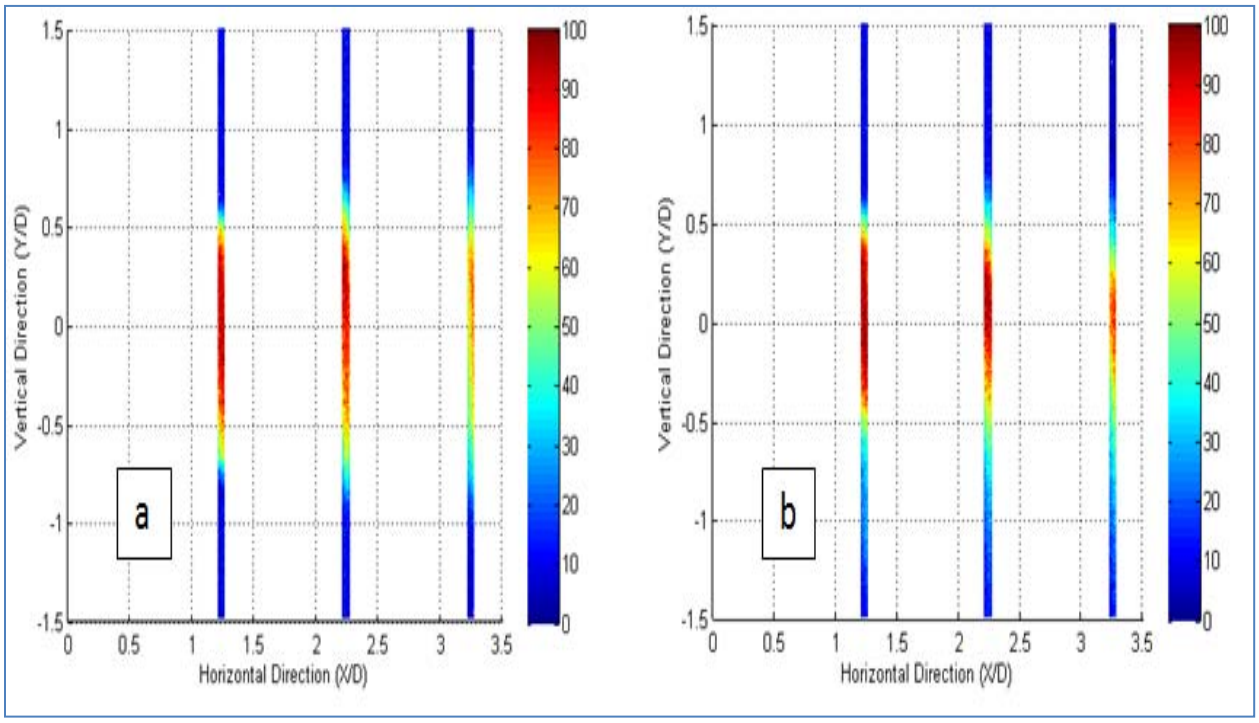

Figure 92. CO_2 Jet Concentration Plots for G_{jet} = 4: (a) Case 9 (With Co-flow) and (b) Case 10 (Without Co-flow)

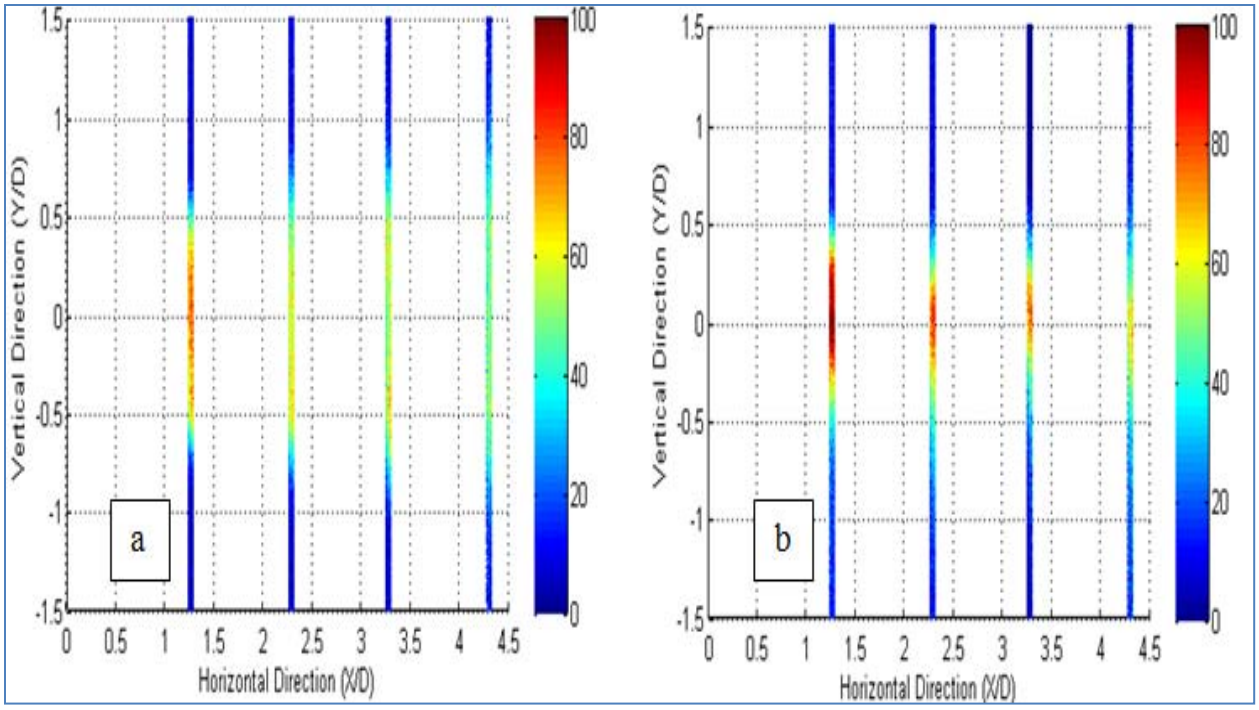

Figure 93. CO_2 Jet Concentration Plots for G_{jet} = 100: (a) Case 11 (With Co-flow) and (b) Case 12 (Without Co-flow)

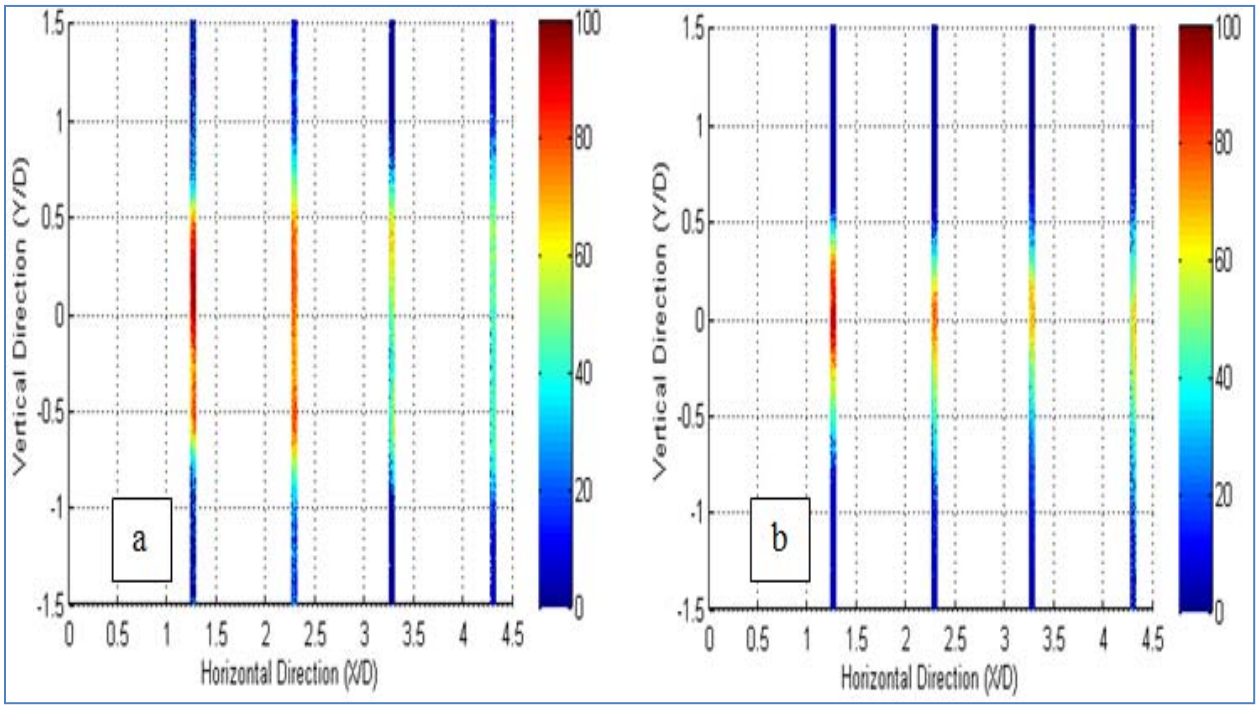

Figure 94. CO_2 Jet Concentration Plots for G_{jet} = 1000: (a) Case 15 (With Co-flow) and (b) Case 16 (Without Co-flow)

With the exception of Case 1 and Case 2 where the G-loading and the jet velocities were small, it was very apparent that the co-flow contributed to increasing the mixing of the jet with air. This could clearly be seen especially when comparing the jet concentration with and without co-flow for the cases considered in figures above. In fact, the plots illustrated more spreading of the jet across the vertical location in the presence of the co-flow which indicated the occurrence of more mixing. It was not apparent however, at low G-loading values that the increase in the G-loads contributed to a significant change in the mixing of the jet. Concentration profiles of cases corresponding to different G-loading were then generated to investigate the effect of G-loading on the jet trajectory and the structure of the jet. At relatively low G-loading (between 0.07 and 4), the G-loading does not seem to drastically influence the direction of the jet nor its core structure. This observation is underlined when looking at the jet concentration profiles at G-loadings of 0.07, 1,2,3 and 4 with and without co-flow as shown in Figure 95, Figure 96, Figure 97, and Figure 98 respectively.

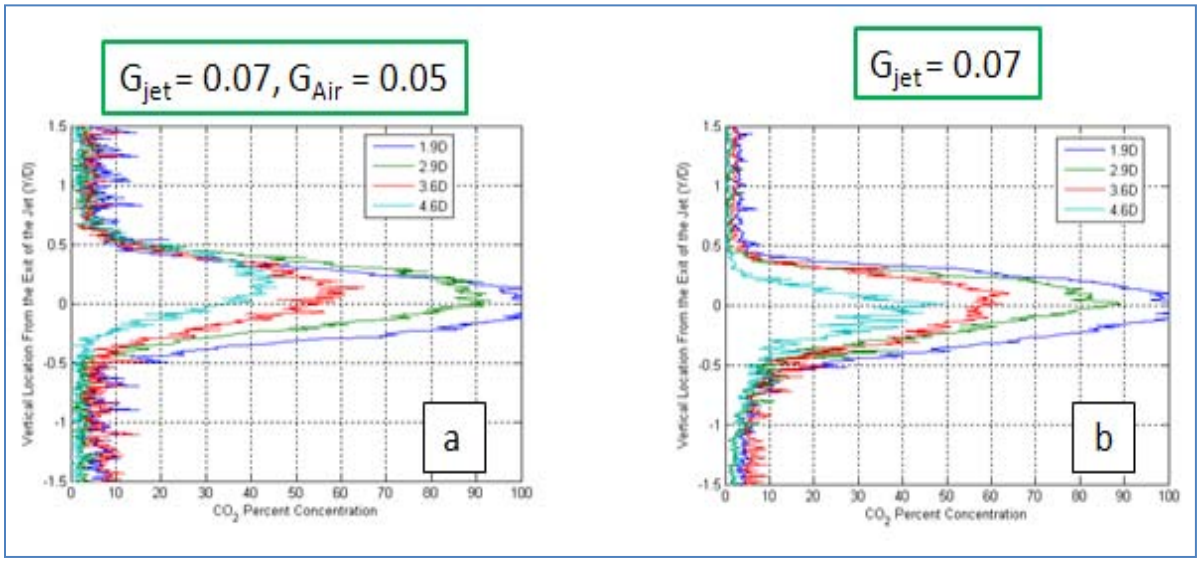

Figure 95. CO_2 Concentration Profile for G_{jet} = 0.07: (a) Case 1 (With Co-flow) and (b) Case 2 (Without Co-flow)

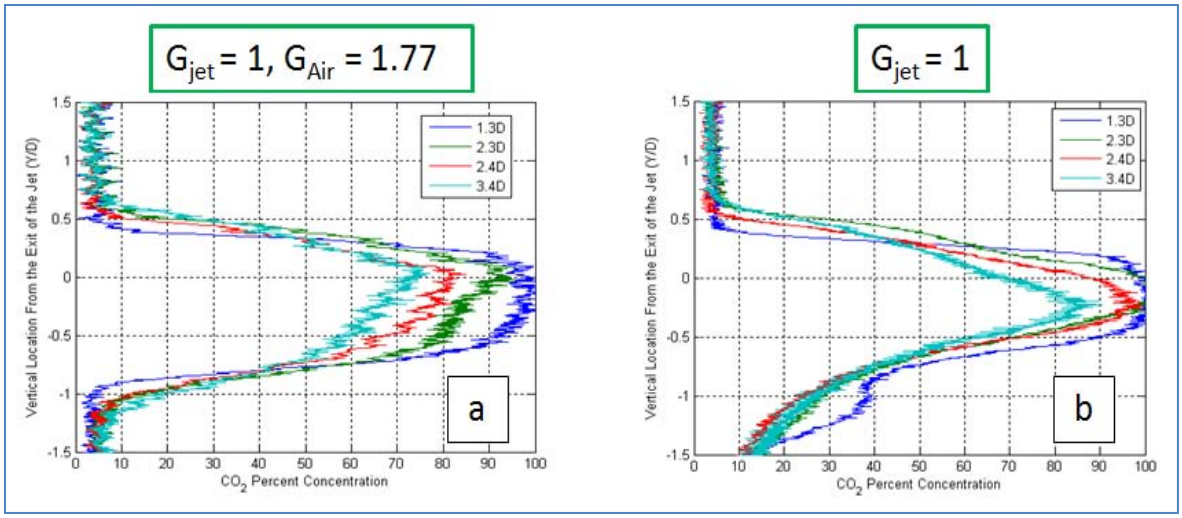

Figure 96. CO_2 Concentration Profile for G_{jet} = 1: (a) Case 3 (With Co-flow) and (b) Case 4 (Without Co-flow)

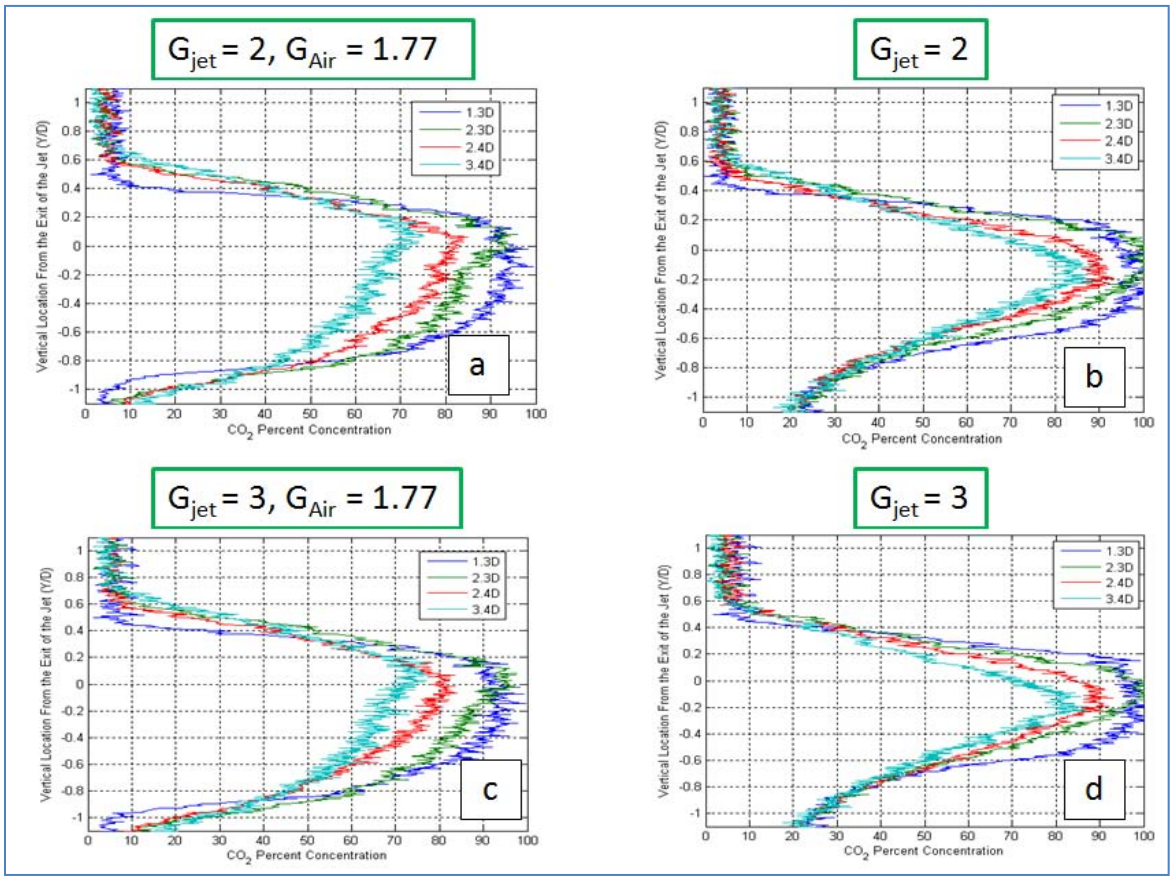

Figure 97. CO_2 Concentration Profile for: (a) Case 5 (With Co-flow),(b) Case 6 (Without Co-flow), (c) Case 7 (With Co-flow), and (d) Case 8 (Without Co-flow)

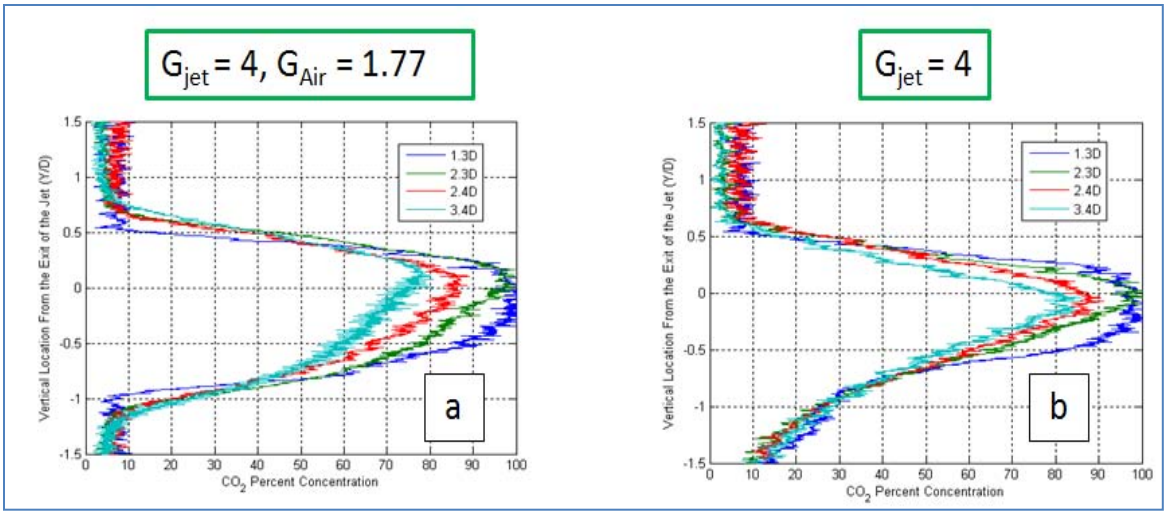

Figure 98. CO_2 Concentration Profile for G_{jet} = 4: (a) Case 9 (With Co-flow) and (b) Case 10 (Without Co-flow)

It could also be noted based on Figure 95, Figure 96, Figure 97, and Figure 98 that the G-loading clearly raises the overall profile of the jet upward in the presence of co-flow. This could be due to the subjection of both the jet and the co-flow to G-loading. Based on Figure 98a, the vertical peak (Y/D) of the concentration profile increased by 0.15 D when the stream-wise location (X/D) increased by 2.1 D. In the absence of co-flow however, jet concentration profile dropped clearly down due to buoyancy. As shown in Figure 98b, this overall drop is about 0.1D in the absence of co-flow.

As shown in Table 4, the first ten cases correspond respectively to G-loadings of 0.07, 1, 2, 3, and 4 (with and without co-flow) with the G-loading of the air kept constant at 1.77 (with the exception of Case 1 and Case 2). For some of these cases, the G-loading of the jet was higher than that of the air and lower for others. Therefore, the ratio of the G-loading of the jet with respect to the G-loading of air was different for these cases. In order to investigate the effects this ratio has on the mixing or trajectory of the jet, Figure 99, was generated. Based on this plot, it appears that the difference (ratio) between the G-loading of the jet and that of air does

not seem to strongly affect the mixing of the jet nor its trajectory at least at low G-loading values.

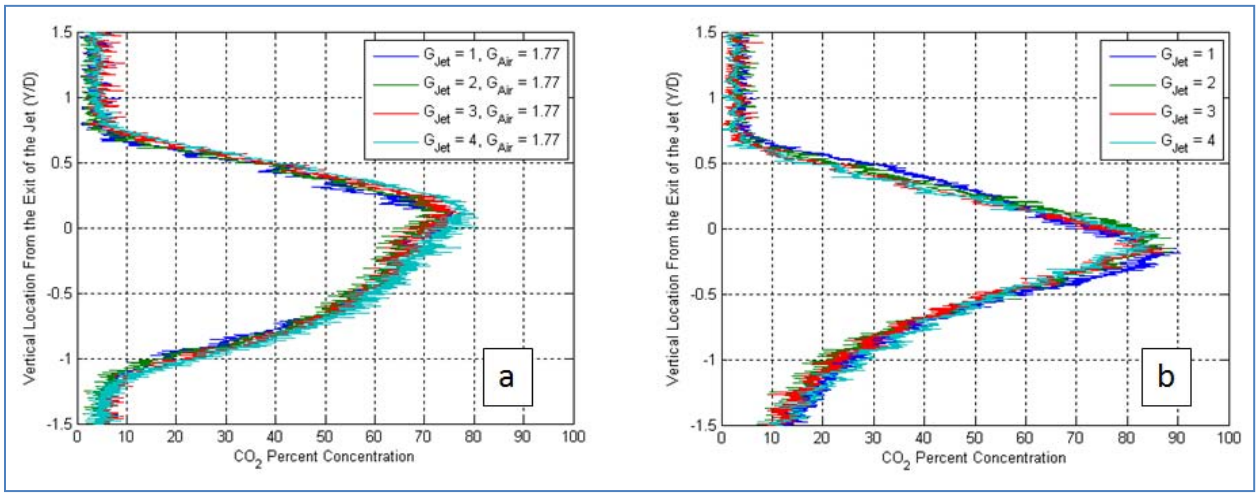

Figure 99. Comparing Concentration Profiles at X/D = 3.4

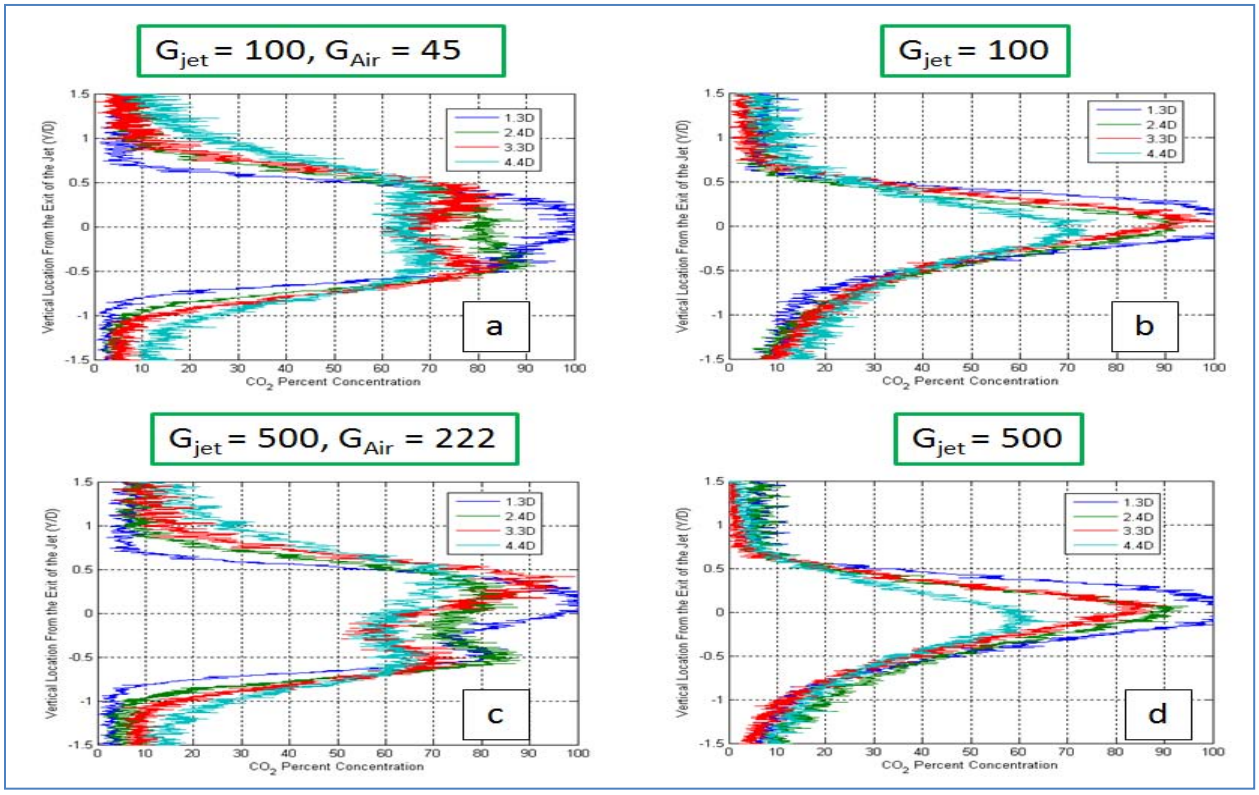

Figure 100. CO_2 Concentration Profile for: (a) Case 11 (With Co-flow),(b) Case 12 (Without Co-flow), (c) Case 13 (With Co-flow), and (d) Case 14 (Without Co-flow)

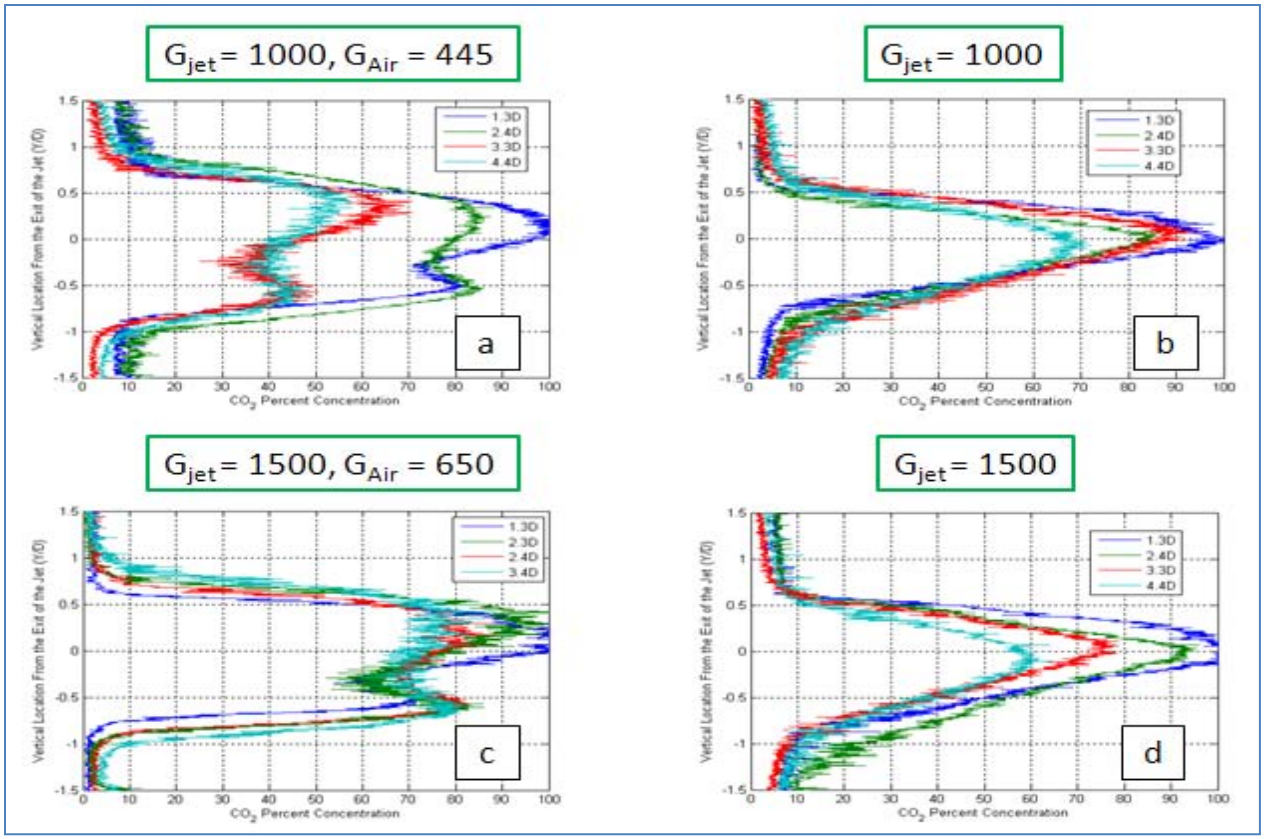

Figure 101. CO_2 Concentration Profile for: (a) Case 15 (With Co-flow), (b) Case 16 (Without Co-flow), (c) Case 17 (With Co-flow), and (d) Case 18 (Without Co-flow)

Concentration profiles at higher G-loading ranging from 100 to 1500 were illustrated in Figure 100 and Figure 101. Based on these plots, the jet maintained an almost straight trajectory in the absence of the co-flow. This was expected since the jet had large momentum (large velocity and Fr as well) at these high G-loading values. The jet maintained, in the absence of the co-flow, relatively similar and narrow concentration profiles that decreased in the overall peak as the stream-wise location increased due to mixing. On the other hand drastic changes occurred to the shapes of the profiles in the presence of co-flow. In addition, at these values of G-loading, the concentration profiles exhibited the development of two peaks. At relatively low G-loading (G_{Jet} = 100), these peaks appeared to initially develop evenly about the center of the jet (Y/D=0). Then, as the G-loads increased, the two peaks became more and more distinct leading to the

development of a double-headed profile with a larger top peak. Overall, the two peaks were much more apparent as the G-loading increases. The development of the two peaks was only noted, however, in the presence of co-flow. This indicates that this change in the jet's core structure is due to the interaction between the jet and the co-flowing air subject to G-loading. A possible explanation of this change in the structure of the jet could be based on Schlichting and Gersten's observations on the flow with a curved pipe [28]. The authors noted that due to the presence of a large centrifugal force, a secondary flow (in the pipe) emerges "outwards in the center and inwards (towards the center of curvature) near the wall" as shown in Figure 102.

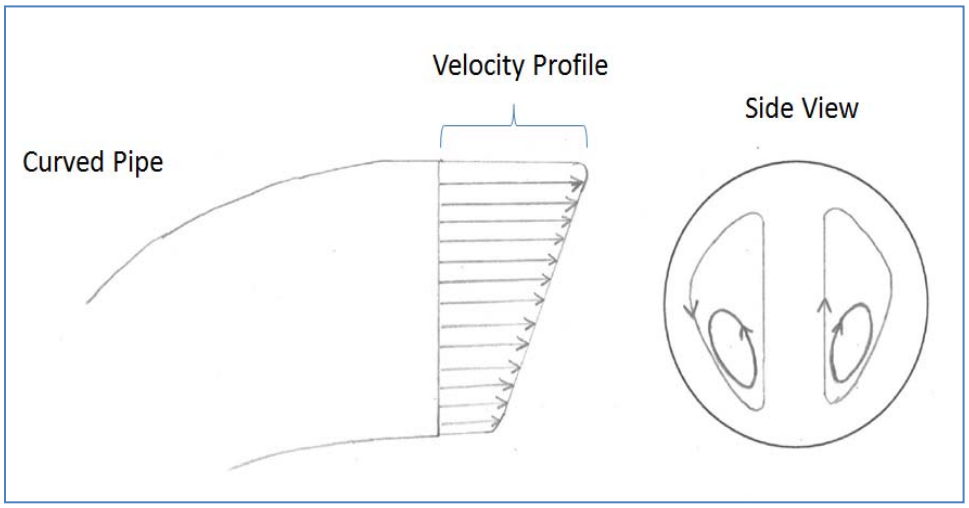

Figure 102. Flow in a Curved Pipe, after Prandtl (as inspired by Schlichting *et al.*'s figure)

The effects of the large centrifugal force are not only associated with the jet in the tube but also with the air which flows in a curved cavity section. The observations noted in Figure 100 and Figure 101 could be the combination of the change in the flow structure undergone by both the jet and the co-flow. With the formation of a large upper peak and small bottom peak within the core of the jet, the jet mixes more with air in the bottom part of the jet and the overall trajectory appears to be slightly moving outwards (away from the center of the curvature). In addition, based on the overall trajectory of the jet for cases with and without co-flow, it appears

that, at high G-loading, the effects of buoyancy (bringing the jet down), are overcome by the high momentum of the jet and G-loading effects.

V. Conclusions

V.1. Findings

The goal of this work was to understand the impact of buoyancy and G-loading on a jet in the presence of a co-flow. Filtered Rayleigh Scattering (FRS) was used to illustrate the jet trajectory and mixing properties of a buoyant jet using both helium and CO_2 gases. Three different experiments were set up, and run for that purpose. The concentration data acquired with FRS was unique in that a continuous wave laser was used in combination with a high speed camera to produce data at 400 Hz (80 Hz when helium was used). This enabled spatio-temporal data collection along a linear expanse at a single stream-wise position. By passing the laser beam through the jet twice, spatio-temporal plots at two different stream-wise positions were also enabled. These time-resolved measurements of concentration along a line were used to investigate the interactions of the jet with a co-flow of air for both the horizontal and G-loaded jet configurations. The concentration of the jet was measured at several locations up to 4.4 D away from the exit of the jet.

The first experiment was the Iodine filter characterization which led to the identification of the transmission well associated with the molecular filter used in the second and third experiments. The transmission well (or alternatively called the absorption well) defined the range of operation of wavelength for which there was maximum blocking of background noise and hence allowed for the collections of relevant Rayleigh scattering signal.

The second experiment involved the acquisition of concentration data of a horizontal jet in a co-flow of air using both helium and CO_2 gases. Cases with a co-flow of air and without the co-flow were run to examine the effects on the trajectory curve and the mixing of the jet. Processed data of Rayleigh scattering signal for cases with or without co-flow indicated that the

jet in general curved downwards as it traveled downstream of the jet for the case of the CO_2 jet due to negative buoyancy and upwards for the case of the helium jet due to positive buoyancy. The generation of standard deviation plots of the Rayleigh scattering signal and the time histories of the signal's intensity at different locations along the imaging lines highlighted the time resolved aspect of this analysis. These clues were incorporated to identify areas of significant mixing between the jet and the co-flowing air. In general, it was deduced from the horizontal jet experiment that the addition of the co-flow to the flow field contributed to both the straightening of the jet trajectory and the increase of its mixing with air.

In addition, the shape of the trajectory was investigated through the variation of the jet velocity, the jet to co-flow velocity ratio, the relative velocity, the Froude number, and the Reynolds number. The Froude number definition used for comparison was based on the jet velocity only and did not take into account the co-flow velocity. The trajectory plots were generated by tracking the maximum value of CO_2 concentration along a strip of the Rayleigh scattering line at multiple stream-wise locations. The trajectory analysis demonstrated that in the presence of the co-flow, the jet velocity had an initial impact on the resultant jet location and spread causing a more horizontal jet to convect downstream. The velocity of the jet then had the strongest effect of all other considered parameters in shaping the trajectory of the jet. Cases with co-flow where the Froude number was kept constant resulted in consistent trajectories and thus impacts of buoyancy. However, at that same Froude number, the trajectory was noticeably different when there was no co-flow. This confirmed that the traditional definition of Froude number based on the jet velocity was the correct parameter to normalize the data; however a correction is needed to account for the presence of a co-flow for future analysis and studies.

The third experiment was set up to investigate the effects of G-loading (centrifugal force) on the jet trajectory and mixing of the jet with air. It turned out that the centrifugal force due to the flow of the jet in a curvature changed drastically the structure of the core of the jet in the presence of co-flow. The classical bell shaped concentration profile turned to a double headed profile in the presence of high G-loading causing the jet to slightly move outwards (away from the center of the curvature) on one hand and an increase in the mixing with air on the other hand. At high G-loading where the velocity of the jet was significantly high, the effects of buoyancy which pulled the jet down were overcome by the effects of G-loading which pushed it outwards.

V.2. Recommendations & Future Work

The idea behind imaging along two laser lines as opposed to using a sheet of laser stems from the need to get the most out of the 12 W laser systems available in the COAL lab. Using a sheet of laser would result in the decrease of the incident laser power and hence a lower signal to noise ratio. However, a disadvantage of this method is that concentration data is only obtained along the laser line which has a relatively small width. Essentially data, between the lines is unknown. In order to bypass this problem, it is recommended for future studies to perform multi-passes of the laser using top and bottom sets of mirrors or prisms. The idea is to collect the Rayleigh scattering signal along multiple lines with relatively small spacing between them. That way, data can be collected simultaneously at different stream-wise locations without the need for a traverse unit or similar systems.

In addition, when processing data for this study, the signal to noise ratio was in some cases low to the point that it was hard sometimes to distinguish between the Rayleigh scattering signal associated with air and that due to CO_2. Although this was not a major issue, it is recommended for future buoyant jet in co-flow studies to use CO_2 as a jet and helium as a co-flow instead of

air. From a fundamental stand point this would be very advantageous due to the presence of a significantly large density gradient between CO_2 and helium. Furthermore, the distinction between the Rayleigh scattering signals associated with both gases would be relatively easy since the Rayleigh scattering cross section of the helium is approximately about 0.6 % of that of CO_2.

As far as developing an equation for the Froude number that would take into account the addition of the co-flow into the flow field, it is recommended to start with the classical definition of the Froude number and modify it. The velocity of the co-flow has to be included in the new formula which could have the velocity of the jet as an exponent to a factor to be determined empirically via the analysis of multiple cases. The reason for this choice is that, in the case when the velocity of the co-flow is zero (no co-flow), the new model collapses back to the classical definition of the Froude number since any factor raised to zero would be one. This model could serve as an initial guess for the development of the new formula but is not necessarily the only one.

Bibliography

1. Subbarao, E., "The Effects of Reynolds Number and Richardson Number on the Structure of a Vertical Co-flowing Buoyant jet," AIAA Paper 89-1800, AIAA 20th Fluid Dynamics, Plasma Dynamics and Lasers Conference, Buffalo, New York June 12-14, 1989.

2. Xiao, J., Travis, J.R., and Breitung, W., "Boussinesq Integral Model for Horizontal Turbulent Buoyant Round Jets," *Since and Technology of Nuclear Installations*, Vol. 2009, Article ID 862934.

3. Rausch, A., Fischer, A., Holger, K., Gaertlein, A., Nirsch, S., Knobloch, K., Bake, and F., Rohle, I., "Measurements of Density in the Outlet Nozzle of a Combustion Chamber by Rayleigh-Scattering Searching Entropy Waves, " Proceedings of ASME Turbo Expo 2010: Power for Land, Sea, and Air, GT2010-22492, Glasgow, UK, June 14-18, 2010.

4. Eckbreth, A.C, "Laser Diagnostics for Combustion Temperature and Species", Second Edition, pp 3, United Technologies Research Center, Connecticut, 1996.

5. Adrian, R.J, "Twenty Years of Particle Image Velocimetry", *Experiments in Fluids*, Vol. 32, Number 2, pp 159-169, 2005.

6. Miles, R.B., Lempert, W.R., and Forkey, J.N., "Laser Rayleigh Scattering," *Meas. Sci. Tech.*, Vol. 12, pp. 33-51, 2001.

7. Miles, R.B., Lempert, W.R., and Forkey, J.N., "Accuracy Limits for Planar Measurements of Flow Filed Velocity, Temperature and Pressure using Filtered Rayleigh Scattering", *Experiments in Fluids*, Vol. 24, pp 151-162, 1998.

8. Miles, R.B, Yalin, A.P, Tang, Z, Zaidi, S. H, and Forkey, J.N., "Flow Field Imaging through Sharp-edged Atomic and Molecular 'Notch' Filters ", *Measurement Science and Technology*, Vol. 12, pp 442-451, 2001.

9. Polanka, M.D, Reeder, M.F, and Hartsfield, K.C, "Fundamental Issues in Integrating of UCC Combustor with a Turbine Vane" AFIT Research Proposal to AFRL/AFIT MOA Small Grant Program, March 2010.

10. Anderson, W.S, Radtke, J.T, King, P.I, Thornburg, H, Zelina, Z., and Sekar, B., "Effects of Main Swirl Direction on High-g Combustion", AIAA Paper 2008-4954, 44th AIAA/ASME/SAE/ASEE Joint Propulsion Conference & Exhibit, Hartford, Connecticut, 21-23 July 2008.

11. Mielke, A., Seasholtz, R., Elam, K., and Panda, J., "Time-average measurement of velocity, density, temperature, and turbulence velocity fluctuations using Rayleigh and Mie scattering" 2005.

12. Miles, R.B., and Lempert, W.R., "Flow Diagnostics in Unseeded Air", AIAA Paper 90-0624, 28th Aerospace Sciences Meeting, Nevada, 8-11 January 1990.

13. Sneep,M., and Ubachs, W., "Direct Measurement of the Rayleigh-Scattering Cross Section in Various Gases", *Journal of Quantitative Spectroscopy & Relative Transfer*, Vol. 92, pp 293-310, 2005.

14. Meents, S., "Filtered Rayleigh Scattering Measurement in a Buoyant Flow Field," March 2008.

15. Jenkins,T.P., and Desabrais, K.J., "Three Components Velocity Field Measurements Near a Parachute During a Drop Test," AIAA Paper 2010-1030, 48th AIAA Aerospace Sciences Meeting, Orlando, Florida, January 2010.

16. Cheung, B.H., and Hanson, R.K., "CW laser-induced fluorescence of toluene for time resolved imaging of gaseous flows," Applied Physics B Lasers and Optics, Vol. 98, pp. 581-591.

17. Gebhart, B., Jaluria, Y., Mahajan, R.L, and Sammakia, B., "Buoyancy–Induced Flows and Transport", pp 670, 1988.

18. Reeder,M.F., Huffman, R.E., Branam, R.D., Lebay, K.D., and Meents, S.M., "Mixing of Gas phase Horizontal Laminar Jets with positive and negative buoyancy measured with Filtered Raleigh Scattering," To appear in *EXP.Fluids*, published online , 19 November 2010.

19. Arakeri, J.H, Das, D., and Srinivasan, J., "Bifurcation in a Buoyant Horizontal Laminar Jet", *Journal of Fluid Mechanics*, Vol. 412, pp 61-73, United Kingdom, 2000.

20. Kumar, R., and Yuan, T.D, "Recirculating Mixed Convection Flows in Rectangular Cavities", AIAA Paper 88-0662, AIAA 26th Aerospace Sciences Meeting, Nevada, 11-14 January 1988.

21. Sherif, S.A, Pletcher, R.H, "Jet Wake Thermal Characteristics of Heated Turbulent Jets in Cross Flow", AIAA Paper A88-48776 20-34, 1988.

22. Armstrong, J., "Effect of Equivalence Ratio and G-loading on in SITU Measurement of Chemiluminescence in an Ultra Compact Combustor," March 2004.

23. Lebay, K.D, Drenth, A.C, Thomas, L.M, Polanka, M.D, Branam, R.D, and Schmidt, J.B, "Characterizing The Effects of G-loading in an Ultra Compact Combustor via Sectional Models", GT2010-22723, Proceeding of the Turbo Expo 2010, 14-18 June 2010.

24. Dahm, W.J.A, Lapsa, A.P, "Hypeacceleration Effects on Turbulent Combustion in Premixed Step-Stabilized Flames", *Proceedings of the Combustion Institute*, Vol. 32, pp 1731-1738, 2009.

25. Seasholtz ,R.G., Buggele, A.E., and Reeder , M.F., “Flow measurements based on Rayleigh scattering and Fabry-Perot Interferometer,” *Optics and Lasers in Engineering*, Vol. 27, pp. 543-570, 1997.

26. Su,L.K, Helmer, D.B, and Brownell, C.J., “Quantitative Planar Imaging of Turbulent Buoyant Jet Mixing ”, *Journal of Fluid Mechanics*, Vol. 643, pp 59-95, 2010.

27. Baranyi ,L., Szabó, S., Bolló ,B., and Bordás, R., “Analysis of low Reynolds number flow around a heated circular cylinder,” *Journal of Mechanical Science and Technology*, April 2009.

28. Schlichting, H., Gersten, K., “Boundary Layer Theory”, New York, McGraw-Hill, pp 588, 1955.

Vita

First Lieutenant Firas Benhassen joined the ranks of the armed forces at the age of 19. He graduated from the Tunisian preparatory school for the military academies (Ecole Preparatoire Aux Academies Militaires) in 2004. He then attended the United States Air force Academy (USAFA) and graduated in 2008 with a Bachelor of Science degree in Aeronautical Engineering. After graduation, he was stationed in Tunis at the Tunisian Air Force Academy where he served as an Assistant Air Officer Commander (AAOC) for the freshman class. Lieutenant Benhassen is the first Tunisian officer to attend the Air Force Institute of Technology for a Master's in Aeronautical Engineering. Upon completion of his assignment at AFIT, Lt Benhassen will go back to Tunisia where he will continue to serve his country as an aircraft maintenance officer.

REPORT DOCUMENTATION PAGE		Form Approved OMB No. 0704–0188

1. REPORT DATE (DD–MM–YYYY)	2. REPORT TYPE	3. DATES COVERED *(From — To)*
24 03 2011	Master's Thesis	February 2010 — March 2011

4. TITLE AND SUBTITLE	5a. CONTRACT NUMBER
Time Resolved Filtered Rayleigh Scattering Measurement of a Centrifugally Loaded Buoyant Jet	5b. GRANT NUMBER
	5c. PROGRAM ELEMENT NUMBER

6. AUTHOR(S)	5d. PROJECT NUMBER
Firas Benhassen, 1st Lt, TUNAF	5e. TASK NUMBER
	5f. WORK UNIT NUMBER

7. PERFORMING ORGANIZATION NAME(S) AND ADDRESS(ES)	8. PERFORMING ORGANIZATION REPORT NUMBER
Air Force Institute of Technology Graduate School of Engineering and Management (AFIT/ENY) 2950 Hobson Way WPAFB OH 45433-7765	AFIT/GAE/ENY/11-M01

9. SPONSORING / MONITORING AGENCY NAME(S) AND ADDRESS(ES)	10. SPONSOR/MONITOR'S ACRONYM(S)
Directorate Aerospace, Chemical, and Material Sciences Air Force Office of Scientific Research Tele: (703) 696-8478 DSN: 426-8478 Fax: (703) 696-8451 Dr. Julian Tishkoff 4015 Wilson Boulevard, Room 713 Arlington, VA 22203-1954 E-mail: julian.tishkoff@afosr.af.mil	AFOSR
	11. SPONSOR/MONITOR'S REPORT NUMBER(S)

12. DISTRIBUTION / AVAILABILITY STATEMENT
APPROVED FOR PUBLIC RELEASE; DISTRIBUTION UNLIMITED

13. SUPPLEMENTARY NOTES
This material is declared a work of the U.S. Government and is not subject to copyright protection in the United States.

14. ABSTRACT

The combustion process within the Ultra-Compact Combustor (UCC) occurs in the circumferential direction. The presence of variable flow density within the circumferential cavity introduces significant buoyancy issues. On the other hand, G-loading caused by the presence of centrifugal forces, ensures the circulation of the flow in the circumferential cavity and enhances the completion of the combustion process before allowing the exit of the hot gases to the main flow. The coupling between buoyancy and high G-loading is what predominately influences the behavior of the flow within the UCC. In order to better understand the combustion process within the UCC, three different experiments were run. The overall objective of these experiments is to investigate the effects of both buoyancy and G-loading on the trajectory and the mixing of a jet in a co-flow. The first experiment involved setting up the Filtered Rayleigh scattering (FRS) technique to be used in this research. Then, using horizontal and curved sections, two types of experiments were run to characterize and measure both G-loading and buoyancy effects on the overall behavior of a jet in a co-flow of air. Measurements were made using an FRS set up which involved a continuous wave laser and a high speed camera showing adequate signal to noise ratio at 400 Hz. Collected time resolved images allowed for the investigation of the effects of G-loading and buoyancy on the mixing properties and trajectory of the jet.

15. SUBJECT TERMS
Filtered Rayleigh scattering, Continuous Wave Laser, Horizontal Buoyant Jet, G-loaded Buoyant Jet

16. SECURITY CLASSIFICATION OF:			17. LIMITATION OF ABSTRACT	18. NUMBER OF PAGES	19a. NAME OF RESPONSIBLE PERSON
a. REPORT	b. ABSTRACT	c. THIS PAGE	UU	133	Dr. Marc Polanka
U	U	U			19b. TELEPHONE NUMBER (Include Area Code) Tele: (937)255-3636, ext 4714 Email: marc.polanka@afit.edu

Standard Form 298 (Rev. 8–98)
Prescribed by ANSI Std. Z39.18